Hydrogen and Nitrogen Plasma Treated Materials with Disordered Surface Layer used for Energy Storage and Conversion Devices

DISSERTATION

zur Erlangung des akademischen Grades

Doktoringenieur (Dr.-Ing.)

vorgelegt der

Fakultät für Elektrotechnik und Informationstechnik

der Technischen Universität Ilmenau

von

M. Sc. Hongmei Wang

geb. am 27.07.1990 in Gansu, V.R. China

2019

1. Gutachter: Univ.-Prof. Dr. rer. nat. habil. Dr. h. c. Peter Schaaf
(Technische Universität Ilmenau)
2. Gutachter: Prof. Dr. rer. nat. habil. Dr. h.c. Andreas Bund
(Technische Universität Ilmenau)
3. Gutachter: Prof. Dr.-Ing. Ge Chen
(Beijing University of Technology)

Tag der Einreichung: 02.09.2019
Tag der wissenschaftlichen Aussprache: 20.12.2019

urn:nbn:de:gbv:ilm1-2019000535

Abstract

Plasma treatment is considered as an easy and effective method for the modification of materials' surface of electrodes for electrochemical energy storage and conversion devices to improve the performances. As a result, a disordered surface layer and atom vacancies could be formed after the high-power plasma treatment, which play significant roles on enhancing the performances of energy storage and conversion materials. In this work, hydrogen and nitrogen plasma are used to modify anode materials for lithium and sodium ion batteries (LIBs and SIBs), and electrochemical catalysts for the nitrogen reduction reaction (NRR), and the electrochemical application performances of these materials are tested.

Firstly, WS_2 nanoparticles are modified through hydrogen plasma treatment at 300 °C for 2 hours, and the hydrogenated WS_2 (H-WS_2) nanoparticles demonstrate a clearly enhanced electrochemical performance as anode material for both LIBs and SIBs. The TEM investigation shows a disordered surface layer with thickness around 2.5 nm after the treatment, and this is also confirmed by the results of the Raman spectroscopy. The shift in the XPS peaks indicates the structure surface disorders are incorporated in the crystalline structure. The H-WS_2 based LIBs and SIBs possess significantly higher specific capacity at different current densities. In addition, the electrochemical impedance spectroscopy (EIS) reveals a drastic decrease of the charge-transfer resistance for both LIB and SIB, which implies the plasma hydrogenated electrode is more favorable for the electron transportation during the electrochemical process. The improved rate performance of H-WS_2 in both applications of LIBs and SIBs can be attributed to the largely reduced charge transfer resistivity at the disordered surface layer.

Secondly, nitrogen doped TiO_2 (N-TiO_2) nanoparticles are prepared via nitrogen plasma treatment and investigated as anode material of SIBs. The N-TiO_2 nanoparticles demonstrate a much better rate performance, yielding discharge capacities of about 621 $mAh \cdot g^{-1}$ at 0.1 C and 75 $mAh \cdot g^{-1}$ at 5 C, as well as a clearly enhanced capacity retention (more than 98 % after more than 400 cycles) than the pristine TiO_2. Different from the other nitrogen doped TiO_2 reported in the literatures, a disordered surface layer with thickness of around 2.5 nm is formed in the N-TiO_2 nanoparticles after the N_2 plasma treatment. Both the doped nitrogen and the disordered surface layer play

significant roles on enhancing the sodium storage performance.

Thirdly, we chose the TiO_2-Au (P-TiO_2-Au, gold nanoclusters supported by P25 TiO_2 nanoparticles, Au loading: ~ 2 wt %) as the electrochemical catalysts for the NRR. The material was modified with H_2 plasma and then formed a blue-black H-TiO_2-Au catalyst, it shown enhanced performance for the nitrogen reduction reaction (NRR) process comparing with the pristine sample. From the TEM investigations we could find some disordered positions on the surface, and also the Raman intensities of H-TiO_2-Au is much lower than the pristine material which could be attributed to the disordered surface and the oxygen vacancies formation. What's more, a small peak shift for the XPS could be found after the hydrogen plasma treatment. When the sample was used for the electrochemical NRR, the yield of NH_3 of blue-black H-TiO_2-Au is around 9.5 times higher than the pristine sample, while the highest faradaic efficiency of 2.7 % is also obtain at the potential of -0.1 V. The density functional theory (DFT) calculation results confirm that H-TiO_2-Au with oxygen vacancies and disordered surface layer is much preferred for the NRR process. It further proves that the reduction process of H_2 plasma treatment makes an important role on the improving of catalysts' performances. It could be the first time that used the plasma technique to modify catalyst for electrochemical NRR processes.

Zusammenfassung

Die Plasmabehandlung gilt als eine einfache und effektive Methode zur Modifikation der Materialoberfläche von Elektroden für elektrochemische Energiespeicher- und Umwandlungsvorrichtungen, um die Leistungen zu verbessern. Infolgedessen konnten nach der Hochleistungsplasmabehandlung ungeordnete Oberflächenschichten und Atomleerstellen entstehen, die eine wichtige Rolle bei der Leistungssteigerung von Energiespeicher- und Umwandlungsmaterialien spielen. In dieser Arbeit werden Wasserstoff- und Stickstoffplasma verwendet, um Lithium- und Natriumionenbatterien (LIBs und SIBs) Anodenmaterialien und elektrochemische Katalysatoren für die Stickstoffreduktionsreaktion (NRR) zu modifizieren, und die elektrochemischen Anwendungsleistungen dieser Materialien zu untersuchen.

Erstens, werden WS_2-Nanopartikel durch Wasserstoff-Plasma-Behandlung bei 300 °C für 2 Stunden modifiziert, und die hydrierten WS_2 (H-WS_2)-Nanopartikel zeigen eine deutlich verbesserte elektrochemische Leistung als Anodenmaterial für Lithium-Ionen-Batterien (LIBs) und Natrium-Ionen-Batterien (SIBs). Die TEM-Untersuchung zeigt eine ungeordnete Oberflächenschicht mit einer Dicke von etwa 2,5 nm nach der Behandlung, was auch durch die Ergebnisse der Raman Spektroskopie bestätigt wird. Die Verschiebung der XPS-Peaks deutet an, dass die Oberflächenstörungen der Struktur in die kristalline Struktur integriert sind. Die H-WS_2-basierten LIBs und SIBs weisen eine deutlich höhere spezifische Kapazität bei unterschiedlichen Stromdichten auf. Darüber hinaus zeigt die Untersuchung der elektrochemische Impedanzspektroskopie (EIS) eine drastische Verringerung des Ladungsübertragungswiderstands sowohl für LIB als auch für SIB. Das bedeutet, dass die plasmahydrierte Elektrode für den Elektronentransport während des elektrochemischen Prozesses vorteilhafter ist. Die verbesserte Leistung von H-WS_2 in beiden Anwendungen von Li und Na Ionenbatterien ist auf den reduzierten Ladungsübertragungswiderstand an der ungeordneten Oberflächenschicht und die verbesserte elektronische Leitfähigkeit durch die Störungsoberfläche in der kristallinen Struktur zurückzuführen.

Zweitens, werden stickstoffdotierte TiO_2 (N-TiO_2)-Nanopartikel durch Stickstoffplasma-Behandlung hergestellt und als Anodenmaterial von Natriumionenbatterien (SIBs) untersucht. Die

N-TiO_2-Nanopartikel weisen eine wesentlich bessere Ratenleistung auf und liefern Entladekapazitäten von etwa 621 mAh-g^{-1} bei 0,1 C und 75 mAh-g^{-1} bei 5 C sowie eine deutlich verbesserte Kapazitätserhaltung (mehr als 98% nach mehr als 400 Zyklen) als das unbehandelte TiO_2. Im Gegensatz zu den anderen stickstoffdotierten TiO_2, von denen in der Literatur berichtet werden, bildet sich in den N-TiO_2-Nanopartikeln nach der N_2-Plasmabehandlung eine ungeordnete Oberflächenschicht mit einer Dicke von etwa 2,5 nm. Sowohl der dotierte Stickstoff als auch die ungeordnete Oberflächenschicht spielen eine wichtige Rolle bei der Verbesserung der Natriumspeicherleistung.

Drittens, haben wir das TiO_2-Au (P-TiO_2-Au, Goldnanocluster, unterstützt durch P25 TiO_2-Nanopartikel, Au-Belastung: ~ 2 wt%) als elektrochemische Katalysatoren für die Stickstoffreduktionsreaktion benutzt. Das Material wurde mit H_2-Plasma modifiziert und bildete dann einen blau-schwarzen H-TiO_2-Au-Katalysator, der eine verbesserte Leistung für den Prozess der Stickstoffreduktionsreaktion (NRR) im Vergleich zur unbehandelten Probe zeigte. Aus den TEM-Untersuchungen konnten wir einige ungeordnete Positionen an der Oberfläche finden, und auch die Raman-Intensitäten von H-TiO_2-Au sind viel niedriger als das unbehandelte Material, das auf die ungeordnete Oberfläche und die Bildung von Sauerstoffleerstellen zurückzuführen ist. Darüber hinaus konnte nach der Wasserstoff-Plasma-Behandlung ein kleiner Peak-Shift im XPS -Spektrum festgestellt werden. Wenn die Probe für die elektrochemische NRR verwendet wurde, ist die Ausbeute an NH_3 von blau-schwarzem H-TiO_2-Au etwa 9,5 mal höher als die unbehandelte Probe, während die höchste faradaysche Effizienz von 2,7 % auch bei dem Potential von -0,1V erreicht wird. Die Ergebnisse der DFT-Berechnung bestätigen, dass H-TiO_2-Au bei Sauerstoffleerstellen und ungeordneter Oberflächenschicht für den NRR-Prozess sehr bevorzugt wird. Es zeigt außerdem, dass der Reduktionsprozess der H_2-Plasma-Behandlung eine wichtige Rolle bei der Verbesserung der Leistung von Katalysatoren spielt. Es könnte das erste Mal sein, dass die Plasmatechnik zur Modifikation des Katalysators für elektrochemische NRR-Prozesse eingesetzt wurde.

Acknowledgements

First and foremost, I would like to thank my supervisor Prof. Dr. Peter Schaaf. It is a great honor to be his PhD student and I am so grateful for that giving me this opportunity to pursue my PhD in his group and he has taught me a lot and his guidance helped me all the time of research and writing this thesis. And then I want to give my gratitude to Dr. Dong Wang. I appreciate all his contribution of time, patience, immense knowledge, encouragement, support and guidance to make my PhD study enjoyable and productive. Besides, I want to express my high gratitude to Prof. Dr. Ge Chen from Beijing University of Technology for his great contribution in this work.

This work was also partly supported by the Deutsche Forschungsgemeinschaft DFG (grant DFG Scha 632/24) within the priority programme "Tailored Disorder" (SPP 1839).

I also thank the state of Thuringia and the TU Ilmenau for the graduate fellowship.

I would like to thank Prof. Peter Schaaf, Prof. Andreas Bund and Prof. Ge Chen being the reviewers of my dissertation. Thank you for the doctoral committee members, Prof. Dr.-Ing. Jens Müller, Dr.-Ing. Dong Wang and Dr. rer. nat. Adriana Ispas from TU Ilmenau for their patience and support.

And I want to thank my colleagues Dr. Thomas Kups, Mr. Marcus Hopfeld, Dr. Henry Romanus, Mr. Dominik Flock for their help with sample characterization. I also acknowledge Dr. Anni Wang, Dr. Manuel Oliva Ramires, Mr. Dmitry Zyabkin, Mrs. Antje Schencke, Miss. Yesenia Haydee Sauni Camposano, Mr. Feitao Li, Mr. Pengfei Cheng, Mr. Honglei Wang, Mr. Sebastian Matthes and Dr. Andreas Diemar, Mrs. Elvira Remdt, Dr. Andreas Herz and Mrs. Diana Herz for their assistance with my experiments and PhD life of the group of Materials for Electrical Engineering and Electronics.

In addition, I am grateful to Dr. Arne Albrecht, Mrs. Birgitt Hartmann, Mrs. Manuela Breiter, Mr. Joachim Döll, Mr. David Venier and Mr. Stefan Hanitsch and Mr. Frank Bucke from ZMN for their help with sample preparation.

What's more, I want to thank Prof. Andreas Bund and his colleagues Dr. Michael Stich, Mr. Mario Kurniawan, Mr. Mathias Fritz and Mrs. Karin Keller of their help and support of my experiments.

Also, many thanks to Miss Yi Wang, Miss. Yi Xu, Mr. Xinya Song, Miss. Jie Xiong, Dr. Min Zhou, Mr. Qian Yuan, for their countless help in the past three years. Thanks a lot for your friendship and I really treasure those good memories of being with you.

Finally, my deep appreciation goes to Mr. Hao Yang for his support, encouragement, quiet patience and unwavering love that were undeniably the bedrock. He is accompanying me through all those good and challenging time, and helping me grow into a mature, independent and optimistic person. I am forever grateful to my dear family: my parents, my sister and my brother, for their constant support, love and allowing me to be as ambitious as I wanted.

Table of Content

List of Figures

List of Tables

List of Abbreviations

TiO_2	Titanium dioxide
WS_2	Tungsten disulfide
LIBs	Lithium ion batteries
SIBs	Sodium ion batteries
NRR	Nitrogen reduction reaction
HER	Hydrogen evolution reaction
OER	Oxygen evolution reaction
ORR	Oxygen reduction reaction
SMSI	Strong metal−support interaction
DFT	Density functional theory
TMD	Transition metal dichalcogenides
XRD	X-ray diffraction
SEM	Scanning electron microscopy
TEM	Transmission electron microscopy
XPS	X-ray photoelectron spectroscopy
BET	Brunauer-Emmett-Teller
UV-Vis	Ultraviolet–visible spectroscopy
EIS	Electrochemical impedance spectroscopy
CV	Cyclic voltammetry
SEI	Solid electrolyte interface
OCV	Open circuit voltage
CE	Columbic efficiency

R_C	Charge-transfer resistance
W_1	Warburg impedance
Rs	Inter resistance of electrodes
SMSI	Strong metal-support interaction
EDX	Energy-dispersive X-rays
EPR	Electron paramagnetic resonance
PDF	Powder Diffraction File
FT	Fourier transform
XAS	X-ray absorption spectrum
FE	Faradaic efficiency
ICP-CVD	Inductively Coupled Plasma – Chemical Vapor Deposition
PVDF	Polyvinylidene fluoride
NMP	N-methyl-2-pyrrolidone
AC	Alternating current impedance
NH_3	Ammonia
MoS_2	Molybdenum disulfide
$LiCoO_2$	Lithium cobalt oxide
$LiMn_2O_4$	Lithium manganese (III, IV) oxide
$LiFePO_4$	Lithium iron phosphate
$LiPF_6$	Lithium hexafluorophosphate
$Li_4Ti_5O_{12}$	Lithiumtitanspinell
CNT	Carbon nanotube
SnO_2	Tin (IV) oxide
SiO_2	Silicon dioxide
Fe_2O_3	Iron (III) oxide
Fe_3O_4	Iron (II, III) oxide

CoO	Cobalt (II) oxide
Co_3O_4	Cobalt (II, III) oxide
Cu_2O	Copper(I) oxide
CuO	Copper (II) oxide
NiO	Nickel (II) oxide
Cr_2O_3	Chromium (III) oxide
RuO_2	Ruthenium (IV) oxide
MoO_2	Molybdenum dioxide
MoO_3	Molybdenum trioxide
CeO_2	Cerium (IV) oxide
ZnO	Zinc oxide
AgCl	Silver chloride
KCl	Potassium chloride
HCl	Hydrogen chloride
NaOH	Sodium hydroxide
NaClO	Sodium hypochlorite
$C_5FeN_6Na_2O$	Sodium nitroferricyanide

1. Introduction

In modern society, humans need to find some new high-efficient, low-cost, and environment friendly energy storage and conversion methods and materials because of the lack and non-renewable of the fossil fuels. Electrochemical energy storage and conversion devices that can realize efficient, environmental friendly and versatile use of energy are strongly considered with the increasing demand of portable devices, consumer electronics and electric vehicles[1]. Nowadays, the most widely used energy storage and conversion technologies are secondary batteries (such as lithium and sodium ion batteries), solar-driven catalysts and electrochemical fuel cells. However, new materials for energy storage and conversion are still not reach the demanding yet.

Since 2011, Chen and co-workers reported a novel hydrogenation treatment approach to generate hydrogenated TiO_2 (black TiO_2) nanoparticles with significantly enhanced optical absorption. And the new black TiO_2 possesses a disordered surface layer and increased surface functional groups, and shown superior photocatalytic activity compared with normal white TiO_2 [2]. And after this report, many works focus on the black TiO_2 materials application, such as lithium ion batteries, supercapacitors, fuel cells, field emission, photocatalytic application, cancer photothermal therapy and microwave absorption, etc [3–10].

At this stage, for the energy storage materials (especially LIBs and SIBs electrodes), researchers have already made a lot of efforts on the new electrode materials. The first efficient method to prepare high performance materials is reducing the materials size to nanoscale which can not only provide a short diffusion distance for electrons and ions transfer, but also lead to increased lifespan by withstanding the volume change during the electrochemical reactions [11]. And another popular method to modify the energy storage materials is that preparing composited materials.

Fuel cells, water electrolysis are another energy conversion and storage devices, and the performances of these devices are mainly limited by the electrochemical catalysts. Oxygen reduction reaction (ORR), hydrogen evolution reaction (HER), and oxygen evolution reaction (OER) are the most popular reactions that could be used for the water splitting process for the clean hydrogen energy preparation, but we didn’t focus on these. What we did is conversion of

atmospheric nitrogen into valuable substance such as ammonia because ammonia is considered as one of the most popular chemicals not only a very important source of nitrogen for fertilizer, exhibiting a strong foothold in agricultural, plastic and textile industries, but also a clean energy carrier and a potential transportation fuel [12–14]. Despite the high efficiency of Haber-Bosch (H-B) process, electrochemical nitrogen reduction reaction (NRR) to ammonia could be a good choice because of the mild reaction conditions without high temperature and high pressure.

Despite all these achievements, we found that many of the hydrogenation process for materials modification is just focused on TiO_2 or other oxides materials, and bare works about other kinds of materials or composite materials. In this dissertation, some new materials were prepared with different gases plasma treatment to gain the modified material with a disordered surface layer which could be used for different electrochemical applications. Chapter 4 introduced the hydrogenated WS_2 nanoparticles with an obvious disordered surface layer formation. When it is used as the anode materials for both lithium and sodium ion batteries, the electrochemical impedance spectroscopy (EIS) reveals a drastic decrease of the charge-transfer resistance for both LIB and SIB, which implies the plasma hydrogenated electrode is more favorable for the electron transportation during the electrochemical process. The improved rate performance of H-WS_2 in both applications of Li and Na ion batteries can be attributed to the reduced charge transfer resistivity at the disordered surface layer and improved electronic conductivity due the disorder surface in the crystalline structure. Chapter 5 shows a nitrogen doped TiO_2 (N-TiO_2) nanoparticles are prepared via nitrogen plasma treatment and investigated as anode material of sodium ion batteries. What is different from the other nitrogen doped TiO_2 reported in the literatures is that a disordered surface layer with the thickness of around 2.5 nm is formed on the N-TiO_2 nanoparticles surface after the N_2 plasma treatment, which is barely found with normal nitrogen doping processes. Both the doped nitrogen and the disordered surface layer play significant roles on enhancing the sodium storage performance. In chapter 6, we chose TiO_2-Au (P-TiO_2-Au, gold nanoclusters supported by P25 TiO_2 nanoparticles, Au load: ~ 2 wt %) as the electrochemical catalysts for the nitrogen reduction reaction. We modified the material with H_2 plasma and then formed a blue-black H-TiO_2-Au catalyst, it shown enhanced performance for the nitrogen reduction reaction (NRR) process comparing with the pristine sample. The DFT calculation results confirm that H-TiO_2-Au with oxygen vacancies and disordered surface layer is much preferred for the NRR process. It further proves that the reduction process of H_2 plasma treatment makes an important role on the improving of catalysts' performances. Chapter 7 made a conclusion of all the works and gave an outlook of

the future plans as well. And we thought all the excellent performance improvements which are attributed to the plasma treatment with a disordered surface layer formation for energy storage materials is proved to be quite effective. We could use different gases which results in different elements doping and disordered surface at the same time, which show a double enhancement for the electrochemical application performances.

2. Fundamentals and review of state of the art

2.1 Energy storage materials

2.1.1 Lithium ion Battery

Usually, a battery includes an anode, cathode, separator and electrolyte, as shown in Scheme 2-1, during the discharge process, electrode reactions occur at the electrode and generated electrons flow through an external circuit to power load; during charge process, an external voltage is applied between electrodes driving electrode reactions occur reversibly. Nowadays the current cathode materials is represented by $LiCoO_2$, $LiMn_2O_4$, $LiFePO_4$ and $Li[Ni_xCo_yMn_z]O_2$ (x+y+z=1) [15,16]. And the electrolyte is usually as ionic and electronic conductor, which is mainly based on solutions of $LiPF_6$ dissolved two or more organic carbonate solvents for the balance of fluidity and dielectric constant [17].

In general, there are three different kinds of active anode materials for lithium ion batteries. (1) insertion /de-insertion materials, this mainly consists of carbonaceous materials [18–21] and Ti-based oxides, such as TiO_2 or $Li_4Ti_5O_{12}$ [22–24]. This type of anode materials usually shows good cycling stabilities with low theoretical capacities. (2) Alloy/de-alloy materials, like Si, Ge, Sn, Zn, SnO_2 and SiO_2 [25–32]. Alloy anode materials possess high specific capacities and energy density, but usually show a large irreversible capacity and poor cycling performance. (3) Conversion materials, especially metal oxides (Fe_2O_3, Fe_3O_4, CoO, Co_3O_4, Mn_xO_y, Cu_2O/CuO, NiO, Cr_2O_3, RuO_2, MoO_2/MoO_3) and metal phosphides/sulfides/nitrides (MXy; M=Fe, Mn, Ni, Cu, Co etc. and X = P, S, N) [11,33–40]. Conversion materials have the similar properties of alloy materials, high capacity, high energy, and also low cost, low operation potential and low polarization than counter oxides. However, the coulombic efficiency and poor cycle life limit the wide applications of them.

Among all of these anode materials, graphite is the most commercial used anode material for the secondary batteries at this moment because of the flat and low working potential, low cost, long cycling life and so on [16]. However, carbon material has a big problem that the discharge voltage is much lower for the lithium ion batteries, and this may cause some safety problems for the battery

system. What's more, the power density of carbon materials is quite low. There is an urgency to replace graphite anode to materials with higher capacities, energy and power densities.

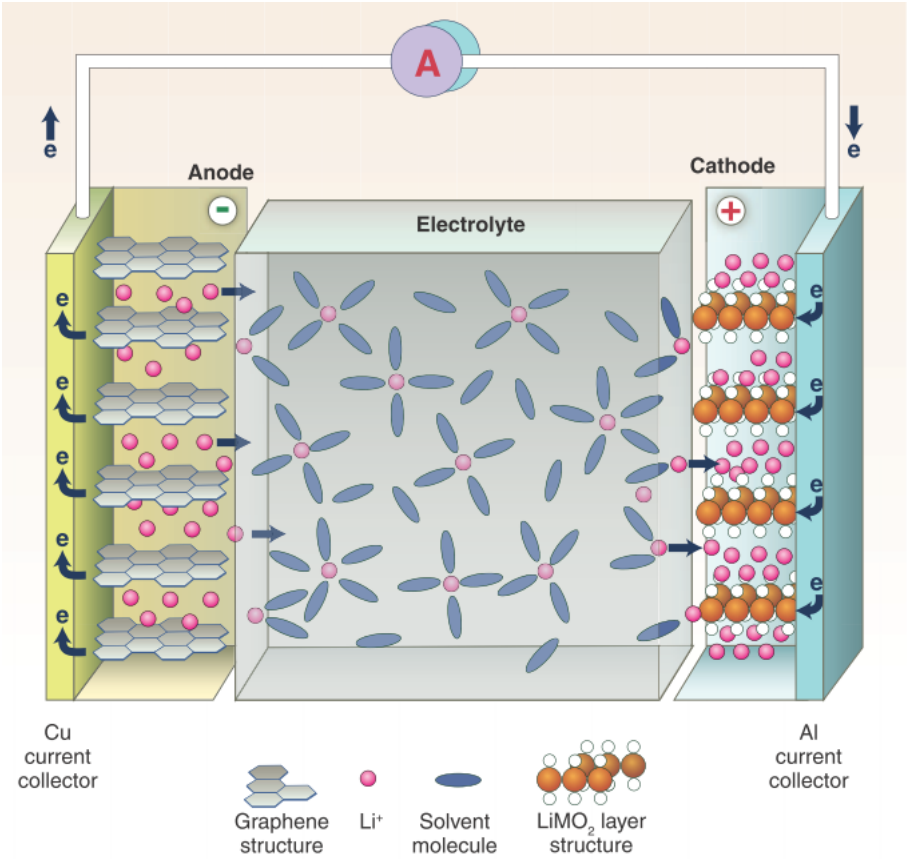

Scheme 2-1 Illustration of a lithium ion battery system. Reprinted from [41].

At this moment, all kinds of carbon and non-carbon anode materials for lithium ion batteries have already been researched a lot. Several strategies are developed to achieve high performance materials, firstly, nanostructured materials exhibit admirable properties when applied in the batteries compared to bulk materials, such as high specific surface area, controllable micro-morphology and high electronic and ionic conductivity and low diffusion distance [16,42]. Secondly, coating or combining the buffering matrix or conductive materials is another way to relieve the severe problems, especially improving the conductivities of the electrodes [43–46]. Various carbon materials like carbon nanotubes, graphite nanosheet have already been studied for the matrix and combining with other anode materials.

Tremendous efforts have been made in searching for alternative anode materials. Several candidates such as metals, semimetals and metal oxide have been investigated. Among them, transitional metal dichalcogenides (TMD), especially WS_2 and MoS_2, have received enormous

attention owing to their unique physical and electrochemical properties [47–53]. Compared to MoS_2, tungsten disulfide (WS_2) has a much larger interlayer spacing of (002) facial (0.62 nm) and weak van der Waals interaction, this would highly favor the Li^+ and Na^+ intercalation/ deintercalation. Layered metal sulfides also behave better rate capacity and cycling performance than silicon or metal oxides. The mechanism has not been clearly identified till now. Nevertheless, since the two dimensions nanosheets are loosely stacked, layered metal sulfides can further accommodate volumetric expansion upon lithium storage and mitigate strain endured in the conversion or alloy reaction, leading to much enhanced cycling stability. In addition, properly designed nanostructure metal sulfides are capable of being deployed at high current densities. In contrast to intercalation electrodes as in the case of graphite anode, most of the transition metal sulfide anodes accommodate lithium ions through conversion reaction mechanism in voltage below 1.5 V vs. Li/Li^+. The advantage of the conversion reaction mechanism is that it may deliver higher energy density than intercalation mechanism-based compounds. Nevertheless, the significant disadvantage of the conversion reaction mechanism is to cause a large volume expansion of electrode materials during the discharge/charge process in the first cycle. This remains a serious issue leading to cracking, fracture, and electrical disconnection from current collectors, which have been recognized as the major causes for rapid capacity fading in LIBs.

2.1.2 Sodium ion Battery

Lithium ion batteries (LIBs) are much more popular at the moment because of the high energy density and long cycling performance. While there are still some shortcomings, especially the high cost of lithium will limit its wide application in the future. In the meantime, SIBs have attracted much attention because sodium is an abundant alkali element widely distributed in the world. Similar to lithium ion batteries, SIBs comprise of an anode(reductant), a cathode(oxidant) and an electrolyte-soaked-separator placed in between (Scheme 2-2). For the cathode materials of SIBs, layered Oxides, polyanion compounds, organic compounds play significant roles [10]. For anode materials, carbonaceous materials is an important choice which is very cheap, however carbonaceous materials show undesired properties with low capacities and /or poor cycle performance [54] Ti-based materials is a promising anode materials for sodium ion batteries , including $Na_2Ti_3O_7$, $Na_{0.66}[Li_{0.22}Ti_{0.78}]O_2$, $Li_4Ti_5O_{12}$, and TiO_2 [10]. Moreover, other materials based on alloying reactions (such as Sn, Sb, P and their compounds e.g. inter-metallics, oxides, sulfides, and phosphides) and correction reactions

(oxides and sulfides, e.g. Fe_2O_3, Fe_3O_4, FeOOH, MoO_3, CuO, Mn_3O_4, $NiCo_2O_4$ and MoS_2) [10] attract some attentions as well. In addition, organic compounds are also potential anode materials for sodium ion batteries.

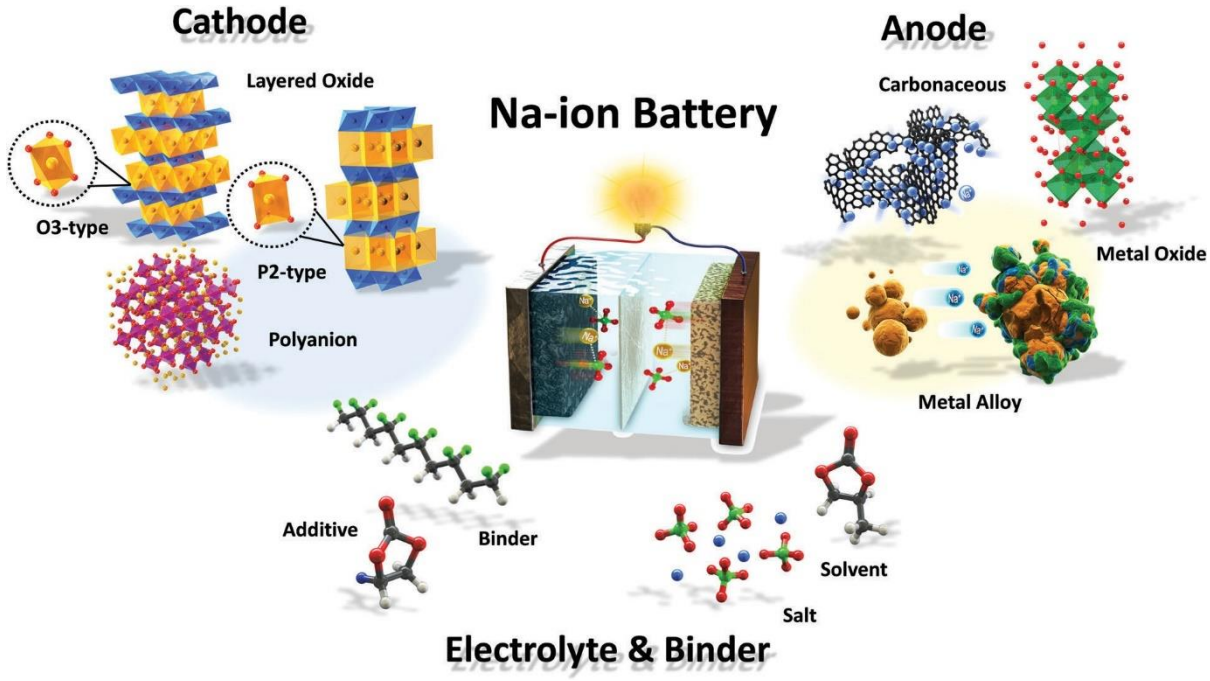

Scheme 2-2 Illustration of a sodium ion battery system. Reprinted from [55].

However, the ion radius of Na ions are ~70% larger than that of Li ions, a big challenge for the development of SIBs is to find proper electrode materials with big interstitial space to accommodate sodium ions and allow reversible and rapid ion insertion/extraction [56]. TiO_2 has already been considered as one of the great energy storage materials due to its low cost, intrinsic safety, high power density and long cycle life. TiO_2 has a lower average potential for Na storage (0.7V vs. Na/Na^+), which is more beneficial to improve the sodium storage performance[57]. Until now, there are a lot of research works about TiO_2 as anode for secondary batteries [58,59]. Poor electrical conductivity and low sodium ion diffusivity are the main limits for the wide application of TiO_2 as anode for sodium ion batteries. The same as other materials, the first and most useful approach to solve the main problem of TiO_2 electrical conductivity is trying to design nano-sized or morphology control TiO_2, for example nanoparticles [60], nanotubes [61], nanofiber[62], petal-like TiO_2 [63]and nanorods [64], as the nanosized morphology or structure could effectively shorten the ion diffusion path and enlarge the active area of the material. Zhang et al. synthesized a novel flexible and freestanding oxygen-deficient TiO_{2-x} nanocages anchored in N-doped carbon fibers, which

exhibited a high areal capacity and an outstanding stability for sodium storage [65]. He et al. reported a hierarchical rod-in-tube TiO_2 with a uniform carbon coating as the anode material for sodium-ion batteries by a facile solvothermal method. The author claimed that this unique structure consists of a tunable nanorod core, interstitial hollow spaces, and a functional nanotube shell assembled from two-dimensional nanosheets[66]. Then surface coating could be another good method to improve the TiO_2 conductivity, especially there are a lot of research works that introduced carbon additives to enhance the electrical conductivity of TiO_2 for SIBs, like amorphous carbon, CNTs and graphene are widely introduced as conductive agents [65,67–71]. What's more, heteroatom doping (N, S or Nb [72–76]) is also considered as an effective strategy to boost the conductivity, in which the produced oxygen vacancies or trivalent titanium species can be formed to improve the electrical conductivity. Yu et al. reported that the introduction of nitrogen into TiO_2 could result a partial formation of Ti^{3+} associated with the oxygen vacancies, which lead to reduce sodium ion and electron transport diffusion resistance and improve the rate capacity [72]. A nitrogen-doped carbon layer coated yolk-like TiO_2 electrode could offer a superior high capacity of 115.9 $mAh \cdot g^{-1}$ at 20 C (6700 $mA \cdot g^{-1}$)[77]. It is clear that the key to improve the electrochemical performance of TiO_2 is to combine strategies of shortening sodium-ion diffusion distance and improving electronic conductivity. However, all the researched work could not reach the high demanding of the novel SIBs electrodes yet, finding some easy operated and effective method for materials modifications is still a burning question.

2.1.3 Electrochemical Catalysts for Nitrogen Reduction Reaction

Ammonia is considered as one of the most popular chemicals not only a very important source of nitrogen for fertilizer, exhibiting a strong foothold in agricultural, plastic and textile industries, and also a clean energy carrier and a potential transportation fuel [12–14]. The reduction of N_2 to produce NH_3 is a great way for N_2 fixation because of the unlimited sources of N_2 from the air. However, as we all know that N_2 has the extremely high bond energy (about 940.95 $kJ \cdot mol^{-1}$), the reduction of N_2 to NH_3 is a kinetically complex and energetically challenging multistep reaction [78,79]. In general, ammonia was produced by the Haber-Bosch (H-B) process with the Fe-based catalyst for industry, which usually required a strictly conditions of high temperature and high pressure [80,81]. The strict demanding of H-B process of producing the ammonia impels researcher to creating some other alternative approaches for ammonia synthesis, for example biological methods, plasma-induced methods, methods based

on metal-complexes, photocatalytic methods and electrochemical methods [82–87]. So far, numerous research work has already been done to pursuit a mild way for N_2 fixation, but there are still many drawbacks, such as expensive electrolytes [88], harsh reaction conditions [85] and low yields [89].

Electrochemical reaction for ammonia synthesis has already attracted much attention because of several advantages such as requiring a mild condition instead of high temperature and pressure, enabling alternative energy sources and having appreciable energy efficiency. Also, it is a good method which can save more than 20 % of the energy consumption compared to the conventional H-B process [90]. At the present, there are kinds of catalysts which have already been synthesized for the application of the electrochemical reduction of N_2 to ammonia. Firstly, biological catalysts are quite normal for the nitrogen fixation, because the biological nitrogen fixation processes occur naturally in diazotrophic microorganisms through the enzyme nitrogenase. Secondly, some transition metal oxides could be used for the electrochemical reduction of nitrogen, but only several NRR electrocatalysts have been researched, including MoO_3 [91], Fe_2O_3/CNT [92] $Bi_4V_2O_{11}/CeO_2$ [93], etc. What's more, noble metals, for example Au [94], Ru [85]and Rh [95], based catalysts show attractive activity for the NRR, but these are limited for wide using because of the high cost. Lastly, conducting polymers/metal-phthalocyanine complexes have been reported for electrocatalytic NRR at ambient conditions [96]. What's more, a majority of NRR researches report very low Faradic efficiency of <1% even at elevated temperature or pressure [92,97]. Although it is reported that notable Faradic efficiency of ~35 % for NRR has already been achieved, this requires an additional input energy to sustain the high temperature (200 °C) and high pressure (>25 bar) [13] Another thing is that in theory, the electrochemical reduction of N_2 gas will be proceed at negative potentials, which is similar to those required by the H_2 evolution reaction related to the thermodynamics of N_2 and NH_3. It would be a big problem about the unwanted HER reaction since most current densities observed in the experiments for the NRR were due to the hydrogen reduction reaction side reaction. In this case, gold (Au) attract the most attentions as a good catalysts for NRR processes because of the low HER activity of gold [94]. Bao and co-workers demonstrated that the electrochemical reduction of N_2 to NH_3 at ambient conditions is indeed possible by using tetrahexahedral Au nanorods as an electrocatalytic catalyst, even without the aid of activating complexes in the electrolyte. The reduction product yield rates are found to be as high as 1.648 and 0.102 $\mu g\ h^{-1}\ cm^{-2}$ for NH_3 and $N_2H_4{\cdot}H_2O$, respectively [98]. However, to effectively utilize the high cost and desired Au, preparing metal particles onto oxide supports to obtain a

well catalyst system has been proved to a great method for considerable catalytic performances. Thus, TiO_2 could be a good choice due to the low cost and high stabilities. Further, black TiO_2 was consider valuable for photocatalysts [99–102], as well as secondary batteries [103] and supercapacitors[7], because black TiO_2 presents surface oxygen vacancies, disordered surface of point defects and sometime with Ti^{3+} ions, which could give great contributions when used as a electrochemical catalysts. At this moment, there are seldom works which used black TiO_2 nanoparticles as the support for gold nanoclusters working as electrochemical nitrogen reduction reaction catalysts.

2.2 Plasma treatment modification for energy storage and conversion devices materials

Recently, it has been demonstrated that the performance of the semiconductor metal oxides nanomaterials, such as titanium dioxide (TiO_2), zinc oxide (ZnO), tungsten trioxide (WO_3), tin oxide (SnO_2) and copper oxide (CuO) for the applications as electrode materials in energy conversion and storage or related field was clearly improved after the hydrogenation treatment [104–108]. This approach is usually based on thermal annealing in H_2 gas, and has been proved that can incorporate a large amount of oxygen vacancies or Ti^{3+} species and introduce a disordered surface layer in the crystalline structure, resulting in an enhanced electrical conductivity and conversion rate [109]. In 2011, Chen and co-workers reported a hydrogenated TiO_2 with enhanced performance as anode material for LIBs, and they argued that the surface-disordered structure is beneficial to the charge-transfer process and the capacity retention of the electrodes. Because the charge transfer process with the conductive carbon and flexible structure in the disordered layer become faster and the smaller structural distortion can allow the larger capacity retention and longer lifetime of the electrode [110]. In addition, Yan et al. has used H_2 plasma to induce the hydrogenation with dramatically enhanced efficiency, controllability and safety, and the hydrogenated TiO_2 nanoparticles showed an excellent fast lithium storage performance. In this work it was claimed that the improved rate performance can be attributed to the enhanced contribution of the pseudocapacitive lithium storage at the surface, and the formed disordered surface layer and the incorporated Ti^{3+} species have played important roles in the enhanced pseudocapacitive lithium storage[103]. It is also reported that hydrogenation can improve the capacitance of ZnO electrode used in supercapacitors. The free-carrier concentration and electrical stability can be improved via introduce hydrogen in the ZnO lattice as a shallow donor [111,112].

What's more, the plasma treatment method is mainly focused on semiconductor metal oxides nanomaterials, there is not too much work about other kind of materials. In addition, the big difference between plasma treatment and normal gas annealing process is that normal annealing process couldn't form an ultra-thin disordered surface on the samples, and the disordered surface layer plays a significant role on enhancing the performances of the materials. And also, the varieties of plasma treatment gases are quite limited. In order to prepared some extraneous element doping material with a disordered surface layer at the same time, we used nitrogen plasma treatment to modify energy storage materials, which could achieve a nitrogen doped materials and a disordered surface layer could be formed at the same time. Also, we tested the plasma treatment effect on transitional metal dichalcogenides (TMD) WS_2 and composite TiO_2-Au materials, all of them show a promising improvement for the energy storage applications after the plasma treatment with a disordered surface layer formation.

3. Experiments and Methods

3.1 Synthesis of hydrogenated WS_2 as anode for lithium and sodium ion batteries

3.1.1 Samples preparation

Commercial WS_2 nanoparticles with average particle size of 90 nm were purchased from Graphene Laboratories, Inc. Because of the convenience of fabrication and almost no waste of material, drop casting was used to disperse the powder more homogeneously. Hereby, 0.10 g WS_2 nanoparticles were dispersed in 30 ml ethanol with an ultrasonic condition and drop-cast onto a 6-inch Si wafer. The drop casting process was repeated several times to achieve WS_2 mass loading of 0.5-0.6 $mg \cdot cm^{-2}$ (sample mass loading should no more than 1.5 $mg \cdot cm^{-2}$ to avoid sample nanoparticles shedding from the surface of Si wafer in the hydrogenation process) [103]. Before each drop, the previous dropped ethanol must be volatilized totally so that a homogenous distribution of powder on the silicon wafer can be obtained.

The drop-casted wafer was transferred into a chamber for plasma-enhanced hydrogenation treatment, and there an instrument of inductively coupled plasma (Plasmalab 100 ICP-CVD, Oxford Instruments) was used. Before hydrogenation, the chamber must be cleaned to make sure the development of a reproducible process and thus fewer impurities can be found in the reaction chamber. A preconditioning must be held afterwards at 300 °C to ensure the quality of plasma treatment. Then, the H_2 plasma treatment was performed at 300 °C for 2 hours, the ICP power was 3000 W, the chamber pressure was 3.52-3.76 Pa, and the H_2 flow rate was 50 sccm. After this treatment, WS_2 were obtained and scratched from Si wafer for further investigations.

3.1.2 Electrochemical experiments

For the electrochemical measurements of lithium and sodium ion batteries, 2032 type coin cells were assembled in an argon-filled glove box, where both the moisture and oxygen contents were < 0.5 ppm. The working electrode was prepared in the ratio of 80: 10: 10 (w/w) active

material/super carbon black/polyvinylidene difluoride (PVDF), to form a homogeneous slurry in N-methyl-pyrrolidone (NMP). The slurry was then deposited as a film with a thickness of 100 μm on a copper foil using a coating machine from Zehntner Testing Instrument. The electrode was dried for 12 h at 120 °C under vacuum and the working electrode loading was about 2 $mg \cdot cm^{-2}$. Glass fiber (GF/D, Whatman) was used as a separator, and pure lithium foil (or sodium foil) (Aldrich) was used as the counter electrode. The electrolyte was 1 M $LiPF_6$ (or $NaPF_6$) in a 50:50 w/w mixture of ethylene carbonate and dimethyl carbonate. A battery tester (Neware, Shenzhen, China) was used to conduct the galvanostatic measurement. Cyclic voltammetry (CV) was carried out over the potential range to 3.0 to 0.01 V using a potentionstat (VMP3, BioLogics, France). The AC impedance of the samples was determined using the same potentiostat, and impedance spectra were obtained by applying a sine wave with an amplitude of 5.0 mV over the frequency range of 100 kHz to 0.01 Hz after charging/discharging for 5 cycles at a certain current density.

3.2 Synthesis of nitrogen doped TiO_2 as anode for sodium ion batteries

3.2.1 Sample preparation

Commercial TiO_2 (P25) nanoparticles were purchased from Sigma-Adlrich and used without further purification. Because of the convenience of fabrication and almost no waste of material, drop casting was used to disperse the powder more homogeneously. Hereby, 0.10 g TiO_2 nanoparticles were dispersed in 30 ml ethanol with an ultrasonic condition and drop-cast onto a 6-inch Si wafer. The drop casting process was repeated several times to achieve TiO_2 mass loading of 0.5-0.6 $mg \cdot cm^{-2}$ (sample mass loading should no more than 1.5 $mg \cdot cm^{-2}$ to avoid sample nanoparticles shedding from the surface of Si wafer in the nitrogen plasma treatment process) [8,107,108]. Before each drop, the previous dropped ethanol must be volatilized so that a homogenous distribution of powder on the silicon wafer can be obtained. The drop-casted wafer was transferred into a chamber for plasma-enhanced nitrogen plasma treatment, and there an instrument of inductively coupled plasma (Plasmalab 100 ICP-CVD, Oxford Instruments) was used. Before the plasma treatment process, the chamber must be cleaned to make sure the development of a reproducible process and thus fewer impurities can be found in the reaction chamber. A preconditioning must be held afterwards at 300 °C to ensure the quality of plasma treatment. Then, the N_2 plasma treatment was performed at 300 °C for 30 minutes, the ICP power was 3000 W, the chamber pressure was 3.52-3.76 Pa, and the N_2 flow rate was 30 sccm.

After this treatment, N-TiO_2 were obtained and scratched from Si wafer for further investigations.

3.2.2 Electrochemical experiments

The electrochemical performances of the materials used as anode for sodium-ion batteries were tested via 2032 type coin half-cells, which were assembled in an argon-filled glove box, where the moisture and oxygen contents both were less than 0.5 ppm. The working electrode was immersed in a mixture, which consist of active material, super carbon black and polyvinylidene in ratio of 70: 15: 15, toward forming a homogeneous slurry in N-methyl- pyrrolidone (NMP). Then, the slurry was pasted onto stainless steel foil with a sample loading of about 1.8 $mg \cdot cm^{-2}$. The handled electrode was dried for 12 h at 120 °C under vacuum. Glass fiber (GF/D, Whatman) and pure sodium foil (Aldrich) were respectively used as a separator and the counter electrode. The electrolyte was 1 M $NaPF_6$ in a mixture of ethylene carbonate and diethyl carbonate, in a ratio of 50:50. For the galvanostatic measurement, a battery tester (Neware, Shenzhen, China) was used. Cyclic voltammetry (CV) was applied in a potential range from 3.0 to 0.01 V at a scan rate of 0.5 $mV \cdot s^{-1}$ by a potentionstat (VMP3, BioLogics, France). Furthermore, the alternating current (AC) impedance of the samples were determined by a same potentiostat and the impedance spectra, which was acquired via a sine wave with an amplitude of 5.0 mV in a frequency range from 100 kHz to 0.01 Hz after charging/discharging for 5 cycles at a current density of 1 $A \cdot g^{-1}$.

3.3 Synthesis of hydrogenated TiO_2-Au nanoparticles as electrocatalyst for nitrogen reduction reaction

3.3.1 Samples preparation

The pristine TiO_2-Au (P-TiO_2-Au, gold nanoclusters supported by P25 TiO_2 nanoparticles, Au load: ~ 2 wt %) was purchased from Particular GmbH (Germany) and used without any purification. 100 mg of P-TiO_2-Au powder was dispersed into 30 mL ethanol under an ultrasonic condition to get a homogenous ink and then drop cast onto a 6-inch Si wafer. The drop-casted wafer was transferred into a chamber for plasma-enhanced hydrogenation treatment. The drop-casted wafer was transferred into the inductively coupled plasma

(Plasmalab 100 ICP-CVD, Oxford Instruments) chamber for plasma-enhanced hydrogenation treatment. Before hydrogenation, the chamber must be cleaned to make sure the development of a reproducible process and thus little impurities can be found in the reaction chamber. A preconditioning must be held afterwards at 300 °C to ensure the quality of plasma treatment. Then, the H_2 plasma treatment was performed at 300 °C for 2 hours, the ICP power was 3000 W, the chamber pressure was 26.5-28.3 mTorr, and the H_2 flow rate was 50 sccm. After this treatment, hydrogenated TiO_2-Au (H-TiO_2-Au) were obtained and scratched from Si wafer for further investigations. The same modification was processed on the H_2 and O_2 plasma treated material (H-O-TiO_2-Au) just an O_2 plasma treatment for 5 minutes with a power of 100 W with a Tefal O_2 plasma set up afterwords. The P-TiO_2-Au was used as the control sample during the experiments.

3.3.2 Electrochemical measurements

1. Cathode preparation

Typically, 4 mg samples and 5 μL of Nafion solution were dispersed in 100 μL ethanol and 100 μL ultra-pure water by sonicating for 30 minutes to form a homogeneous ink. Then the ink was loaded onto a carbon paper (Toray 090) with an area of 2×2 cm and dried under vacuum at room temperature overnight.

2. NRR electrochemical measurements

The N_2 reduction reaction electrochemical measurements were carried out with an electrochemical workstation using a three-electrode configuration with TiO_2-Au working electrode, Pt foil counter electrode and Ag/AgCl (saturated KCl electrolyte) reference electrode, respectively. The electrolyte is 0.1 M HCl with N_2 saturated for 30 minutes before the test. The reference electrode was calibrated on reversible hydrogen electrode (RHE). The calibration was performed in the high purity hydrogen saturated electrolyte with Pt foils as both working electrode and counter electrode in 0.1 M HCl electrolyte. Cyclic voltammetry tests were run at a scan rate of 0.5 $mV \cdot s^{-1}$, and the average value of the two potentials at which the H_2 oxidation/evolution curves crossed at I = 0 was taken to be the thermodynamic potential for the hydrogen electrode reactions. Thus, in 0.1 M HCl, E (RHE) = E (Ag/AgCl/saturated KCl) + 0.28 V in my work.

3. Determination of ammonia

The determination of the produced ammonia was carried by the indophenol blue method with some modification. Firstly, 2 mL of solution was removed from the electrochemical reaction vessel, and subsequently, 2 mL 1M NaOH solution containing 5 wt % salicylic acid and 5 wt % sodium citrate, followed by addition of 1 mL of 0.05 M NaClO and 0.2 mL of an aqueous solution of 1 wt % $C_5FeN_6Na_2O$ (sodium nitroferricyanide). After 2 h at room temperature, the absorption spectrum was measured using an ultraviolet-visible spectrophotometer. The formation of indophenol blue was determined using the absorbance at a wavelength of 655 nm. The concentration-absorbance curves were calibrated using standard ammonia chloride solutions, which contained the same concentrations of HCl as used in the electrolysis experiments. And then we used the UV-Vis spectrophotometer of every sample and the fitting calibration cur to gain the amount of the ammonia which was produced during the NRR process.

4. Faradaic efficiency

The Faradaic efficiency for NRR was defined as the quantity of electric charge used for synthesizing ammonia divide the total charge passed through the electrodes during the electrolysis. The total amount of NH_3 produced was measured using colorimetric methods. Assuming three electrons were needed to produce one NH_3 molecule, the Faradaic efficiency can be calculated as follows: Faradaic efficiency = $3F\times cNH_3\times V/(17\times Q)$, where F is the Faraday constant. The rate of ammonia formation was calculated using the following equation: $vNH_3= (cNH_3\times V)/(t\times m)$, Where cNH_3 is the measured NH_3 concentration, V is the volume of electrolyte, t is the reduction reaction time and m is the catalyst mass.

3.3.3 Calculation method

The first-principle calculations were performed with the Vienna Ab initio Simulation Package (VASP). The ion-electron interactions were treated with the projected-augmented wave (PAW) method. The exchange-correlation interactions were calculated with the Perdew–Burke-Ernzerhof (PBE) scheme. The energy cut-off was set to 400 eV, and the self-consistent convergence was set at criteria of 0.0001 eV/atom. The spin polarization was considered in the calculation.

The Norskov's computational hydrogen electrode (CHE) method was applied to calculate the reaction free energy (△G) for nitrogen reduction reactions (NRR). In the method, with the

standard conditions (pH=0, p = 1 bar, T = 298 K), the △G of the reaction: $A^* + H^+ + e^- \rightarrow AH^*$, could be calculated from the reaction: $A^* + 1/2\ H_2 \rightarrow AH^*$, i.e., △G= G (AH*) –G (1/2 H_2) –G (A*) + eU'. Here U is the electrode potential vs. SHE, and in alkaline condition, the formula between U' and U is U' = U + 0.059*(pH).

3.4 Central analytics tools for materials characterizations

The crystalline structure of the nanoparticles was characterized by X-ray diffraction (XRD, SIEMENS D5000) using Cu-Kα radiation. The samples were characterized by using transmission electron microscopy (TEM, Tecnai F20). Scanning electron microscopy (SEM) images were taken with a Hitachi S-4800 instrument, where also energy-dispersive x-ray spectrometry (EDS) was carried out. The optical absorption in the range from UV to the visible wavelength was measured by a diffuse reflectance accessory of a UV-Vis spectrometer (Cary 5000 UV-Vis-NIR). The X-ray photoelectron spectroscopy (XPS) analysis was performed by a spectrometer (Kratos Axis Ultra XPS) with monochromatized Al-Kα radiation and an energy resolution of 0.48 eV. Raman spectra analysis was performed with a Renishaw In-Via System utilizing a 514.5 nm incident radiation and a 50 × aperture (N.A. = 0.75), resulting in an ~ 2 μm diameter sampling cross-section. Electron paramagnetic resonance (EPR) spectra were recorded at the temperature of 77 K using a Bruker BioSpin CW X-band (9.5 GHz) spectrometer ELEXYS E500. Au LIII-edge extended X-ray absorption fine structure (EXAFS) data were acquired at the 1W1B beamline of the Beijing Synchrotron Radiation Facility, China. The electron beam energy of the storage ring was 2.5 GeV with a stored current of 200 mA. Au foil was used as reference sample and data were obtained in transmission mode, while data for the TiO_2-Au catalysts were acquired in fluorescence mode. The data were processed and analyzed using the Demeter 0.9.25 software package.

4. Disordered Surface Formation of WS_2 via Hydrogen Plasma with Enhanced Anode Performances for Lithium and Sodium Ion Batteries

4.1 Introduction of transition metal dichalcogenides as anode materials

Nowadays, high performance energy storage devices have attracted amount of attentions because of the growing power-supply demand in the fields of portable electronics, electric vehicles and grid energy storage systems[114–117]. Among these energy storage devices, rechargeable lithium ion batteries (LIBs) and sodium ion batteries (SIBs) are the most important groups due to their high energy densities, environmental friendly, memoryless effect and long cycle life [118–121]. LIBs are the wildest used energy storage method in the market now, what's more, SIBs also own a high potential to apply in smart-grid because of the high abundance nature resources and low cost. However, because the radius of sodium ions is larger than the lithium ions, SIBs may have some greater disadvantages than LIBs, for example, a lower specific capacity and larger volume change during charging/discharging process [122,123]. For these reasons, considerable attention has been paid to investigate suitable electrode materials as anode materials for both lithium and sodium ion batteries with a higher rate and long cycling performances [121,124–127].

Among the lithium and sodium anode materials, transition metal dichalcogenides (TMD) nanoparticles attract much attention in recent lithium and sodium ion batteries (LIBs and SIBs) due to its layered structure, which act as host lattices when reacting with ions to yield intercalation compound. Transitional metal dichalcogenides (TMD), especially WS_2 and MoS_2, have received enormous attention owing to their unique physical and electrochemical properties [47–53]. Compared to MoS_2, tungsten disulfide (WS_2) has a much larger interlayer spacing of (002) facial (0.62 nm) and weak van der Waals interaction, this would highly favor the Li^+ and Na^+ intercalation/ deintercalation. In addition, WS_2 has a relatively higher theoretical specific capacity of 432 $mAh \cdot g^{-1}$ than the commercial graphite for LIBs. Due to its great advantageous features, WS_2 has already been studied as energy storage devices, transistors, catalysts and photo-sensor devices [128]. However, bottlenecks such as the reversal of decomposition in terms of

reactivity, mass transport and nucleation, the poor electronic conductivity and the substantial large volume change during charging-discharging process hinder the further development and application of tungsten disulfide in batteries [50,129–131]. Therefore, developing novel nano-size structure materials to reduce the diffusion length of Li^+ and Na^+ is an effective way to increase the anode capacities and subsequent energy density of batteries [132,133]. Secondly, synthesizing some carbonaceous composite material is also a good way to increase the conductivity and reduce the volume change during the charging/discharging processes [38,131,134–138]. Despite these achievements, there are still many difficulties for researchers to get some novel WS_2 materials without any other complicated materials which showed not only a considerable electrochemical performance, but also an easy operation method to modify the pristine materials. In this chapter, WS_2 nanoparticles are modified through hydrogen plasma treatment at 300 °C for 2 hours, and the hydrogenated WS_2 (H-WS_2) nanoparticles demonstrate a clearly enhanced electrochemical performance as anode material for LIBs and SIBs. The TEM investigation shows a disordered surface layer with thickness around 2.5 nm after the treatment, and this is also confirmed by the results of the Raman spectroscopy. The shift in the XPS peaks indicates the structure surface disorders are incorporated in the crystalline structure. The hydrogenated WS_2 based LIBs and SIBs possess significantly higher specific capacity at different current densities. In addition, the electrochemical impedance spectroscopy (EIS) reveals a drastic decrease of the charge-transfer resistance for both LIB and SIB, which implies the plasma hydrogenated electrode is more favorable for the electron transportation during the electrochemical process. The improved rate performance of H-WS_2 in both applications of Li and Na ion batteries can be attributed to the reduced charge transfer resistivity at the disordered surface layer and improved electronic conductivity due the disorder surface in the crystalline structure.

4.2 Results and discussion

4.2.1 Characterizations

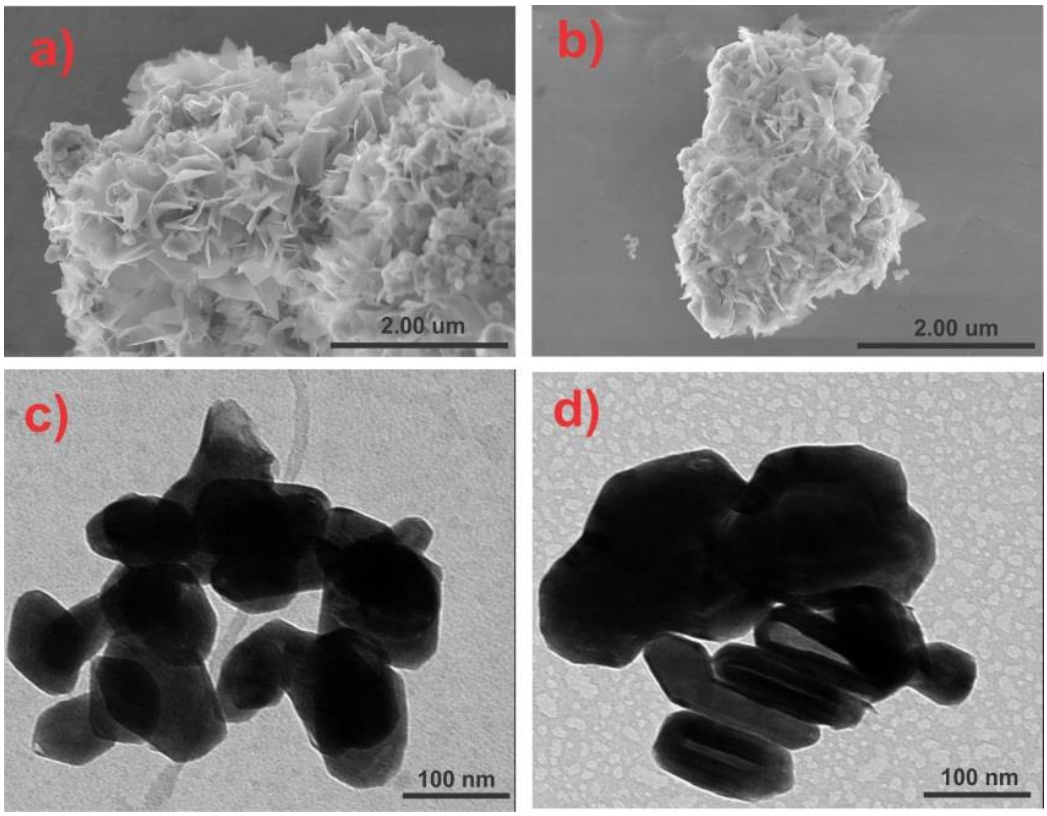

Figure 4-1 (a) (c) SEM and TEM images of pristine WS_2; (b)(d) SEM and TEM images of H-WS_2.

The microstructures of the samples were investigated by the scanning electron microscopy (SEM) and transmission electron microscopy (TEM). As displayed in Figure 4-1, pristine and H-WS_2 nanoparticles have typical sizes of around 100 nm. The morphology of the materials before and after hydrogen plasma treatment has no big differences. Figure 4-2 shows the HR-TEM images of pristine and H-WS_2 nanoparticles. In order to get further structural information, we zoom in the region near the edges. Both the pristine and H-WS_2 nanoparticles are highly crystallized. Combing the results in the FFT images of the whole regain of the sample (insets), the lattice fringes with the d spacing are 0.617 nm and 0.627 nm before and after hydrogenation, respectively. These values correspond well to the (002) plane of WS_2. It is interesting to notice that a disordered layer (~2.5 nm) was formed on the surface of H-WS_2 nanoparticles along the c-axis after hydrogenation. The thickness of the formed disordered layer in the WS_2 is clearly

larger than that (around 1.3 nm) reported in H-TiO_2 [113]. The disordered surface layer could be formed more easily along the c-axis of the WS_2 due to the weak van der Waals bonding. Also, the crossover of the fringes indicates a partially dislocation in the H-WS_2 nanoparticles. However, we can't conclude that whether the pristine WS_2 nanoparticles or hydrogenated WS_2 nanoparticles has more dislocations due to the limitation of the images.

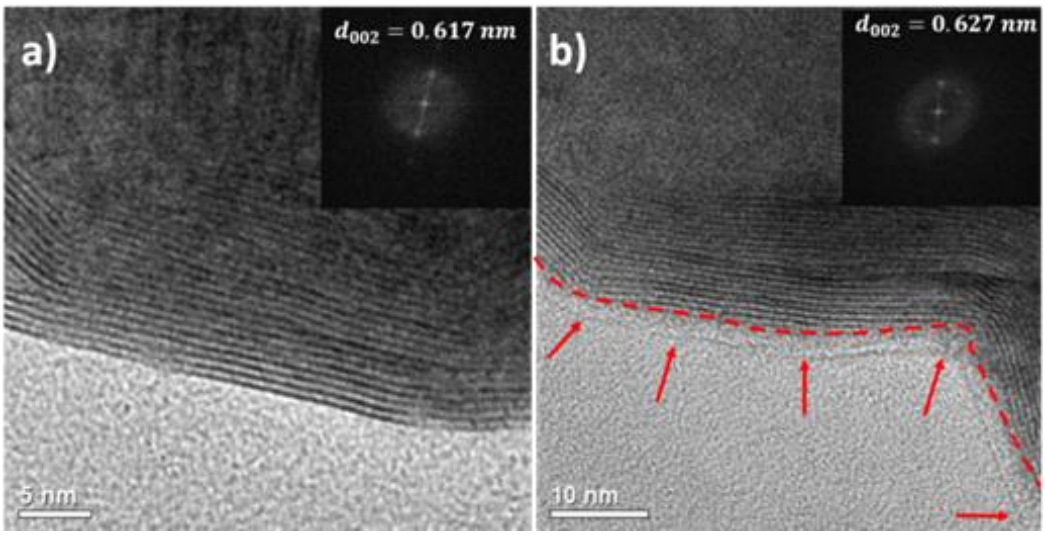

Figure 4-2 (a) HRTEM image of pristine WS_2 (inset is FFT image of the whole region); (b) TEM image of H-WS_2 (inset is FFT image).

Figure 4-3 shows the XRD patterns of the pristine and H-WS_2, respectively. The background has already been subtracted. Two different phases of WS_2 have been observed in the pristine nanoparticles: tungstenite-2H (PDF 84-1398), tungstenite-3R (PDF 84-1399). In addition, there was also little amount of contamination detected: tungstite (hydrous tungsten oxide) (PDF- 84-0886) and tungsten oxide (PDF 32-1395). The XRD patterns of both 2H and 3R phases of WS_2 are still strong after the hydrogenation. However, the tungstite phase disappeared after hydrogenation, which could be reduced into the tungsten oxide, because the tungstate could be easily transformed into tungsten oxide at a high temperature annealing.

The Rietveld refinement is one of the most successful quantitative analysis methods to model the diffraction pattern by duplicating the calculated pattern to the experiment one. TOPAS will be used for the quantitative analysis in this dissertation. And the goodness of the fit could be identified by the value of Rwp, and when Rwp < 10, the refinement can be accepted as good result. Figure 4-4 shows the results of Rietveld refinement, the blue curve is the observed value, the red curve is the calculated value and the gray curve is the difference between the observed

value and calculated value. The Rwp-value for pristine nanoparticles is 11.034, for hydrogenated nanoparticles it is 11.136. Both values show a convinced fitting result. Table 4-1 shows the phase wt % of the two samples according to the results of Rietveld refinement. We could find that 3R (R denotes rhombohedral) phase wt % increased after hydrogenation whereas the 2H (H denotes hexagonal) phase decreased. Also, almost all the tungstite transferred to the triclinic tungsten oxide. Different stacking sequences of trigonal prismatic layer result in different symmetries. In our case, the phase transition induced by hydrogenation could results in disorders in the mixture phase, which indicates an evolution in electrochemical performance. On the other hand, the phase transition from the tungstite to tungsten oxide, which we thought comes from the high temperature during the plasma treatment process, but it is just 3 % changing and could have little contributions to enhanced electrochemical performance.

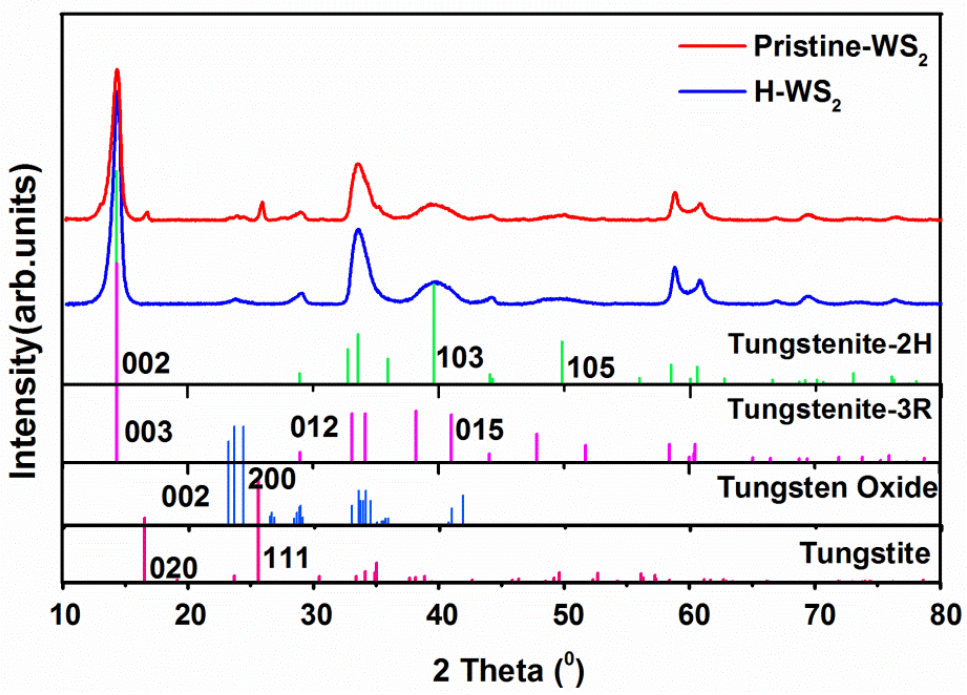

Figure 4-3 XRD patterns of pristine and H-WS_2 nanoparticles.

Table 4-1 Phase wt % of pristine and H-WS_2 nanoparticles.

Phases	Tungstenite 2H	Tungstenite 3R	Tungstite	Triclinic WO_3
Pristine WS_2	56.17%	34.70%	3.42%	5.71%
H-WS_2	50.81%	40.01%	0%	9.17%

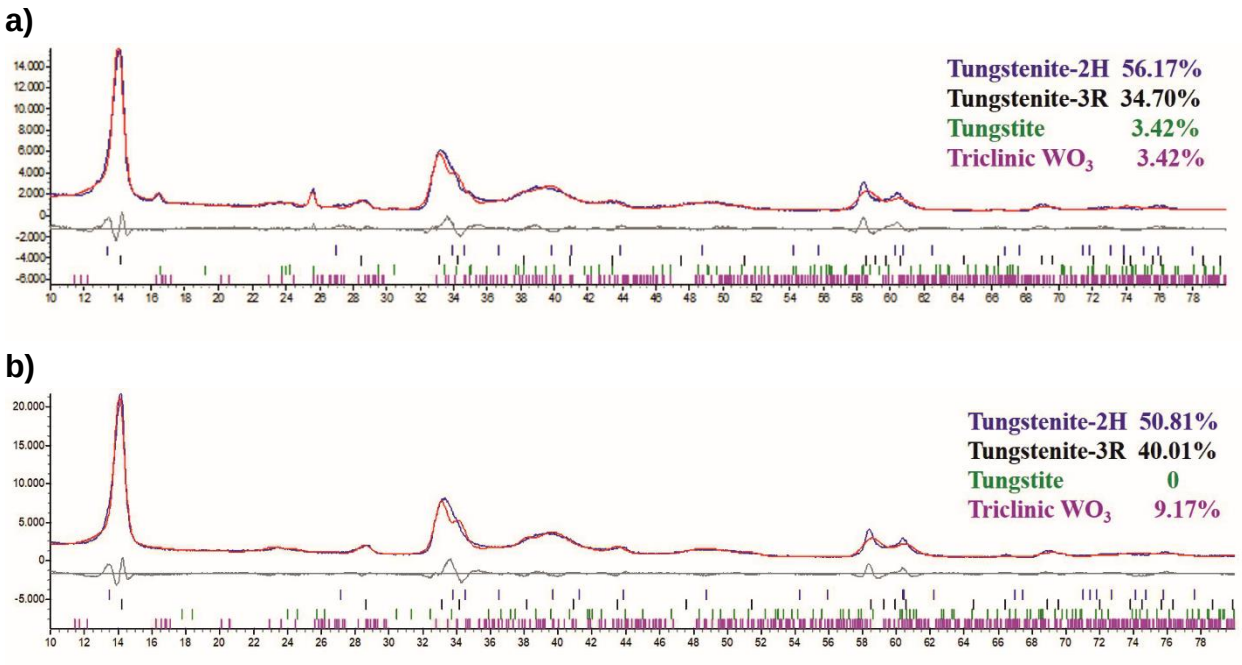

Figure 4-4 Full pattern quantitative analysis in TOPAS. (a) Pristine WS_2 nanoparticles; (b) H-WS_2 nanoparticles.

Raman spectra of the pristine and H-WS_2 nanoparticles are shown in Figure 4-5. Both of samples were excited by 780 nm line in area ambient environment. It is obvious that WS_2 consisted of the well-known in-plane E_{2g} and out-of-plane A1g mode at 350 and 414 cm^{-1} [139], respectively. Typically, the frequency of E_{2g} decreases while that of A1g peak increases with increasing layer number in TMD materials [140]. The blue-shift of the A1g peak results from the atom vibration which was suppressed by the interlayer Van der Waals force due to higher force constant [141]. On the contrary, E_{2g} peak shows a red-shift with increasing layer. Lee. C. [142] have argued that stacking induced structure changes or long-range Coulombic interlayer interactions are the main reasons for the peak shift rather than the increased interlayer Van der Waals force. In our case, a slightly phase change from 2H to 3R doesn't cause obvious frequency change of the vibrated atoms. Thus, no peak-shift was witnessed after hydrogenation. However, the peak intensities of both modes decrease after hydrogenation, and both vibration modes show broad peaks after hydrogenation. Hence, it could be speculated that hydrogenation has caused different scattering properties which were probably induced by the slightly phase transition and surface disorder due to the rearrangement of the atoms [143,144]. In addition, tungstite was found at 1347, 1409 and 1538 cm^{-1} in both cases. As discussed above, the Raman intensity could be influenced by the molecule concentration. Therefore, this result corresponds

well with the result in XRD analysis that most water molecules in hydrous tungsten oxide disappeared after hydrogenation. N_2 adsorption/desorption isotherms were used to investigated the surface areas and pore structures of WS_2 samples. The Brunauer-Emmett-Teller (BET) specific surface areas of pristine and hydrogenated WS_2 were 6.7518 and 5.6153 $m^2 \cdot g^{-1}$, respectively (Figure 4-6 (a)(b)). We could see that both of the materials give very low surface areas.

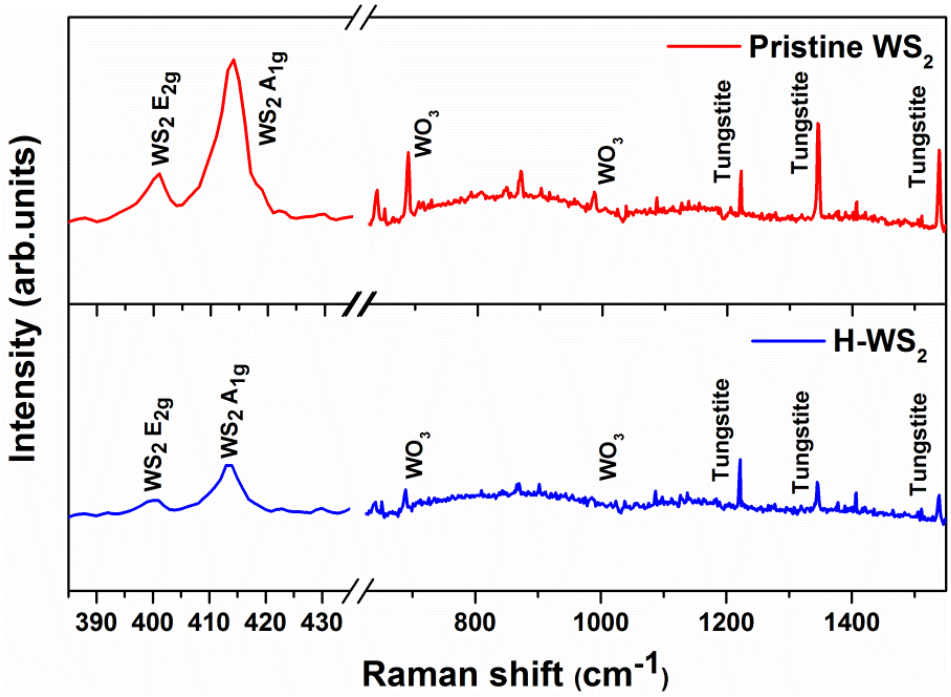

Figure 4-5 Raman spectrum of pristine and H-WS_2 nanoparticles.

The X-ray photoelectron spectroscopy (XPS) of WS_2 before and after hydrogen plasma treatment was performed to examine the effect of hydrogenation on the chemical composition. Figure 4-7 shows the XPS survey spectra of the pristine and hydrogenated WS_2 nanoparticles, tungsten, sulfur, carbon and oxygen can be observed in both samples. And there are no obvious differences between these two samples, and then the high-resolution spectra of tungsten and sulfur elements were investigated for more details. Depth resolved XPS measurements of both WS_2 nanoparticles were used to compare the elemental profile of tungsten and sulfide. The normalized W 4f core level XPS spectra of pristine and H-WS_2 was shown in upper panel of Figure 4-8 (a). The W 4f core level spectrum of the pristine WS_2 nanoparticles shows three

peaks at ~32, ~34 and ~38 eV corresponding to W $4f_{7/2}$, W $4f_{5/2}$ and W $5p_{3/2}$ respectively, they demonstrated the 4+ valence state of W from WS_2 phase [145,146]. In comparison to pristine WS_2, the peaks of H-WS_2 show a small positive shift in binding energy, suggesting the different bonding environment after hydrogenation. By subtracting the normalized W 4f spectra of H-WS_2 with pristine WS_2 sample [108,147,148], we could find there are three peaks centered at 32.88, 35.07 and 38.64 eV (show in the lower panel of Figure 4-8 (a)) which were related to the peaks shifting to the higher binding energy positions after the hydrogenation process. At this moment, there is no much work about the peaks shifting to higher energy on W for XPS investigations. We found a new research [149] about the defect WS_2, the XPS results shown that the peaks shifted to a higher binding energy when annealed in a reductive atmosphere under 1000 °C. The authors claimed the reason could be some crystals surface structure disruption at the high temperature annealing but no more discussions. For our experiment results, we supposed that could be related to the formation of the disordered surface and maybe after the hydrogen plasma treatment, the formation of W-H or W-S-H bonds could change the peak position to higher energies. We thought this kind of hydrogenation process could result in the disordered surface formation and the amorphous layer makes an important role on enhancing the electrochemical performances of the materials for anode electrode of secondary batteries. On the other side, the S 2p core level spectrum of the pristine and hydrogenated WS_2 nanoparticles shows two peaks at ~161 and ~163 eV corresponding to S $2p_{3/2}$ and S $2p_{1/2}$ of S^{2-} , as is shown in Figure 4-8 (b). The binding energy of the elements is consistent with W^{4+} and S^{2-} in WS_2 [150,151], which further confirm the WS_2 phase. However, we could find two peaks that located at about 168.6 and 169.6 eV for S 2p of pristine WS_2, which could be attributed to the sulfite and sulfate [152]. After hydrogenation process, the two peaks become weaker and only one left at about 168.8 eV, it may be for the sulfite. We think this was caused by the hydrogenation process, which we have already mentioned in the XRD part, the phase transition from the tungstite to tungsten oxide may cause the difference.

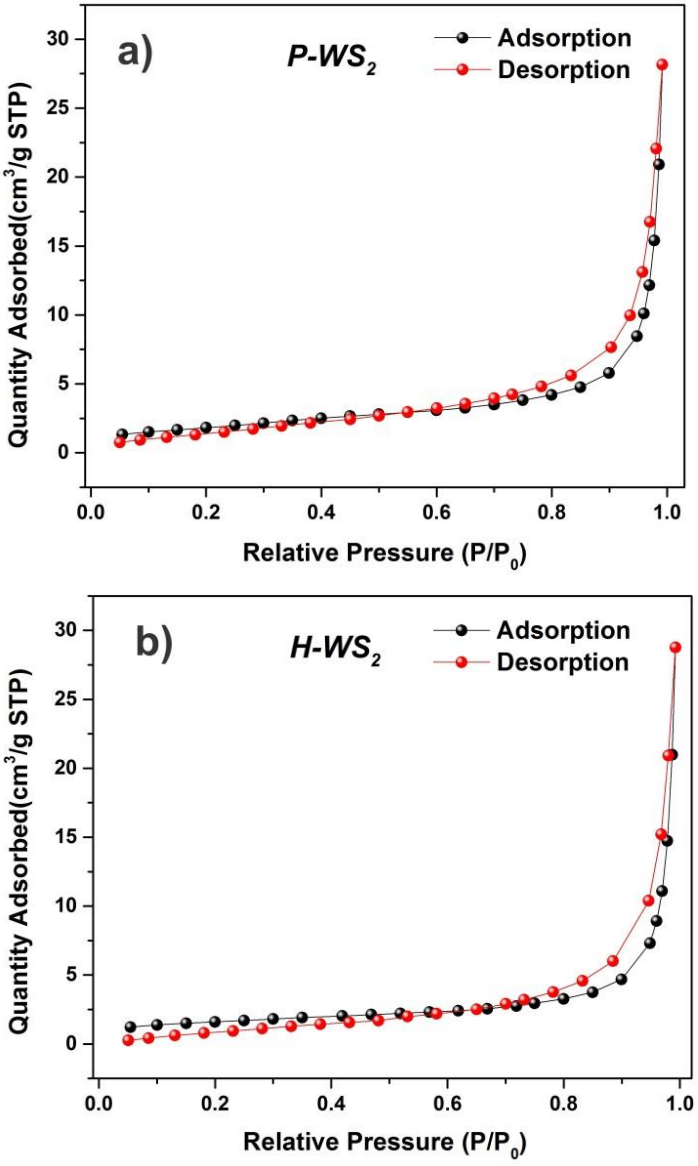

Figure 4-6 (a) N_2 adsorption/desorption isotherms of pristine WS_2; (b) N_2 adsorption/ desorption isotherms of H-WS_2.

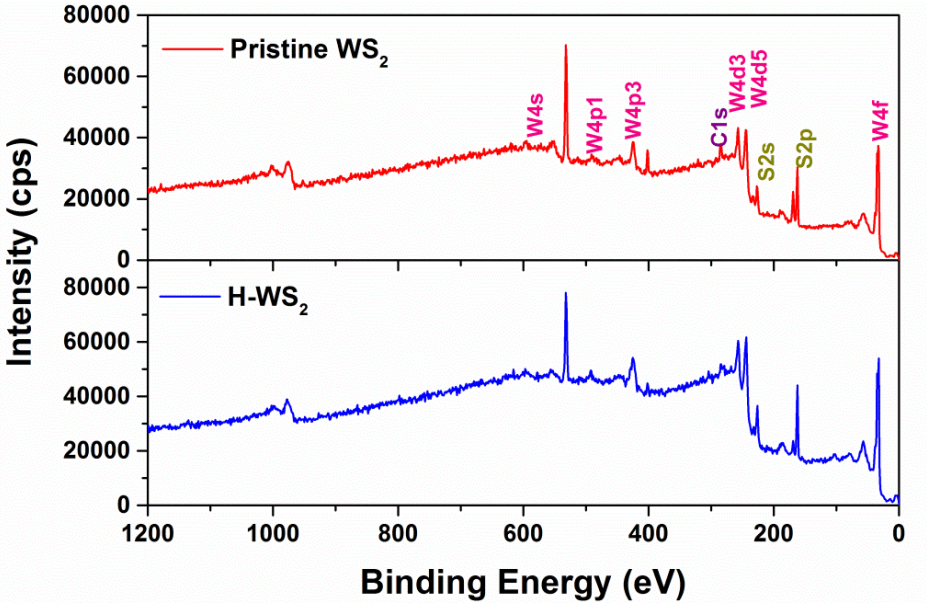

Figure 4-7 XPS survey spectra of the pristine and H-WS_2 nanoparticles.

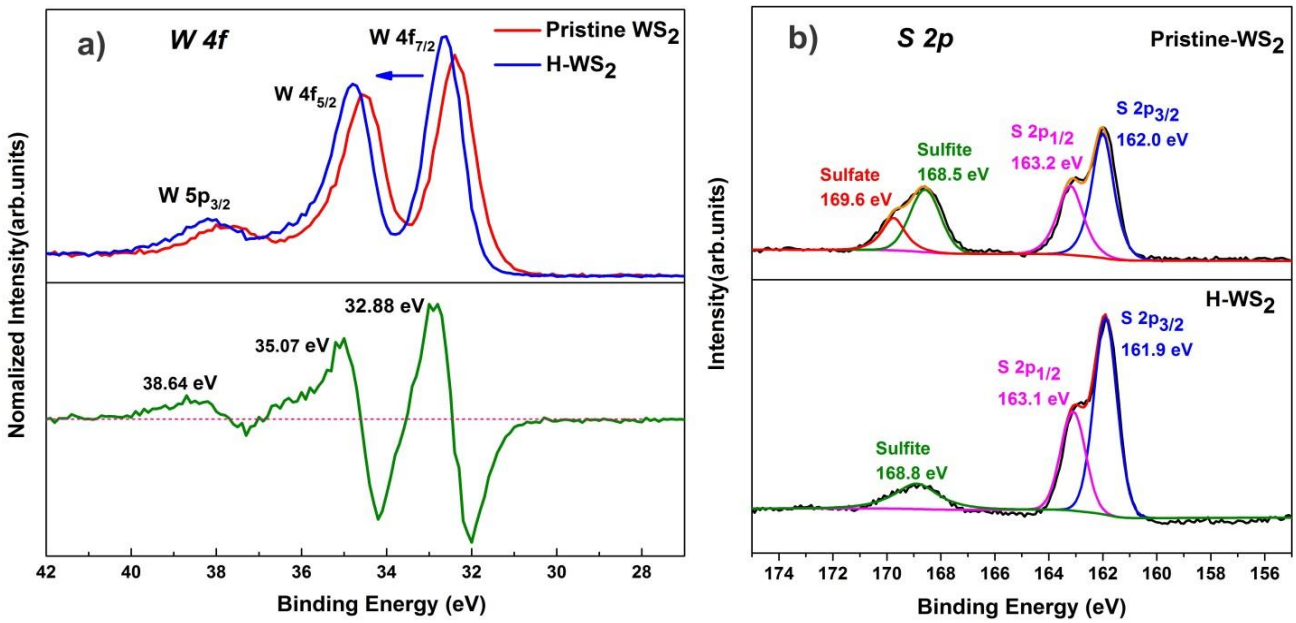

Figure 4-8 XPS spectra of (a) W 4f and W 5p and (b) S 2p for pristine and hydrogenated WS_2.

4.2.2 Electrochemical Performance of LIBs

After the characterization, we measured the electrochemical performances of the samples used as anode material for LIBs firstly. Figure 4-9 shows the cyclic voltammetry (CV) curves of pristine and hydrogenated WS_2 for the first cycle between 0.01 and 3.0 V at a scan rate of 0.5 $mV \cdot s^{-1}$. The small reduction peaks located at about ~1.03 V could be attributed to the lithium insertion into the interlayer space of WS_2 to form Li_xWS_2, as shown by Eq. (4-1):

$$WS_2 + xLi \rightarrow Li_xWS_2 \quad (4\text{-}1)$$

The following wide plateaus at about 0.5 V could be ascribed to the subsequent conversion reaction of Eq. (4-2):

$$Li_xWS_2 + (4 - x)Li^+ \rightarrow 2Li_2S + W \quad (4\text{-}2)$$

and accompanying with the irreversible decomposition of the electrolyte and formation of the gel like solid electrolyte interface (SEI) layer [129,133]. This step is the main reason for the irreversible capacity loss during the discharge process. For the first anodic scan, a small peak at ~1.25 V and a large oxidation peak located at ~ 2.5 V associated to the lithium extraction [123,129,153]. We could see the hydrogenated WS_2 shows larger current peaks than the pristine samples during the processes. Figure 4-10 (a) indicates the CV curves from the 1st to 5th cycles of H-WS_2, from the second cycle, there are two new reduction peaks appeared at ~ 1.77 and 2.03 V, these could be explained by the formation of a gel-like polymeric layer by of the dissolution of Li_2S in the electrolyte [152,153]. The CV curves from the 2nd to 5th cycles are perfectly overlapped, indicating an excellent reversibility of the hydrogenated sample. While the pristine materials shown smaller peaks and irreversible results from the 2nd cycle for the CV curves (Figure 4-10 (b)).

Figure 4-11 (a) shows the first discharge/charge profiles of the H-WS_2 at a current density of 0.1 $A \cdot g^{-1}$. The results could be greatly matched with the CV performance. There are three phases during the discharge process, a rapid voltage decreases during the first period from open circuit voltage (OCV) to 1.0 V, this is the intercalation of Li in WS_2 (Eq.1); the second phase was the decomposition of Li_xWS_2 to Li_2S and W, which we have already mentioned in Eq. (2) of the CV

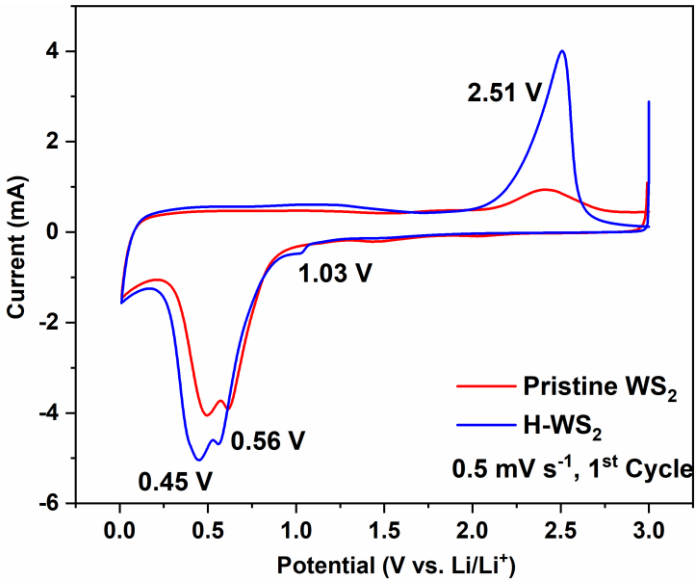

Figure 4-9 CV curves for the pristine and H-WS_2 electrodes measured at a scan rate of 0.5 $mV \cdot s^{-1}$.

part. This process is the main reaction between the lithium and WS_2, the first reason for the plateau is the subsequent conversion reaction of lithium with WS_2, and another could be the formation of a solid electrolyte interlayer (SEI). And the phase III as a steep voltage drop [129]. When charged to 3.0 V, the reaction process could be described by Eq. (4-3) as following:

$$W + 2Li_2S \leftrightarrow W + 2S + 4Li \quad (4\text{-}3)$$

This means that the Li_2S will be converted to S and the mental W remains inert. During the next subsequent cycles, the reversible reaction occurs between S and Li_2S [128]. Depending on the above results, we know that the first discharging process of WS_2 is different from the next cycles, the formation of Li_xWS_2 between OCV and around 1V (Eq. 1) followed by the decomposition of Li_xWS_2 to Li_2S and W (Eq. 2) just happen for the first cycle, then the reaction of Eq. (3) will be the reversible reactions during the next cycles. From the CV results and the initial discharging/ charging curves of H-WS_2 and pristine WS_2, we find that the H-WS_2 shows a much more obvious peak for CV and plateaus for the charging curves, it means there are much more Li_2S and S reacted for the Eq. (3), leading to better performances during the following cycles. The main reason for the improvements could be attributed to the disordered surface. The first two steps become much easier for hydrogenated WS_2 than pristine material because of the disordered surface, which could improve the electrical conductivity of H-WS_2 electrodes, as a resulting of the larger capacity retention and longer lifetime of the electrode could be obtained.

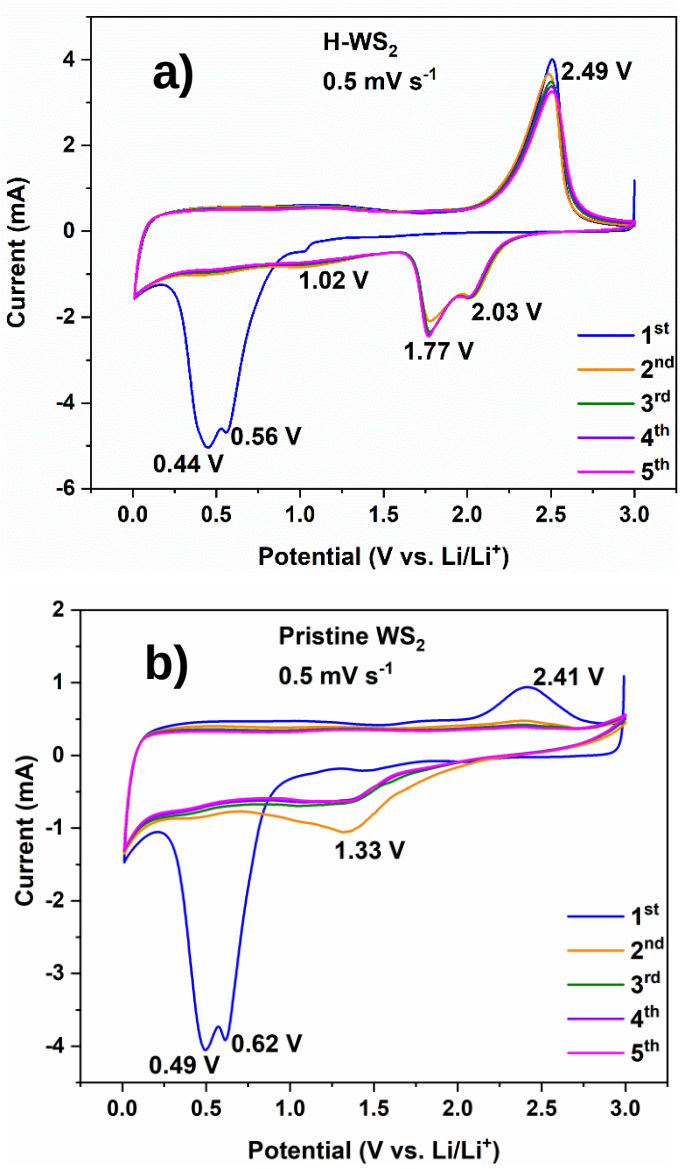

Figure 4-10 CV curves for the (a) H-WS_2 and (b) pristine WS_2 electrodes measured at a scan rate of 0.5 mV·s^{-1} at different cycles of lithium ion batteries.

Figure 4-11 (b) is the galvanostatic performance of the two samples at different current densities of 0.1, 0.5, 1.0, 2.0 and 4.0 A·g^{-1}. The first discharge/charge specific capacities of the H-WS_2 at 0.1 A·g^{-1} are 674.6/556.2 mAh·g^{-1}, with a columbic efficiency (CE) of 82.2 %. While the discharge/charge capacities of pristine WS_2 sample is 711.9/442.9 mAh·g^{-1} and with a lower columbic efficiency of 62.2 %. When the current densities are 0.1, 0.5, 1.0, 2.0 and 4.0 A·g^{-1}, the discharge capacities of H-WS_2 are about 568.4, 463.5, 346.9, 189.6 and 82.9 mAh·g^{-1}, respectively. For the pristine WS_2 sample, the discharge capacities are 364.3, 154.7, 106.2, 65.3 and 28.9 mAh·g^{-1}, respectively, they are much lower than the sample with H_2 plasma treatment. Figure 4-12 (a) (b) shows the galvanostatic discharge/charge profiles of the WS_2

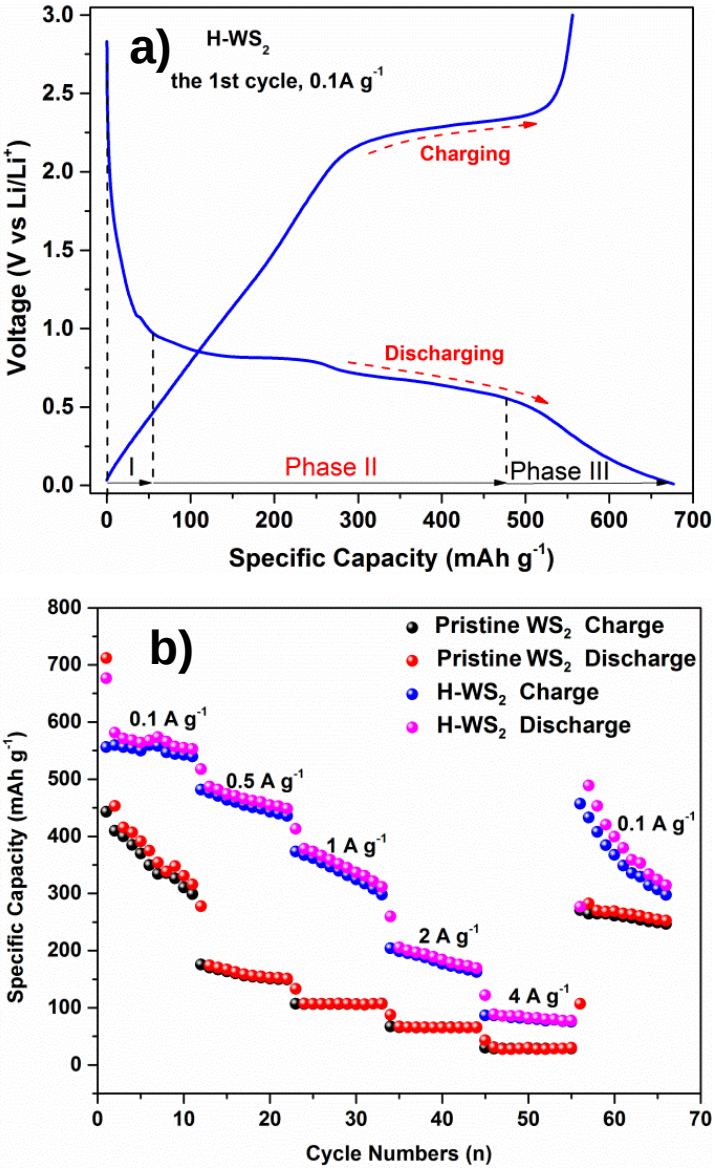

Figure 4-11 (a) Initial discharge/charge curves of H-WS_2 at 0.1 A g^{-1} for the 1st cycle in the potential window of 0.01-3.0 V; (b) Rate performances of samples at different charging/ discharging rates.

samples at different current densities. For the pristine WS_2 sample, we could find that the discharge and charge plateaus are appeared at a low current density (0.1 A·g^{-1}), with the increasing of the current densities, there is almost no obvious charge or discharge plateaus. In contrast, the plateaus are more prominent for the H-WS_2 anode at different current densities. It means the H_2 plasma treatment has a good influence for improving the electrochemical performance of the WS_2 when used as the anode materials for LIBs.

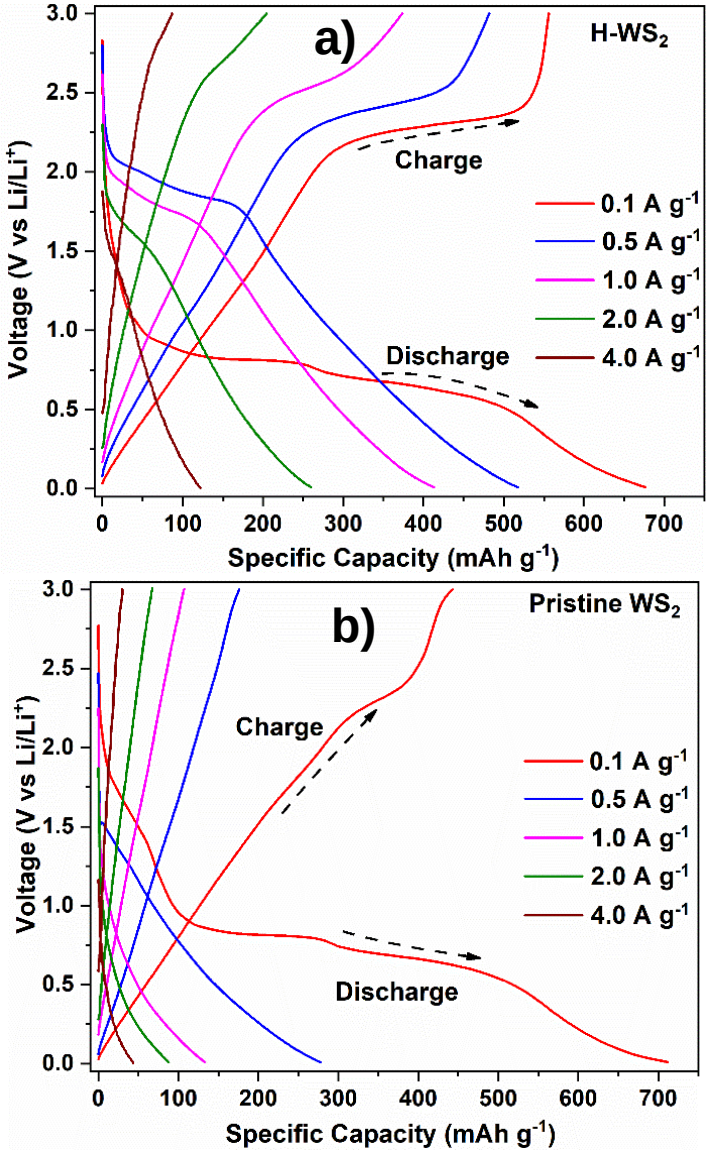

Figure 4-12 (a) Initial discharge/charge curves of H-WS_2 at different rate in the potential window of 0.01–3.0 V; (b) Initial discharge/charge curves of pristine WS_2 at different rate in the potential window of 0.01–3.0 V of lithium ion batteries.

Figure 4-13 is the long-term cycling performance of these two materials at a high current density of 2 $A \cdot g^{-1}$ for 60 cycles. The first discharge/charge capacities of H-WS_2 are 595.8/500.9 $mAh \cdot g^{-1}$ with a coulombic efficiency of 84.0 %, while the capacities of pristine WS_2 sample are 614.1/ 384.2 $mAh \cdot g^{-1}$ with a first cycle coulombic efficiency of 62.56 %. After 60 cycles process, the discharge specific capacity of H-WS_2 is about 180 $mAh \cdot g^{-1}$, just a little higher than the pristine WS_2 sample (140 $mAh \cdot g^{-1}$). It means the stabilities of WS_2 after treatment just improved a little. The next two figures (Figure 4-14 (a) (b)) are the discharge and charge profiles of the long-term performance from the 1^{st} to 50^{th} cycles. It is worth mentioning that there are obvious plateaus for the discharge/charge curves of H-WS_2, while the pristine sample

shows a very fast capacity fading just after several cycles. The irreversible reaction during the discharge/charge process was depressed in the H-WS_2 sample, which could be easily found from the initial curves from Figure 4-12 & 4-13. These results are quietly well matched with the CV and rate performances which we discussed before.

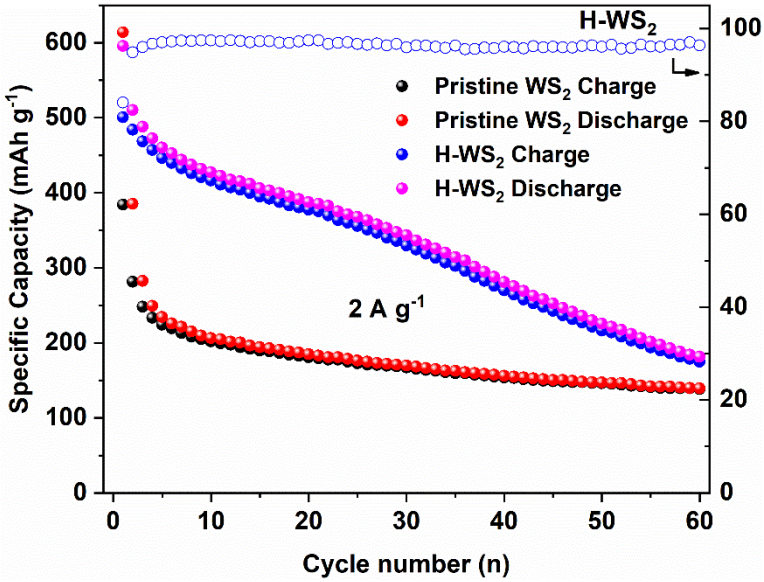

Figure 4-13 Long term performances and the coulombic efficiencies of samples at charging/discharging rate of 2.0 $A \cdot g^{-1}$ for 60 cycles.

In order to investigate the resistance changing after H_2 plasma treatment, electrochemical impedance spectroscopy (EIS) was carried out for the two electrodes in the frequency range of 100 kHz to 0.01 Hz after discharge/charge for 5 cycles at a current density of 1 $A \cdot g^{-1}$. As we all know, the EIS plots of the electrode of a LIB are composed of one or two semi-circles in the high frequency region followed by a straight line with decreasing frequency. The depressed semicircle from high to medium frequency could be attributed to the charge transfer process and the formation of the SEI layer [154]. Rs represents the internal resistance of the capacitor. And the first semicircle in the high frequency range which is an ion migration resistance that related to the diffusion resistance of ions in the SEI layer. The fitted impedance (R_{SEI}, fitted by Zview) of the pristine WS_2 and H-WS_2 were 132.4 and 3.817 Ω, respectively (Figure 4-15). And the second semicircle in the middle frequency is charge-transfer resistance (R_C, fitted by Zview). The fitted impedance of H_2 plasma treated WS_2 (7.2 Ω) was also lower than that of the pristine WS_2 (313.5 Ω). And the sloping line in the lower frequency, which is called Warburg impedance (W_S). W_S is related to the diffusion of the lithium ions in the $LiPF_6$ particles. And CPE1 and CPE2 expressed the constants. The fitted impedance parameters are listed in Table

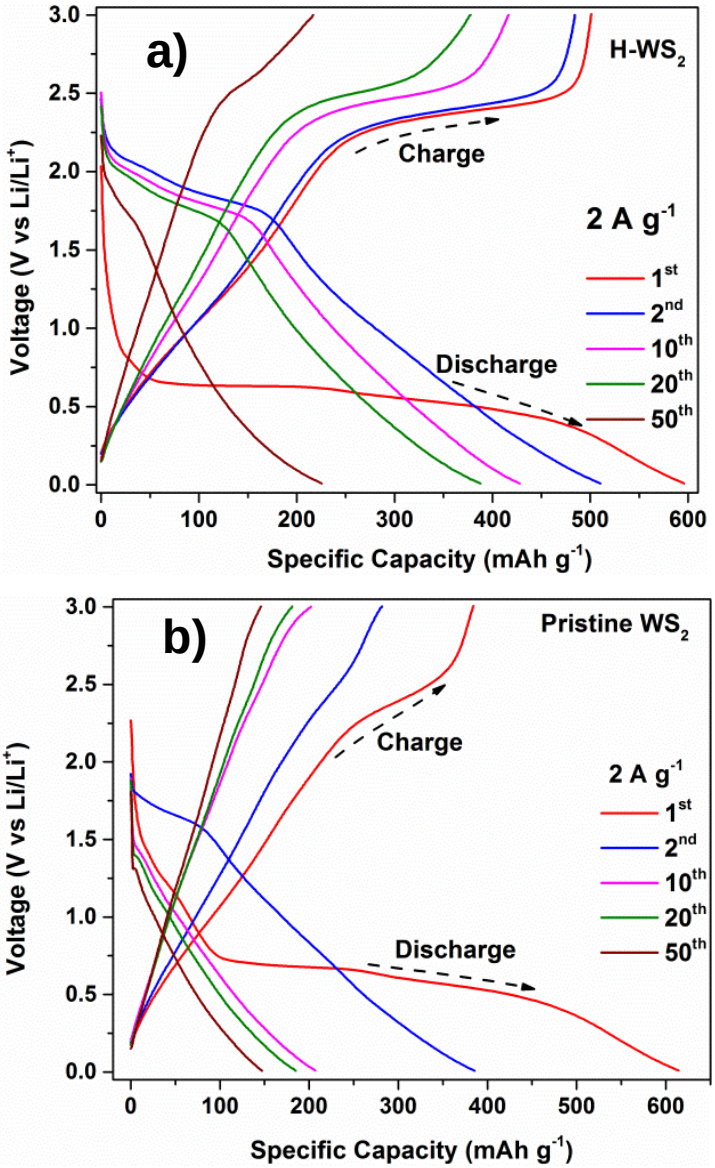

Figure 4-14 (a) Initial discharge/charge curves of H-WS_2 at 2.0 $A \cdot g^{-1}$ for different cycles in the potential window of 0.01-3.0 V; (b) Initial discharge/charge curves of pristine WS_2 at 2.0 $A \cdot g^{-1}$ for different cycles in the potential window of 0.01–3.0 V of lithium ion batteries.

4-2. The lower impedance of the ion diffusion in SEI layer and charge-transfer implied that the electrode is more favorable for the ion transport during the discharge/charge process [129]. The H-WS_2 nanoparticles with a disordered surface have a strongly improved conductivity. What's more, we think that the resistance of the SEI layer and the transfer resistance of H-WS_2 are benefit from the disordered surface, the ion transportation within the electrode become much

easier and faster than the pristine material, and this is confirmed by the EIS measurements with clearly reduced charge transfer resistance. The semicircle size of the H-WS_2 is much smaller than that of pristine WS_2, implying that the disordered surface after hydrogenation can greatly enhance the charge transfer during the electrochemical reactions and leading to an improvement of the rate and cycling performance.

Table 4-2 Fitted impedance parameters for the electrodes of LIBs.

Electrode	R_S (Ω)	R_{SEI} (Ω)	R_C (Ω)
Pristine WS_2	2.93	132.4	313.5
H-WS_2	3.47	3.817	7.173

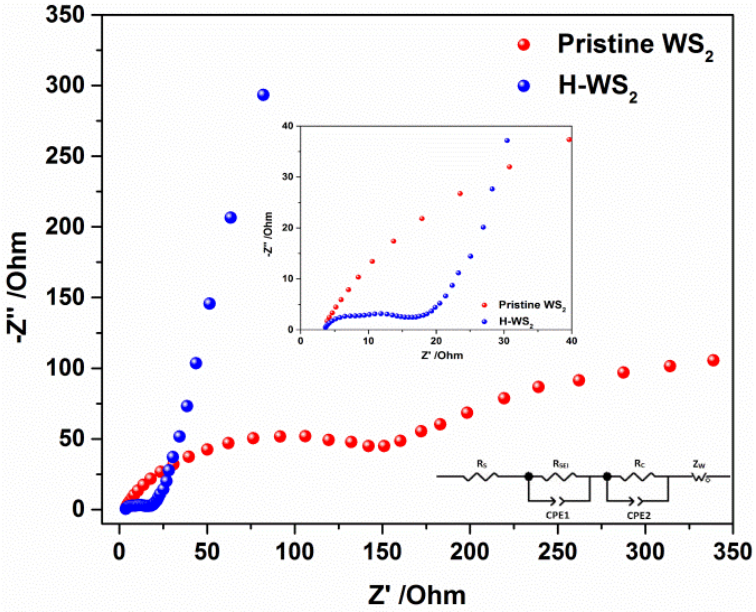

Figure 4-15 Nyquist plots for pristine WS_2 and H-WS_2 for lithium ion batteries.

4.2.3 Electrochemical performance of SIBs

The pristine and H-WS_2 were also tested as the anode electrodes of sodium ion batteries (SIBs). Figure 4-16 shows the first cyclic voltammetry of the pristine and H-WS_2 for SIBs at the scan rate of 0.1 $mV \cdot s^{-1}$. From the first cathode scan of the H-WS_2, there are three peaks located at 0.9, 0.6 and 0.2 V, which could be attributed to the insertion of sodium ions into WS_2 lattice to

form Na_xWS_2, conversion reaction of WS_2 with sodium ions and the formation of SEI layer on the surface of the electrode. And it corresponds to the chemical reaction in Eq. (4-4) [155–157],

$$WS_2 + 4Na^+ + 4e^- \rightarrow 2Na_2S + W \quad (4\text{-}4)$$

and then for the anode scan, three peaks located at 1.9, 2.3 and 2.6 V could be viewed, which could be attributed to the sodium extraction from Na_xWS_2, as shown in Eq. (4-5) [49,122,155–157].

$$Na_xWS_2 \rightarrow xNa^+ WS_2 + xe^- \quad (4\text{-}5)$$

The peak positions of pristine WS_2 are almost the same as H-WS_2, but more significant peaks were obtained for hydrogenated material, indicating that better sodium storage ability was gained after H_2 plasma treatment. In the following CV curves of H-WS_2 (Figure 4-17), the reactions peaks become broad and less prominent.

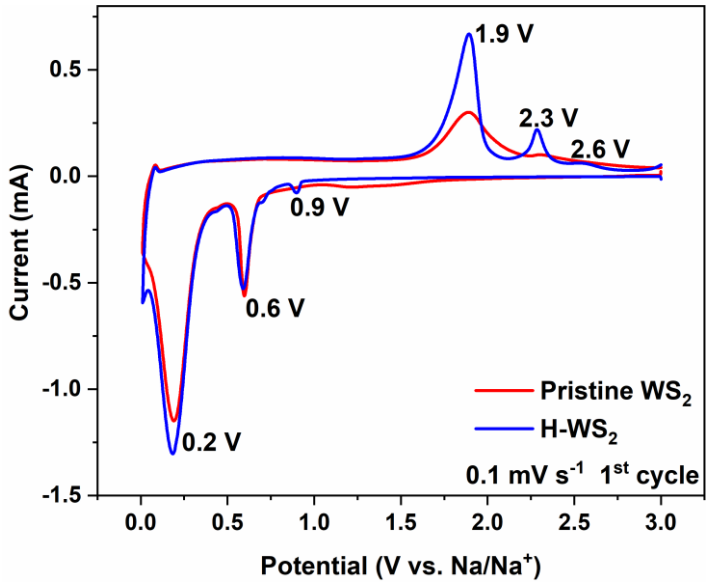

Figure 4-16 CVs for the pristine and H-WS_2 electrodes measured at a scan rate of 0.5 mV s^{-1} of sodium ion batteries.

Figure 4-18 (a) shows the first discharge/charge curves of two samples at a current density of 0.1 A·g^{-1}. It's almost the same as the LIBs, the hydrogenated samples showed a higher sodium storage ability than the pristine WS_2. For the first sodiation and de-sodiation process, the specific capacities of H-WS_2 were 515.6 and 404.5 mAh·g^{-1}, leading to an initial columbic efficiency of 78.45 %. While, the pristine WS_2 had a discharge/charge capacities of 561.2/344.7

$mAh \cdot g^{-1}$ for the first cycle that to be with a lower CE of 61.42 %. As we mentioned in the LIBs performance part, the irreversible capacity may due to the irreversible reaction and the formation of the SEI layer. The rate capacities of the two samples are showed in Figure 4-18 (b). For H-WS_2, reversible specific capacities of 375.1, 325.7, 236.1, 138.9 and 63.2 $mAh \cdot g^{-1}$ are achieved at current densities of 0.1, 0.2, 0.5, 1, 2 and 4 $A \cdot g^{-1}$, respectively. The capacity was returned to about 143.5 $mAh \cdot g^{-1}$ and decreased to be similar with the pristine sample when the current density came back to 0.1 $A \cdot g^{-1}$. Compared with the hydrogenated material, the pristine sample showed a very quick fading of the specific capacities, especially when it came to the high current densities.

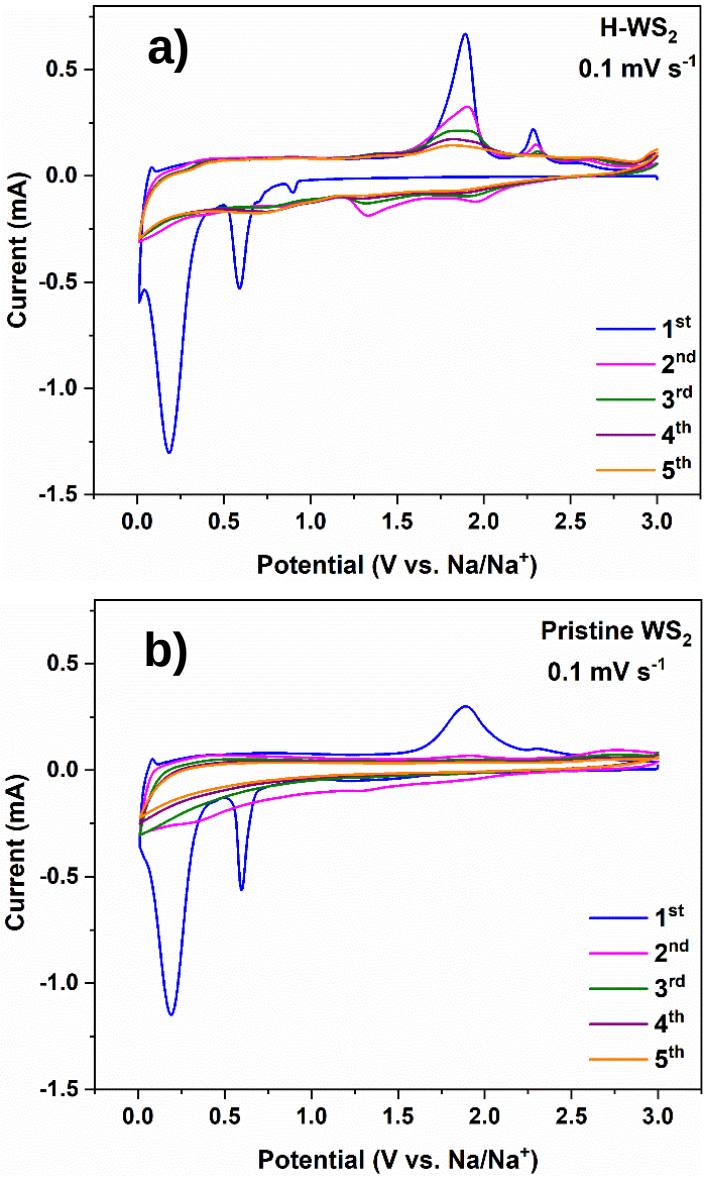

Figure 4-17 (a) H-WS_2 and (b) pristine WS_2 electrodes measured at a scan rate of 0.1 $mV \cdot s^{-1}$ for different cycles of sodium ion batteries.

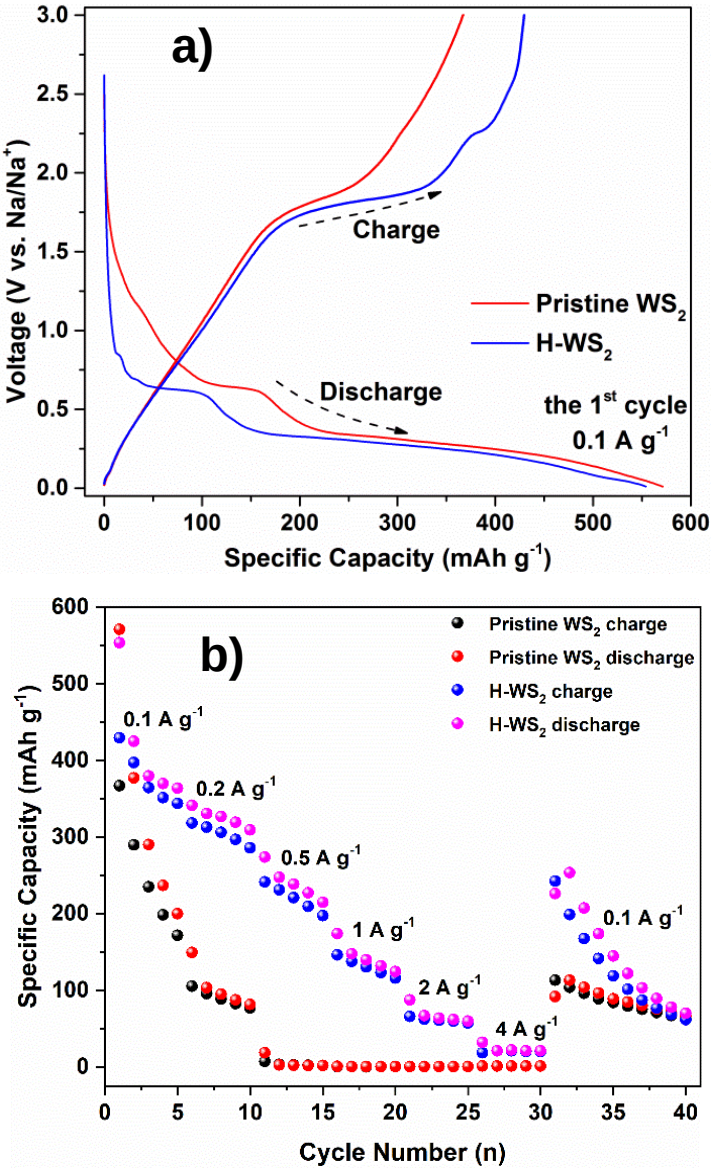

Figure 4-18 (a) Initial discharge/charge curves of H-WS_2 at 0.1 A g^{-1} for the first cycle in the potential window of 0.01-3.0 V; (b) Rate performances of samples at different discharge/charge rates.

Furthermore, the long cycling performances of these two samples were showed in Figure 4-19. For the first 25 cycles, the hydrogenated sample showed a higher specific capacity than the pristine sample. After that, the stabilities of both samples are not so good. Because the sodium ions have a much larger size than lithium, the volume change during the sodiation and de-sodiation process won't be well accommodated compared with the lithiation and de-lithiation process. Figure 4-20 shown the charge and discharge profiles of the long-term performance from the 1st to 50th cycles. We could find that there are plateaus for the H-WS_2 samples, while the pristine sample shows a very fast capacity fading just after several discharge/charge cycles.

We could say the hydrogenation process make some good effects on the performance for batteries. Subsequently, electrochemical impedance spectroscopy (EIS) measurements were performed on the WS_2 nanoparticles for SIBs. The fitted impedance (R_{SEI}, fitted by Zview) of the pristine WS_2 and H-WS_2 are 433.0 and 117.6 Ω, respectively (Figure 4-21). And the charge-transfer resistance (R_C, fitted by Zview) is reduced from ~1177 Ω for the pristine WS_2 to ~260.5 Ω for hydrogenated WS_2. The same situation is achieved for the sodium ion batteries, so now we could make sure that the simple H_2 plasma treatment could reduce the resistance of the anode materials and may improve the energy storage performances.

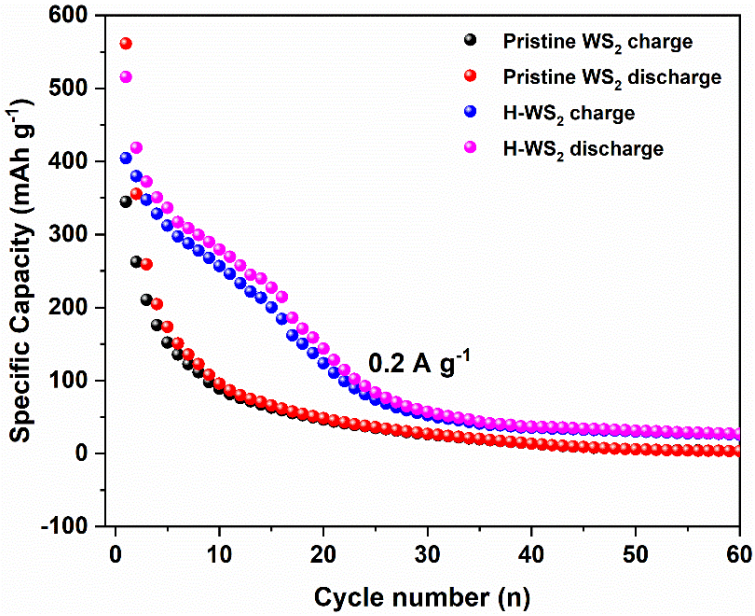

Figure 4-19 Long term performances of samples at discharge/charge rate of 0.2 $A \cdot g^{-1}$ for 60 cycles.

The cycling performances of the H-WS_2 as anode materials for LIBs and SIBs from this work are compared to those of the related WS_2 materials from literatures as shown in Table 4-3. The active materials, discharge capacities, current densities and cycling number of the electrodes are listed and compared. Firstly, most of the electrodes are carbonaceous compositions, and the carbon materials played an important role in improving the anode performance [136,156–160]. Secondly, some nanostructured or preferentially-oriented WS_2 were prepared as anode materials, the higher surface areas and pore volume, the shorter ionic diffusion length and more active sites are good at enhancing the batteries performances as well [133,150,153,155,159,161]. On the contrary, our H-WS_2 is a simply modified material without any other compositions and also no specials structures, but it still shown a great improvement

even at the high discharge current density of 2000 $mA \cdot g^{-1}$, and most of the reported WS_2 anodes are limited less than 100 $mA \cdot g^{-1}$ [133,150,158,159,161]. What's more, we measured the morphology of our electrodes after the rate performance test (shown in Figure 4-22), because of the low resolution of the figures, we couldn't tell the differences between the pristine and H-WS_2 anode, but the structures of the materials remain well as before the batteries testing.

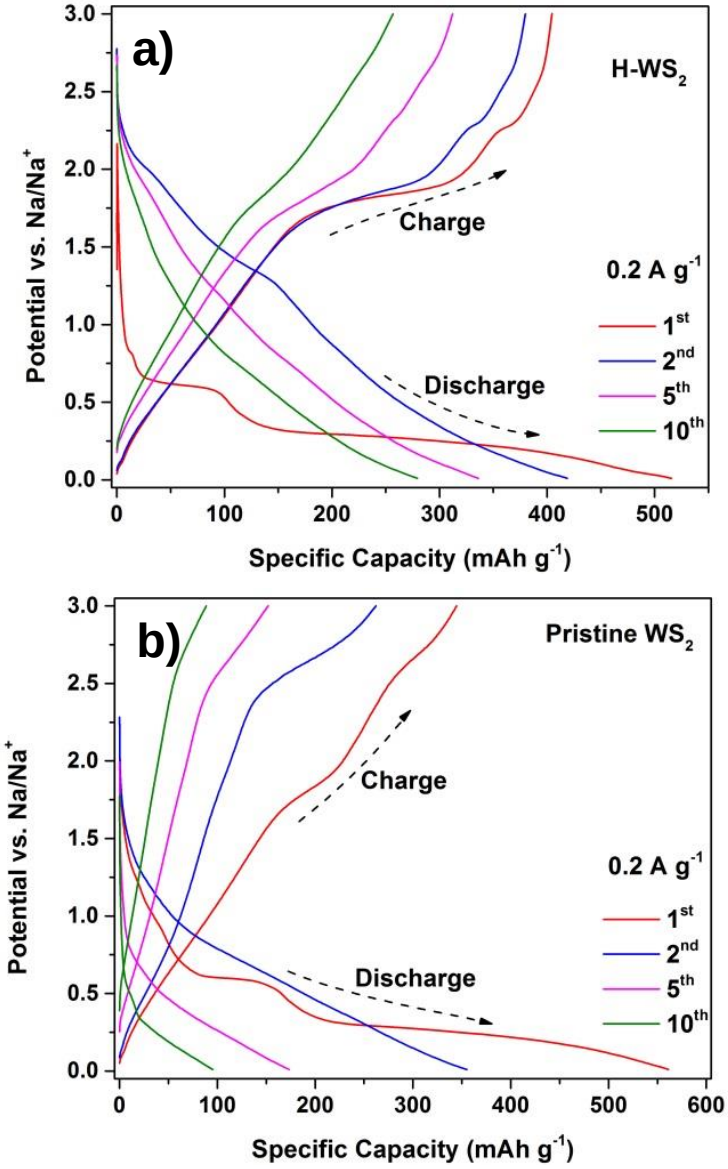

Figure 4-20 (a) Initial discharge/charge curves of H-WS_2 at 0.2 $A \cdot g^{-1}$ for different cycles in the potential window of 0.01-3.0 V; (b) Initial discharge/charge curves of pristine WS_2 at 0.2 $A \cdot g^{-1}$ for different cycles in the potential window of 0.01–3.0 V of sodium ion batteries.

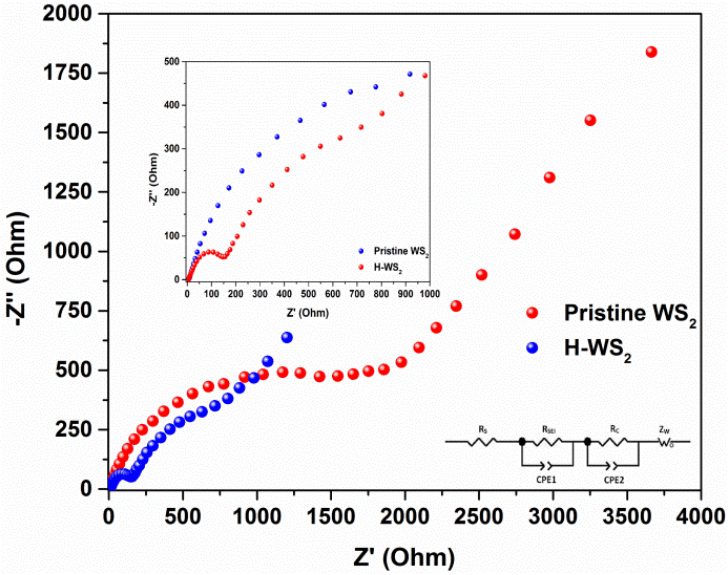

Figure 4-21 Nyquist plots for pristine WS_2 and H-WS_2 for sodium ion batteries.

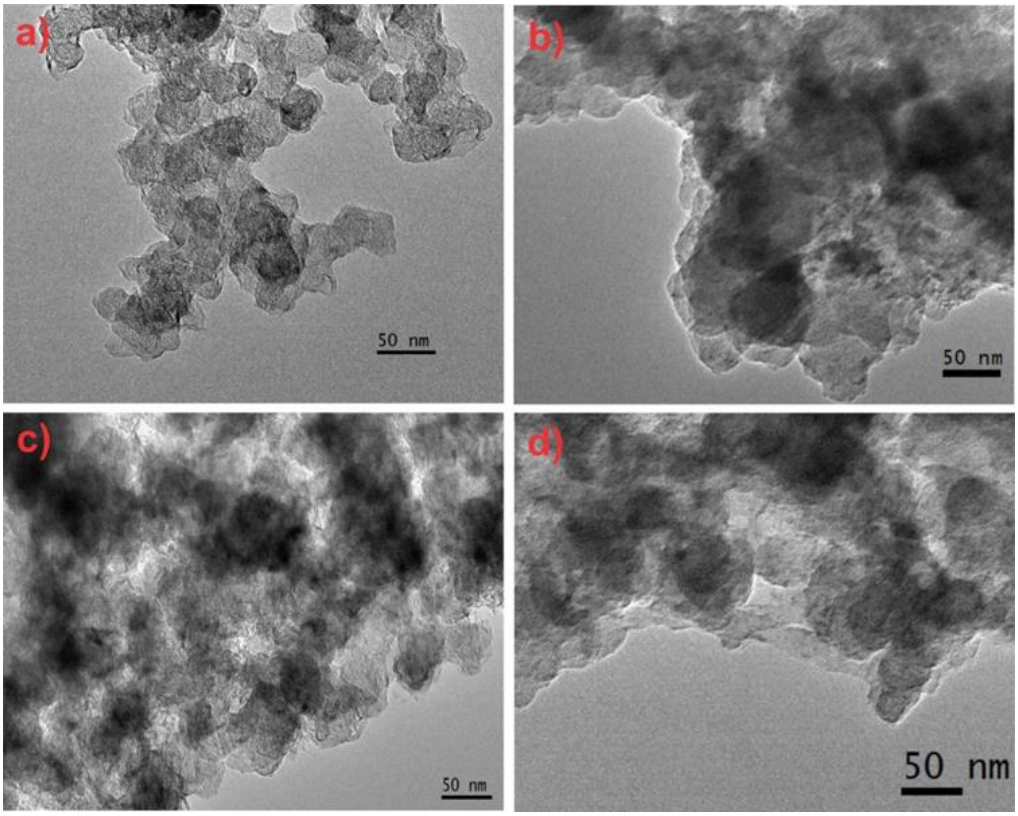

Figure 4-22 TEM images of (a) pristine WS_2, (b) H-WS_2 after rate performance testing of lithium ion batteries; TEM images of (c) pristine WS_2, (d) H-WS_2 after rate performance testing of sodium ion batteries.

Table 4-3 Comparison of WS_2 anode material for batteries between current work and related references.

Active material	Discharge capacity (mAh/g)	Current density (mA/g)	Cycle Numbers (n)	Battery type	Ref.
H-WS_2	596 / 515	2000	60	LIBs / SIBs	Current work
Sulfuration WS_2	~800	800	50	LIBs	[53]
Ordered mesoporous WS_2	~700	100	100	LIBs	[133]
Surface functionalized WS_2 sheets	465	25	50	LIBs	[150]
WS_2 nanowires	605.3	100	50	SIBs	[155]
3D porous WS_2/C	267	500	300	SIBs	[122]
WS_2-NC	450	1000	100	SIBs	[157]
WS_2 composite	519	100	100	LIBs	[158]
Few-layer WS_2	45	1000	50	LIBs	[153]
WS_2 @NGr	455/289	1000	140/60	LIBs / SIBs	[136]
Graphene-like WS_2 nanosheets	550	43.2	70	LIBs	[161]

4.3 Conclusions

In summary, WS_2 nanoparticles are modified by H_2 plasma treatment and the H-WS_2 shows a clearly improved rate performance compared with the pristine WS_2 nanoparticles when used as the anode materials for both lithium and sodium ion batteries. After the hydrogenated treatment, a disordered surface layer with a thickness of about 2.5 nm is formed. The disordered surface could be investigated by the TEM, Raman and the XPS results clearly. The H-WS_2 nanoparticles possess significantly higher specific capacity at different current densities. In addition, the electrochemical impedance spectroscopy (EIS) reveals a drastic decrease of the charge-transfer resistance for application in both LIBs and SIBs, which implies the plasma hydrogenated electrode material is more favorable for the electron transport during the lithium and sodium ion insertion/extraction process. We think after hydrogen plasma treatment, charge transfer of the electrode become easier and faster within the disordered surface than the crystalline phase. As a result, the larger capacity retention and longer lifetime of the electrode could be obtained. This is the main reason why we got a better performance for H-WS_2, and hydrogen plasma treatment could be identified as an effective method to reduce the resistance of the electrode with the disordered surface layer formation.

5. N-doped TiO_2 with Disordered Surface Layer Fabricated via Plasma Treatment as Anode with Clearly Enhanced Performance for Rechargeable Sodium Ion Battery

5.1 Introduction of nitrogen doped TiO_2 as anode materials for SIBs

Lithium ion batteries (LIBs) and sodium ion batteries (SIBs) are two of the most popular secondary batteries on the social market now [162]. But LIBs are much more popular at the moment because of the high energy density and long cycling performance. While there are still some shortcomings, especially the high cost of lithium will limit its extensive application in the future. In the meantime, SIBs have attracted much attention because sodium is an abundant alkali element widely distributed in the world. However, the ion radius of Na ions are ~70 % larger than that of Li ions, so a big challenge for the development of SIBs is to find proper electrode materials with big interstitial space to accommodate sodium ions and allow reversible and rapid ion insertion/extraction [56].

TiO_2 has already been considered as one of the great energy storage materials due to its low cost, intrinsic safety, high power density and long cycle life [58,59]. And the main challenge of using TiO_2 as anode for sodium ion batteries is its inherent low electrical conductivity. In order to solve this problem, the first and most useful approach is that trying to design nanosized TiO_2, for example nanoparticles [60], nanotubes [61] and nanorods [64], as the nanosized structure could effectively shorten the ion diffusion path and enlarge the active area of the material. Yuan et al. reported an ultra-small TiO_2 nanoparticles grown on graphene which showed a superior performance for batteries [163]. The authors claimed that the excellent electrochemical performance was mainly attributed to the particle size effect and the enhanced conductivity due to the presence of graphene network. Then there are a lot of research works that introduced carbon additives to enhance the electrical conductivity of TiO_2 for SIBs [65,67–71]. Zhang et al. synthesized a novel flexible and freestanding oxygen-deficient TiO_{2-x} nanocages anchored in N-doped carbon fibers, which exhibited a high areal capacity and an outstanding stability for sodium storage[65]. Another great strategy is preparing doped TiO_2 with N, S or Nb [72–76], in which oxygen vacancies or trivalent titanium species can be formed to improve the electrical conductivity.

Li showed a sulfur doped TiO_2 nanotube arrays anode materials for SIBs, which demonstrated superior electrochemical capability and increased kinetic stability due to the structural advantage and the giant doping effect on the electronic properties[73]. Liang and coworkers reported a nitrogen doped TiO_2 nanospheres which exhibited a stable capacity of 162 $mAh \cdot g^{-1}$ at 1 $A \cdot g^{-1}$ over 1000 cycles, as well as a superior rate performance of SIBs[76]. Yu et al. reported that the introduction of nitrogen into TiO_2 could result a partial formation of Ti^{3+} associated with the oxygen vacancies, which lead to reduce sodium ion and electron transport diffusion resistance and improve the rate capacity [72].

Herein, nitrogen doped TiO_2 (N-TiO_2) nanoparticles are obtained through the N_2 plasma treatment of the pristine TiO_2 nanoparticles (commercial P25), and investigated as anode material of sodium ion batteries. Oxygen vacancies are found in the N-TiO_2 due to the doping effect. In addition, a disordered surface layer with thickness of around 2.5 nm is formed after the plasma treatment. Such disordered surface layer is not observed in the N-TiO_2 obtained from chemical synthesis from literatures [74,76,162]. Comparing with the pristine TiO_2 nanoparticles, the N-TiO_2 nanoparticles obtained via plasma treatment, present a much better rate performance with discharge capacities of about 621 $mAh \cdot g^{-1}$ at 0.1 C and 75 $mAh \cdot g^{-1}$ at 5 C, as well as an enhanced capacity retention of higher than 98 % after more than 400 cycles. The great enhancement of the rate performance can be attributed to largely reduced charge transfer resistance at the interface and the enhanced electrical conductivity due to the formed disordered surface layer and the doped nitrogen atoms as well.

5.2 Results and discussions

5.2.1 Characterizations

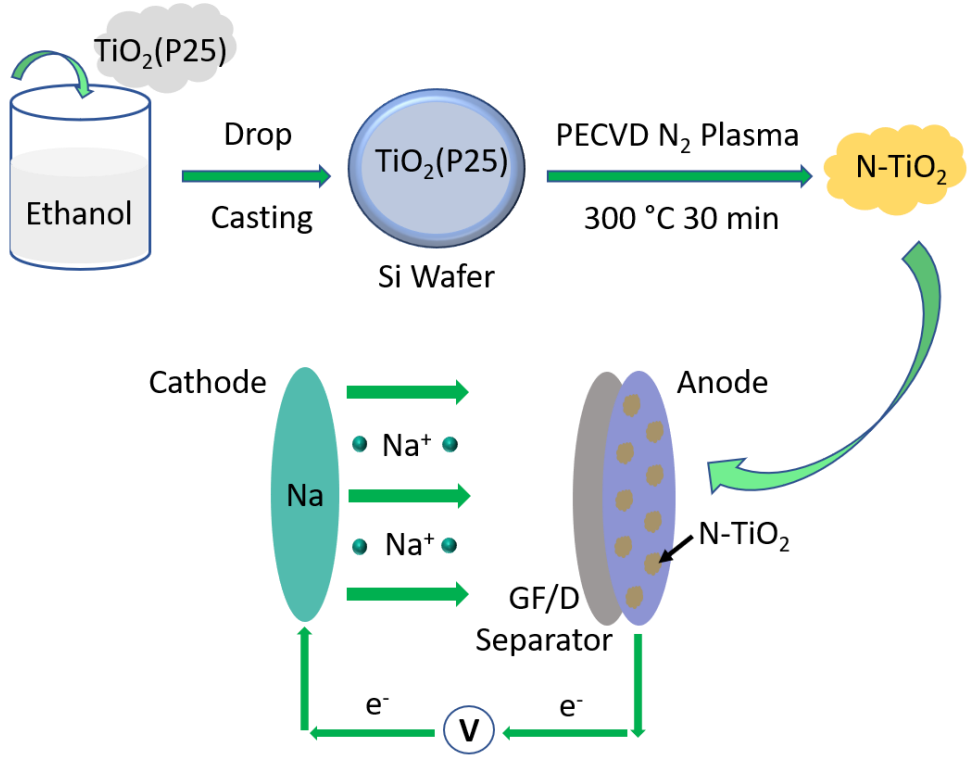

Scheme 5-1 Illustration of the sample preparation process and the basic structure of a sodium ion battery.

The sample preparation process and the basic structure of a sodium ion battery is shown in Scheme 5-1. The morphology of white pure TiO_2 and N-TiO_2 were systematically characterized by transition electronic microscope. Figure 5-1 shows the high-resolution TEM images of the two TiO_2 samples. The interplane spacing of ordered lattices is measured to be closed to 0.35 nm, corresponding to (101) planes of the anatase crystal phase (Figure 5-1 (a) & (c)). All TiO_2 nanoparticles were highly crystallized but there are some crossovers of the fringes in the N-TiO_2. They may be a partially dislocation or defects on the surface. By zooming in the region near the edges, a disordered layer which thickness is about 2.5 nm was found on the surface of N-TiO_2 as shown in Figure 5-1 (c). It's noted that after nitrogen plasma treatment, the color of TiO_2 powder has greatly changed from white (TiO_2) to light yellow (N-TiO_2) which are shown in Figure 5-2, which is caused by the nitrogen doping[164,165].

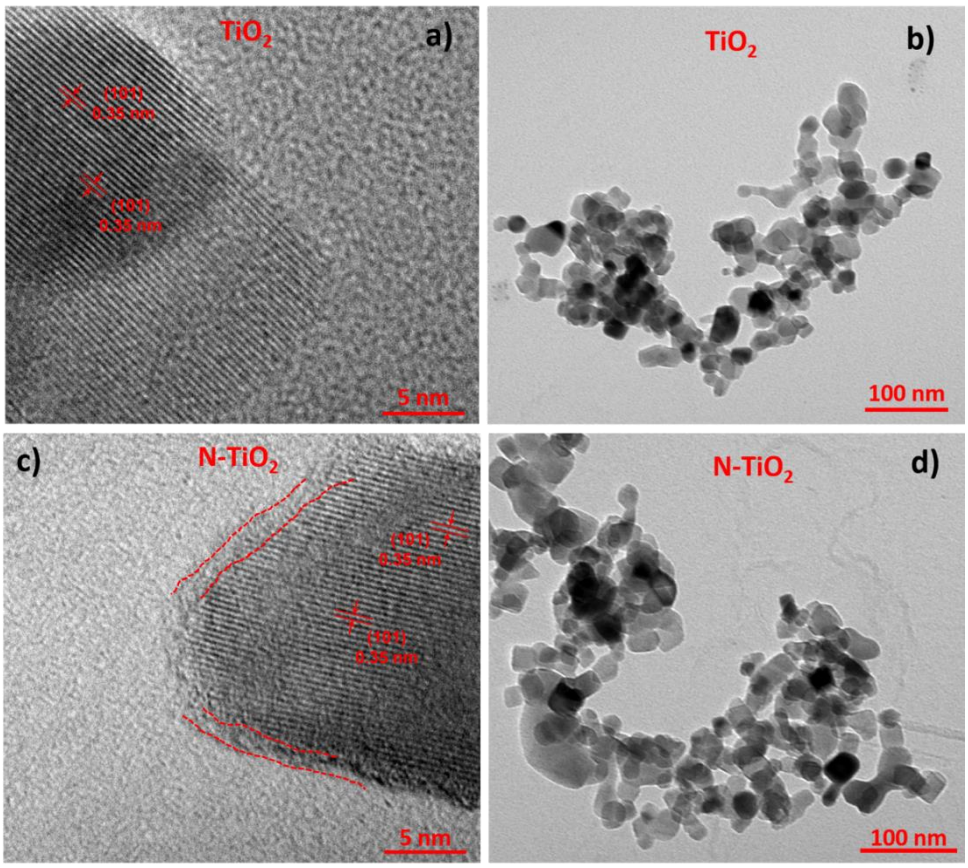

Figure 5-1 HRTEM and TEM images of pristine TiO_2 (a & b) and N-TiO_2 (c & d).

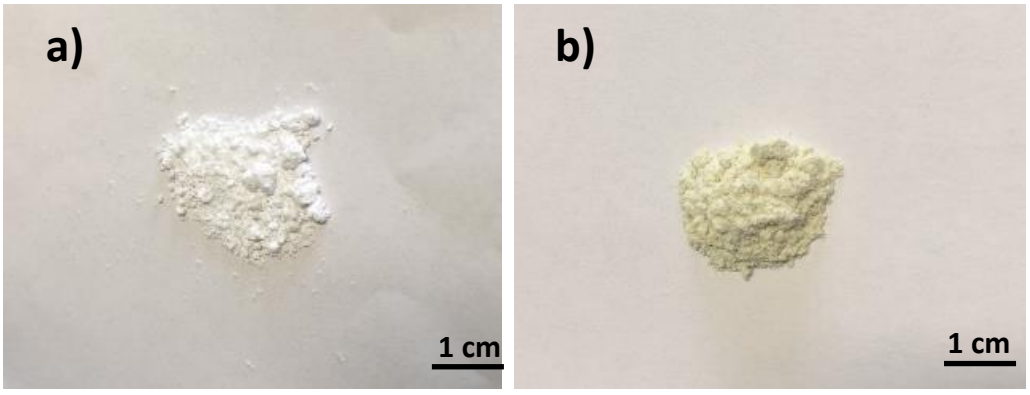

Figure 5-2 Photographs of (a)TiO_2 and (b)N-TiO_2.

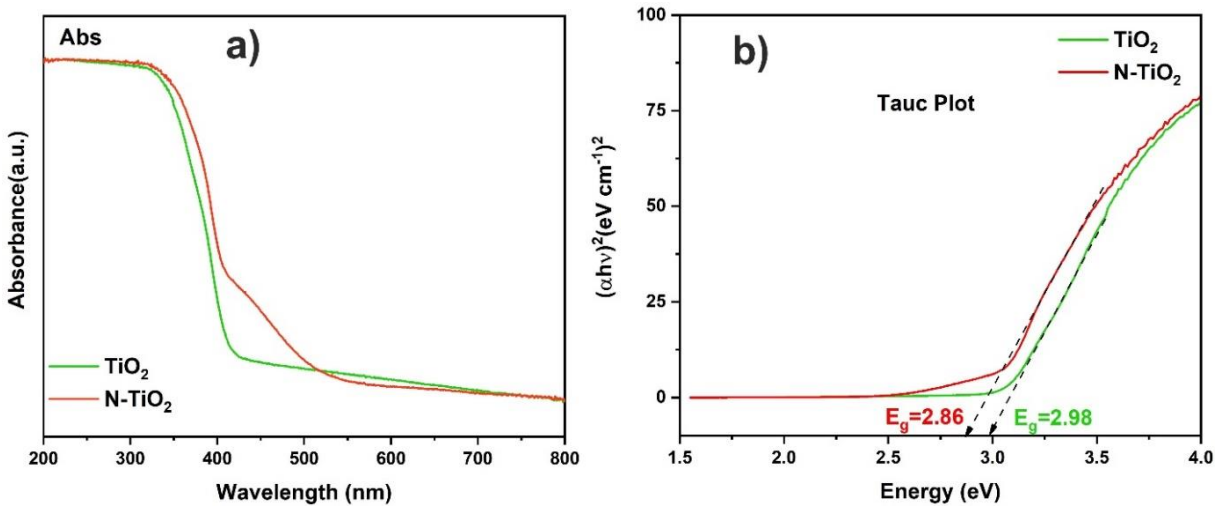

Figure 5-3 (a) UV-Vis absorption spectra of TiO_2 and N-TiO_2 and (b) Tauc plots to obtain the band gaps.

Figure 5-3(a) shows the typical absorption spectra of pristine TiO_2 and N-TiO_2 electrodes. The absorption edge of original TiO_2 appears at 410 nm, and the absorption edge of N-TiO_2 shifted to the higher wavelengths, which confirms that N is successfully doped into the TiO_2 crystal lattice[166]. Tauc plot is used to determine the band gap energies of the samples by extrapolating the linear region of the plot to intersect the photon energy axis. The calculated band gap for TiO_2 is 2.98 eV (Figure 5-3 (b)), while after the N doping, it shows a slightly decrement to 2.86 eV. This band gap decrement could be attributed to the substitution location of N in the TiO_2 lattice, in which an O (Ti) atom is replaced by a N atom[167–171].

X-ray diffraction (XRD) is used to reveal information about the crystal structure and chemical composition of materials. XRD patterns of the pristine and N-TiO_2 nanoparticles are shown in Figure 5-4. An anatase characteristic diffraction peak appears at 25.28° and a rutile diffraction peak shows at 27.35°, which are in well accordance with the (101) diffraction peak of anatase TiO_2 (PDF 21-1272) and the (110) diffraction peak of rutile TiO_2 (PDF 21-1276) [68][172]. Compared with the pristine material, there is no significant difference of XRD patterns between these two samples, except that slightly enhanced diffraction peak intensity at 2 Theta of 25.28°, can be observed for the N-TiO_2 sample. This position was the plane (101) of anatase phase. There is no peak shift for the N-TiO_2 sample, and this is due to the small amount of nitrogen doping content[173]. The crystallite size was calculated for both of the samples using the Scherrer equation, which is shown as follows:

$$D = K\lambda/\beta\cos\theta \qquad (5\text{-}1)$$

Where D is the average crystallite size of the sample, K=0.89, λ is X-ray wavelength (0.154 nm), β represents the full width at half maximum (FWHM) of the sample, and θ is the diffraction angle. The calculated crystalline size is 16.41 and 16.43 nm for pristine TiO_2 and N-TiO_2, respectively.

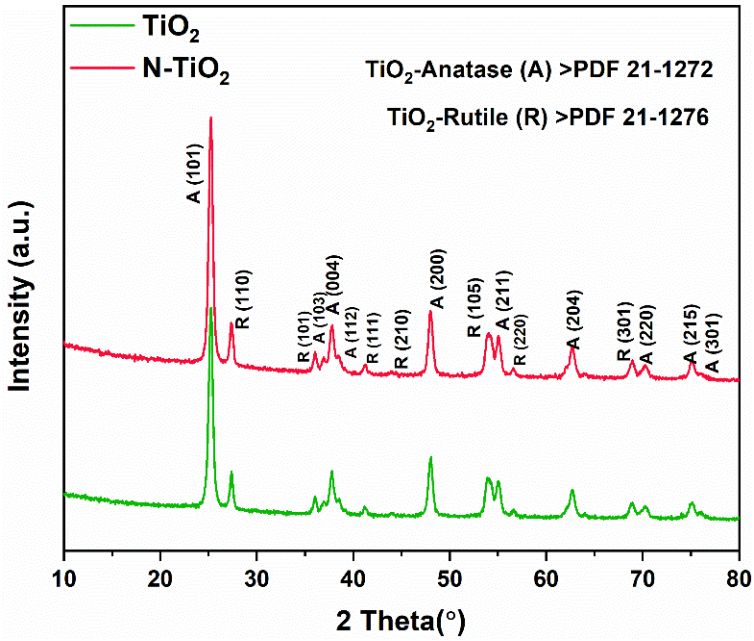

Figure 5-4 XRD patterns of pristine TiO_2 and nitrogen doped N-TiO_2.

X-ray photoelectron spectroscopy (XPS) was employed to further investigate the surface bonding information of TiO_2 samples. Figure 5-5 (a) shows the XPS survey spectra of pristine and N-TiO_2. Oxygen (O), titanium (Ti) and carbon (C) can be observed in the samples. There were no significant differences in the XPS survey spectra of N-TiO_2 compared with pristine TiO_2. In order to get more detailed chemical binding information about all the elements, the high-resolution XPS spectra of Ti 2p and O 1s and N 1s of N-TiO_2 were analyzed. As shown in Figure 5-5 (b), the Ti 2p XPS spectrum of pristine TiO_2 shows two typical Ti $2p_{1/2}$ and $2p_{3/2}$ peaks centered at 464.3 and 458.5 eV respectively, corresponding to the characteristic peaks of Ti^{4+}. For the N-TiO_2, the peaks positions just shifted 0.1 eV to the higher binding energy. That means the change of chemical environment of titanium is not obvious after nitrogen plasma treatment. The XPS spectrum of O 1s of pristine TiO_2 is shown in the upper panel of Figure 5-5 (c). There is only one characteristic peak centered at 529.7 eV, corresponding to O^{2-}. For the spectra of N-TiO_2, as shown in the lower panel of Figure 5-5 (c), except the same peak of TiO_2, there are two new characteristic peaks which are centered at 530.3 and 532.1 eV, respectively. Especially, the binding energy of the left peak (532.1 eV) is very high and could be

corresponded to the presence of Ti-O-N bonds[174]. György et al [175] assigned this feature to the formation of oxidized Ti-N, which leads to the Ti-O-N bond. And the other extra peak centered at 530.3 indicating the nature of oxygen. In summary, these results manifest that the doping of nitrogen atoms into TiO_2 can cause an increase of oxygen vacancies.

And the high-resolution XPS spectrum of N 1s of N-TiO_2 was shown in Figure 5-5 (d). According to the XPS results, the atomic concentration of nitrogen in N-TiO_2 is about 0.48 %. Being affected by the noise, the reflection signal of nitrogen is weak, and we made a smoothing spectrum firstly. There are only two characteristic peaks which are centered at 399.4 and 409.8 eV, respectively. The first peak (399.4 eV) can be attributed to interstitial N [174]. According to some previous work, NO or NO_2 type species usually appear above 400 eV [175]. So, another peak (409.8 eV) belongs to this situation. Most researchers accept that an N 1s peak at $\leq$ 397.5 eV is characteristic of O-Ti–N linkages, which result from doping of nitrogen atoms into a TiO_2 lattice [176,177]. Therefore, changes of the nitrogen environment can produce significant differences in the N 1s XPS spectral region. From the above observations the chemical states of the nitrogen doped into TiO_2 may be various and exist in the form of N-Ti-O and Ti-O-N[176]. Many research works have reported that the role of N species on the electrical conductivity of TiO_2 is mainly related to the decrement of the band gap, and this is matched well with the UV-Vis results, since the nitrogen doping can elevate the valence band maximum[177].

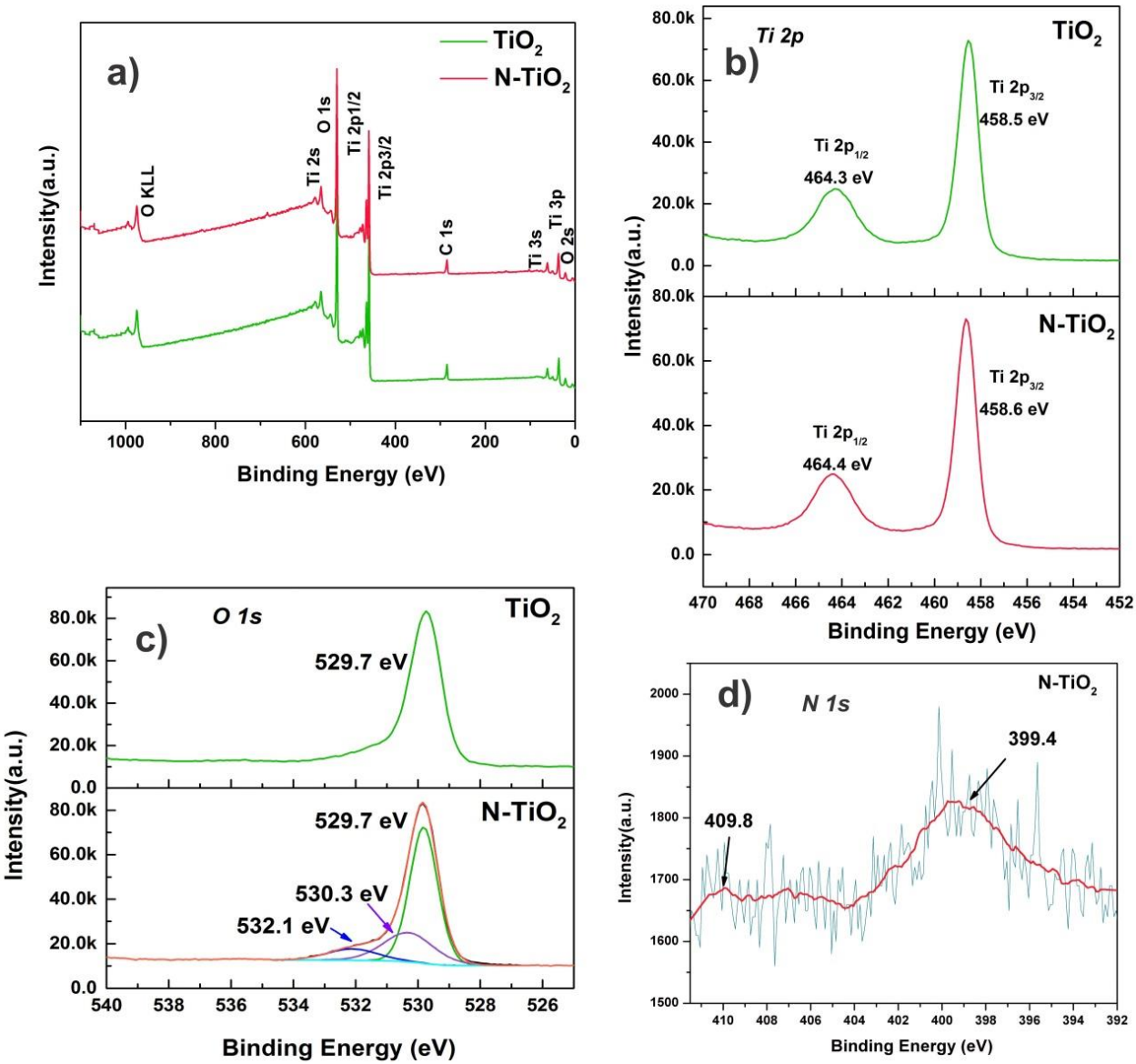

Figure 5-5 (a) The XPS survey spectra of TiO_2 and N-TiO_2; (b) Ti 2p spectra of TiO_2 and N-TiO_2; (c) O 1s spectra of TiO_2 and N- TiO_2; (d) N 1s spectra of N- TiO_2.

5.2.2 Electrochemical performance for SIBs

Coin cells were fabricated to investigate the electrochemical performances of the as-prepared TiO_2 anode materials for sodium ion batteries. Cycle voltammetry (CV) plots are shown in Figure 5-6 (a)(b), which were evaluated at a scan rate of 0.5 $mV \cdot s^{-1}$ at the voltage range of 0.01-3.0 V for 3 cycles of each sample. Both of them exhibit the typical CV curves of TiO_2 anode for SIBs[60,178]. The irreversible broad cathode peaks in a wide potential range of 0.01-0.5 V of the first cycle are observed for both electrodes, which are caused by the solid electrolyte interface (SEI) layer formation, irreversible sites for Na-ion insertion in the crystal lattice defects, electrolyte and other organic material decomposition[64,178]. From the second cycle on, the electrode shows only the peaks at around 0.78 and 0.85 V in the CV profiles (Figure 5-6 (a)(b)), which we attributed to the reversible insertion/de-insertion of Na into/from TiO_2 and N-TiO_2 electrodes. The large irreversible capacity likely originated from the electrolyte decomposition and SEI layer formation during the first cycle and disappeared from subsequent cycles. And except the first cycle, the CV curves overlapped well for the following cycles, demonstrating high reversibility and good cycling stability of the electrode. In addition, the peaks of the N-TiO_2 are wider and stronger than those of the pristine TiO_2 material, and it means N-TiO_2 shows a better performance for the sodium storage application (Figure 5-7).

The rate performance of the samples is shown in Figure 5-8 (a) (b), all of the samples were investigated at a current density of 0.1, 0.5, 1.0, 2.0 and 5.0 C for 4 cycles of every current stage, and then back to 0.1 C for 10 cycles of the last rate stage (1C= 335 $mA \cdot g^{-1}$). The first cycle discharge/charge specific capacities of the samples are 584.28/112.08, 621.59/132.86 $mAh \cdot g^{-1}$ for pristine TiO_2 and N-TiO_2, respectively. Both of the materials show very low coulombic efficiencies of about 20 % for the first cycles. The loss of capacities was mainly caused by the occurrence of the side reactions to form a solid-electrolyte interface (SEI). When the current densities are 0.1, 0.5, 1.0, 2.0, 5.0 and 0.1 C, the discharge specific capacities of N-TiO_2 were 202.2, 129.2, 114.4, 86.4, 76.2 and 161.81 $mAh \cdot g^{-1}$, respectively; while for the pristine TiO_2 electrode, they were 184.3, 104.3, 93.5, 63.8, 49.36 and 124.6 $mAh \cdot g^{-1}$, the N-TiO_2 shows an obvious improvement of the capacities. When the current density goes back to 0.1 C, a charge capacity of about 161 $mAh \cdot g^{1}$ could be obtained for N-TiO_2, while the pristine TiO_2 is much lower,

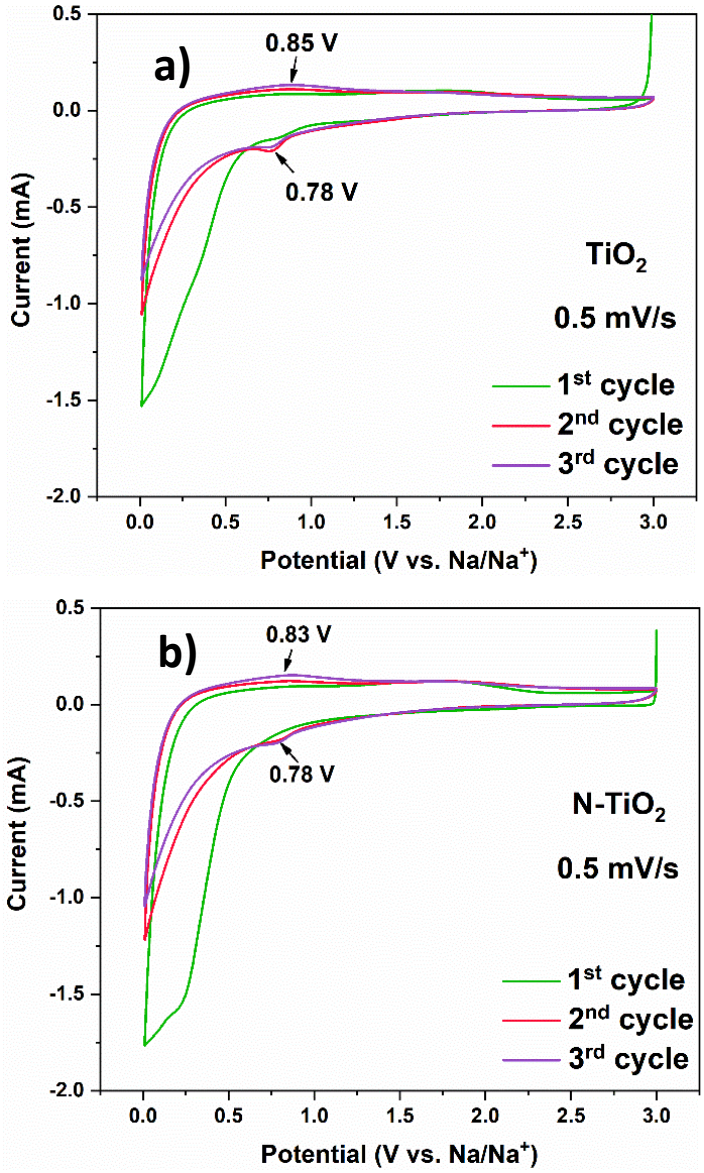

Figure 5-6 CV curves for the electrodes measured at a scan rate of 0.5 mV $\cdot s^{-1}$, (a) N-TiO_2; (b) TiO_2.

around 125 mAh$\cdot g^{-1}$. Both of them show good recover of the specific capacities, this is due to the good stabilities of the TiO_2 as anode materials for secondary batteries. Figure 5-9 (a) is the first discharge/charge curves of both electrodes at the current rate of 0.1 C. There is a long voltage plateau from 0.5 V to 0.01 V for the first discharge curves, consistent with CV results. From the galvanostatic discharge/charge curves, we could know that firstly, a higher first discharge specific capacity is achieved for the N-TiO_2 than the pristine TiO_2 material; secondly, the higher charge capacities are obtained for N-TiO_2 when the charge voltage is over than 1.0 V, it means that the reversible charge capacities of N-TiO_2 are higher than the pristine TiO_2

electrode. Furthermore, the galvanostatic discharge/charge curves of the electrode at different current densities show the similar results (Figure 5-9 (b)(c)), and N-TiO_2 displays higher discharge/charge capacities and much slower performance fading at all different current stages. All these results give solid proofs of the considerable performance improvement of the N-TiO_2 electrode.

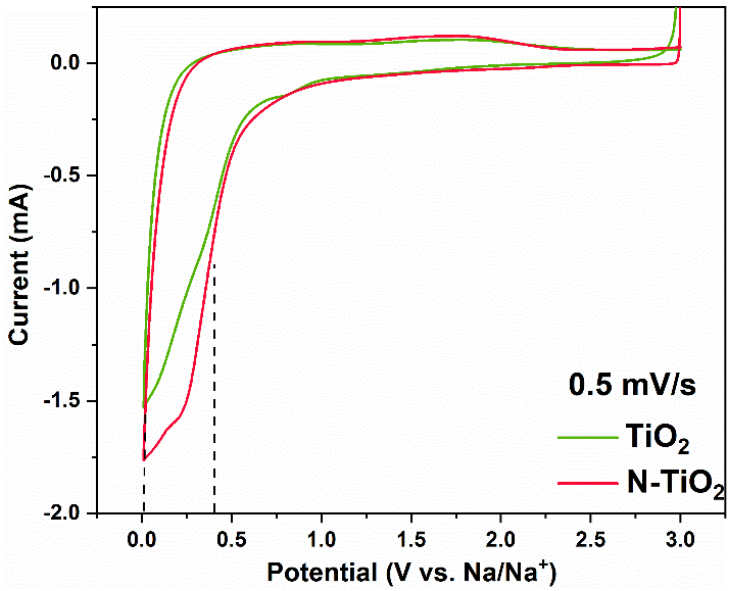

Figure 5-7 CV curves of two TiO_2 electrodes at a scan rate of 0.5 mV· s^{-1}.

To further understand the improved rate performance of the N-TiO_2 electrodes, electrochemical impedance spectra (EIS) was evaluated in the frequency range of 100 kHz to 0.01 Hz (as shown in Figure 5-10). The Nyquist plots consist of an incline line in the low-frequency region and on semicircle in the high-frequency region. The incline line represents Warburg impedance (W1) corresponding to the sodium ion diffusion resistance in a solid electrode. The small intercept at the Z' axis demonstrates the inter resistance of electrodes (Rs) while the semicircle corresponds the charge-transfer impedance on the electrode-electrolyte interface (R_1)[179]. CPE1 represent a constant phase [180]. The charge transfer resistance (R_1) of the pristine sample is about 137 Ω, while that of the N-TiO_2 is less than half of the pristine TiO_2 (ca. 50 Ω), and higher value of R_1 has been demonstrated as an important contributor to the capacity fading of active electrode. The results clearly indicate that the plasma treatment results in a large reduction of the charge transfer resistance and a clear improvement of electrical conductivity due to incorporation of N doping atoms and formation of a disordered surface layer.

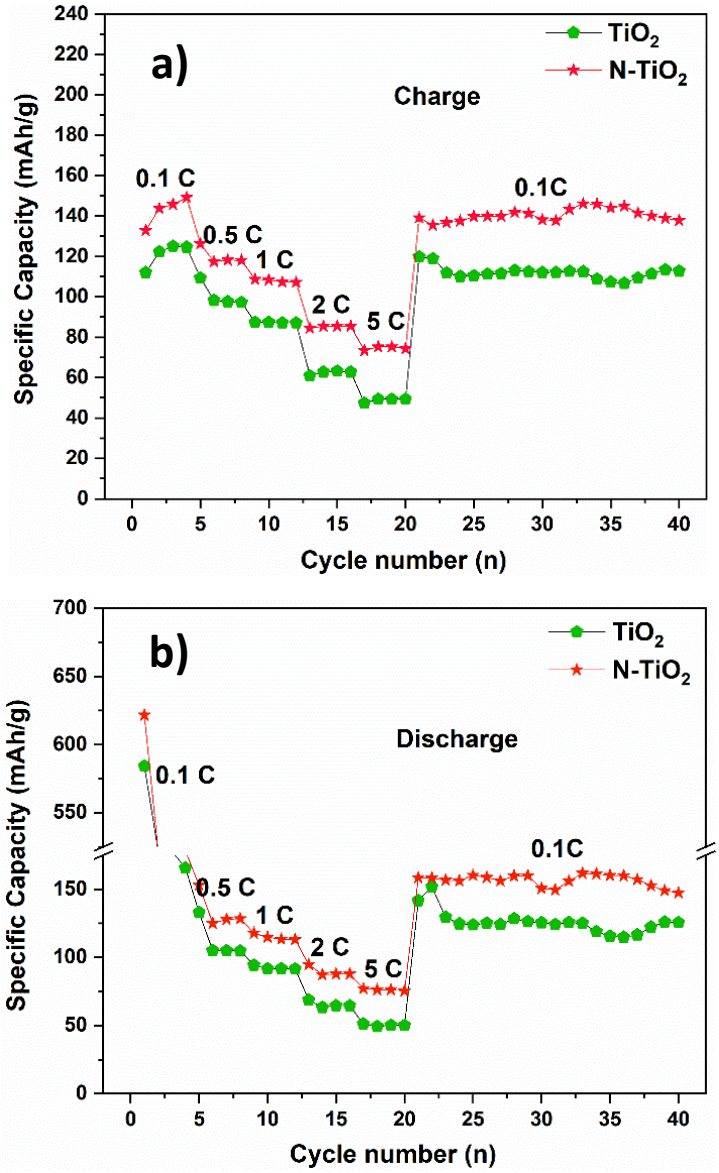

Figure 5-8 Rate performances of TiO_2 and N-TiO_2 at the current densities of 0.1, 0.5, 1.0, 2.0 and 5.0 C, (a) Charge, (b)Discharge.

To evaluate the long cycling stabilities of the materials, we cycled the materials at a current rate of 1 C for 400 cycles. As shown in Figure 5-11 (a)(c), the first cycle discharge/charge specific capacities of the pristine TiO_2 and N-TiO_2 electrodes are 304.7/64.2, 338.7/71.4 $mAh \cdot g^{-1}$, respectively. Both of the materials show a very low coulombic efficiency of about 21% in the first cycle. However, at such high current density, N-TiO2 still shows good long cycling specific capacities compared with other literatures' report [57,71,75,181,182]. Especially, it should be noted that our plasma treated N-TiO2 nanoparticles were not combined with any other carbon materials as composite electrode material, but showed a promising long cycling capacity as well. It is believed here that in addition to the N doping, the disordered

surface layer plays also an important role on enhancing the electrochemical performance. It has been reported that similar disordered surface layer on TiO_2 nanoparticles formed after H_2 plasma treatment can clearly enhance the rate performance for LIB due to the enhanced pseudocapacitive storage contribution[113].

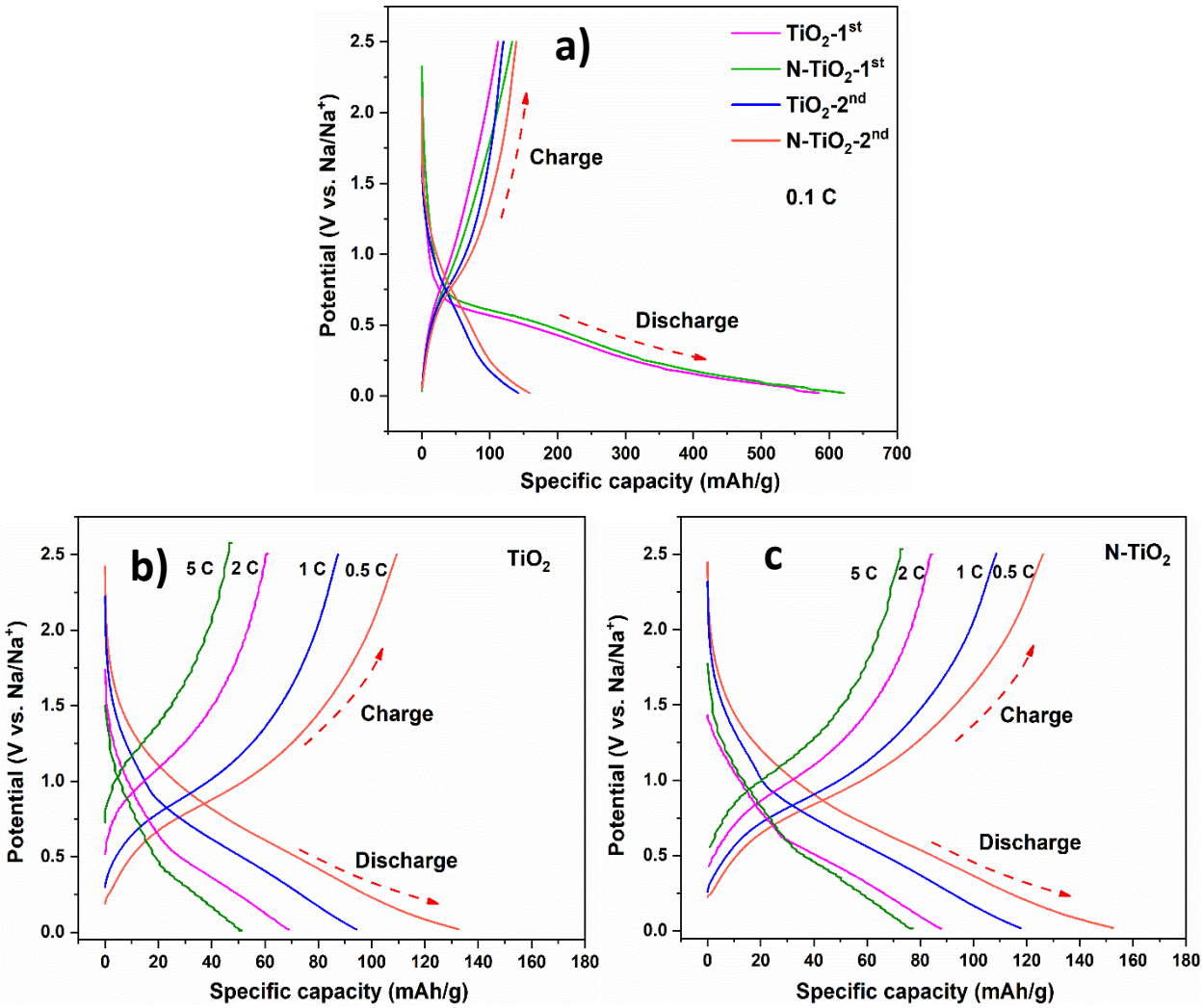

Figure 5-9 (a) Discharge/charge curves of electrodes at current density of 0.1C; Discharge/ charge curves at different current densities (b)TiO_2, (c) N-TiO_2.

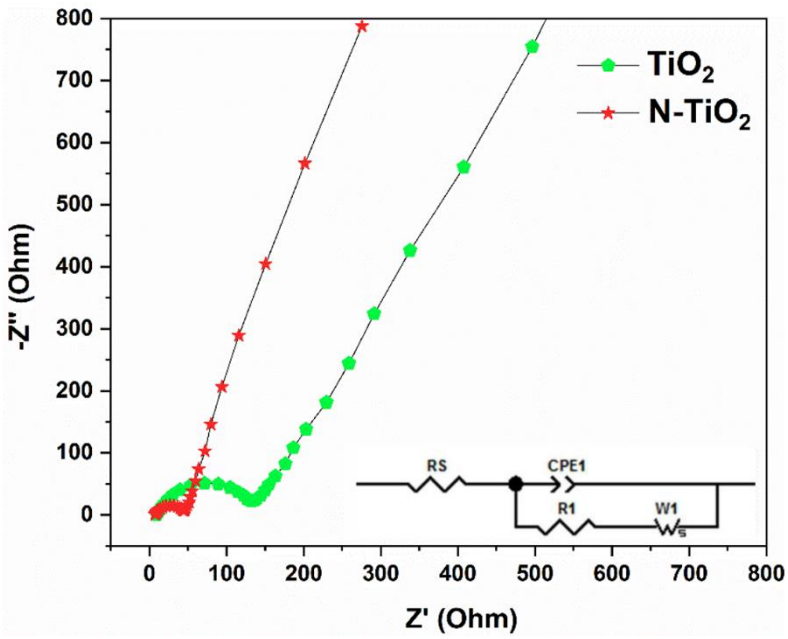

Figure 5-10 Nyquist plots for TiO_2 and N–TiO_2.

After about 20 cycles, the N-TiO_2 show about 25 % of capacity higher than the pristine TiO_2. During the long cycling performance test, the two electrodes maintain good long cycling stabilities, the coulombic efficiencies are nearly 98 % after 50 cycles, and this great CE could be sustained to the last cycles of long cycling test (Figure 5-11(e)). This excellent cycle performance is believed to be due to the advantage of the structural stability of TiO_2 itself. Remarkably, what we could notice from Figure 5-11 is that the N-TiO_2 reached the stable high coulombic efficiency earlier than the pristine TiO_2 material. After 400 cycles, the N-TiO_2 shown a discharge/charge specific capacities of 61.8/60.6 $mAh \cdot g^{-1}$, and it could be kept for around the last 300 cycles. While for the pristine TiO_2 electrode, the discharge/charge specific capacities are only 47.40/46.44 $mAh \cdot g^{-1}$ at the 400^{th} cycle, it also shown a great stability for the long cycling performance, but much lower discharge/charge capacities. Figure 5-10 (b) (d) display the galvanostatic discharge/charge curves of electrodes at different cycles of the long cycling test, the curves are quite similar for these two materials, but the capacities fading of N-TiO_2 is much slower than the pristine TiO_2 material. The similar with the rate performance, the reversible charge capacities of N-TiO_2 are higher than the pristine TiO_2 electrode (The red circle in Figure 5-11 (d)). In general, most of the TiO_2 anode materials are carbon composited which could increase the conductivity of the material a lot and improve the energy storage performance[70,74,181,183]. However, there are still some research which are just nitrogen

doped TiO_2 anodes. Liu and co-workers reported a nitrogen-doped TiO_2 nanospheres for SIBs[76], which exhibited a stable capacity of 162 $mAh \cdot g^{-1}$ over 1000 cycles at 1 $A \cdot g^{-1}$. The nitrogen content in the sample was calculated from the XPS results to be about 1.75 wt % (Another nitrogen-doped ordered mesoporous anatase TiO_2 nanofibers anode with a nitrogen atomic content of 1.86 % was reported by Wu[184], which shown good rate and cycling performances as well. The authors claimed that the improvements can be attributed to the nanosized particles and pores which could shorten the diffusion length of Na ions in TiO_2 and also allow sufficient infiltration of electrolyte and allow fast diffusion of Na ions. Compared to these works, our specific capacity is not that good, but in our situation, the content of nitrogen is just around 0.48 At % and also without any special nanostructure. After the nitrogen plasma treatment, the improvement of our anode material is quite promising. Here, we believe that the nitrogen plasma treatment could serve as a model for simple modification of other oxides which could result in a nitrogen doping and also the formation of the disordered surface layer.

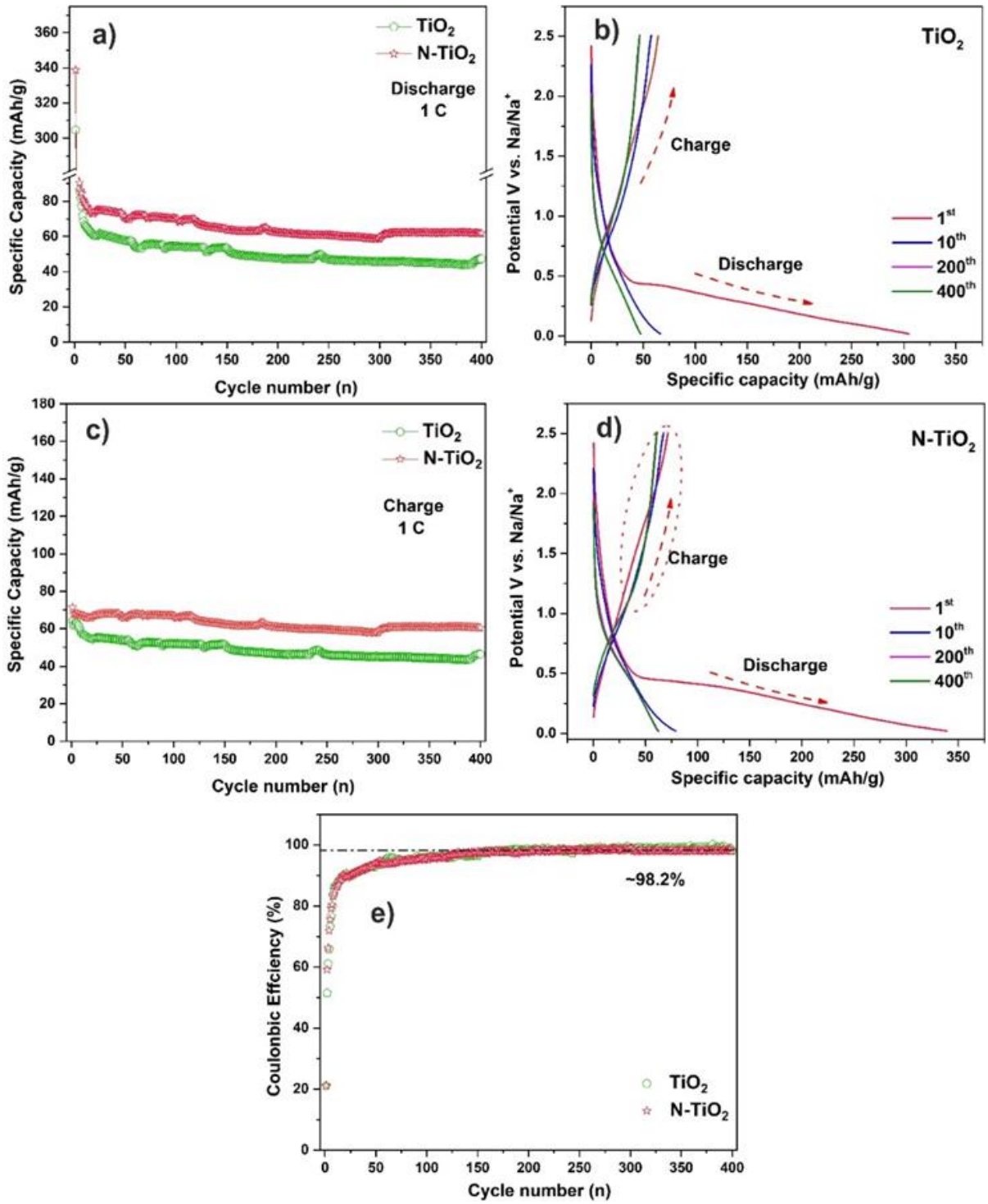

Figure 5-11 Long term cycling performances of electrodes at a current rate of 1 C (a) discharge; (c) charge; Discharge/charge curves of electrodes at different cycles (b) TiO_2; (d) N-TiO_2. (e) Coulombic efficiencies for long cycling performances of TiO_2 and N-TiO_2.

5.3 Conclusions

In summary, N-TiO_2 nanoparticles have been synthesized via high power N_2 plasma treatment. Comparing with other synthesis methods, a disordered surface layer is formed in addition to the N doping after the treatment. Both disordered surface layer and N doping have a collective effect on the rate performance enhancement when used as the anode materials for sodium-ion batteries. What's more, when the samples are tested for the anode materials of SIBs, the N-TiO_2 shows a great cycling stability. In addition, the electrochemical impedance spectroscopy (EIS) reveals a drastic decrease of the charge-transfer resistance from 137 Ω (pristine TiO_2) to about 50 Ω (N-TiO_2), which implies the plasma treatment for electrode material is more effective method for enhancing the electron transport during the sodium ion insertion/extraction process.

6. Hydrogen Plasma Treated TiO_2-Au Composite with Enhanced Performance Used for Electrochemical Reduction of Nitrogen

6.1 Introduction of TiO_2-Au for NRR electrocatalysts

As NH_3 serves an attractive hydrogen storage medium and a renewable energy sector, also a significant source of nitrogen for fertilizer, finding an easy, economic and cleaning method for the ammonia producing is quite urgent for modern society. Electrochemical nitrogen reduction reaction under room temperature and ambient pressure is considered as a good choice for the nitrogen fixation to ammonia. At this moment, for the nitrogen fixation electrochemical catalysts, there are already a lot of works have been carried out [92,185–188]. Unfortunately, in most of the studies, the efficiency of ammonia production is quite low. To progress toward achieving both high-performance and selective electrochemical catalysts at ambient temperature and pressure for NRR is a great challenge for us now. Because of the low HER activity of gold(Au) particles [94,189], Au is a good choice for NRR processes. However, to effectively utilize the high cost and desired performances of Au, preparing metal particles onto oxide supports to obtain a well catalyst system has been proved to a great method for considerable catalytic performances. Thus, TiO_2 could be a good choice due to the low cost and high stabilities. Furthermore, black TiO_2 was consider valuable for photocatalysts[99–102], as well as secondary batteries [103,190] and supercapacitors [7], because black TiO_2 presents surface oxygen vacancies, disordered surface of point defects and sometime with Ti^{3+} ions, which could give great contributions when used as a electrochemical catalysts. What's more, the interactions between metals and supports, especially the strong metal−support interaction (SMSI), are widely proposed as a key factor in determining catalytic performances toward important chemical reactions[191]. The SMSI changes the catalytic activity and selectivity of the metal particles because the it influences the electronic properties and the morphology of metal particles, and causes the modification of metal particles with reduced supports (e.g., TiO_2) generated by H_2 treatment at high temperature[192]. Thus, we wonder how will the hydrogen plasma treatment change the surface structure between TiO_2 support and Au

nanoparticles. Also, to our best knowledge, there is seldom works which used black TiO_2 as the support for gold particles working as electrochemical nitrogen reduction reaction catalysts.

In this research, we chose the TiO_2/Au (gold nanoclusters supported by P25 TiO_2 nanoparticles, Au load: ~ 2 wt %) and hydrogenated TiO_2/Au as the electrochemical catalysts for the nitrogen reduction reaction. The pristine TiO_2/Au has purple red color due to the plasmonic effect of Au nanocluster. After H_2 plasma treatment, the sample color is changed to blue-black, and shows enhanced performance for the NRR process comparing with the original sample. From the TEM investigations we could find some disordered positions on the layer surface, and a strong metal−support interaction could be observed from the TEM results. Then the Raman intensities of H-TiO_2-Au is much lower than the pristine material which could be attributed to the disordered surface and the oxygen vacancies formation. What's more, a small peak shift for the XPS could be found after the hydrogen plasma treatment. The formation of the disordered surface makes an important role on improving the performances of catalyst. The yield of the NH_3 is about 9.5 times increasing of the blue-black H-TiO_2-Au compared with the pristine TiO_2-Au. What's more, after the hydrogenation process, the surface of the sample is very different from the control sample. As a comparison, we also used O_2 plasma treated the hydrogenated material (H-O-TiO_2-Au) and test the catalyst activity of H-O-TiO_2-Au, as what we expected, the lightly oxidized material shows worse performance for the NRR, while it is better than the pristine materials. This improvement could be attributed to the disordered surface formation which comes from the hydrogen plasma treatment, which we could find from the TEM and XPS characterizations. This could be the first time that used the plasma technique to modify catalyst for NRR process. We hope this work could give some reminder for future electrochemical NRR catalysts.

6.2 Results and discussions

6.2.1 Characterizations

The XRD patterns of samples are shown in Figure 6-1 (a). For all samples we could find two different TiO_2 diffraction peaks: anatase TiO_2 marked with "A" and rutile TiO_2 marked with "R". The characteristic diffraction peaks corresponding to anatase TiO_2 (101), (004), (200), (105), (211), (204), (220) and (301) reflections can be found at 2θ = 25.28, 37.80, 48.05, 53.89, 55.06, 62.69, 70.31 and 76.02° (PDF card 21-1272), respectively. While the peaks located at 2θ=27.43, 36.08, 39.19, 41.24, 54.32, 56.62, 69.00 and 76.53° could be attributed to (110), (101), (200), (111), (211), (220), (301) and (202) diffractions of rutile TiO_2 (PDF card 75-1754). And because the deposition of gold is very low, we can just find some small peaks at around 38.18, 44.38 and 64.57° for the (111), (200) and (220) reflections for Gold (PDF card 65-2870). Compared the diffraction results before and after hydrogenation, nearly there is no obvious differences could be observed.

Raman spectroscopy is a powerful tool for the investigation of various phase of TiO_2. To future reveal some more details of P-TiO_2-Au after hydrogenation process, Raman spectroscopy is carried out to measure the changes of the obtained specimens, which was performed in the range of 50-1000 cm^{-1}, and the results are shown in Figure 6-1 (b). The observed Raman peaks at 151.43, 202.81, 391.77, 515.85 and 632.32 cm^{-1} could be attributed to anatase TiO_2. In general, there will be two peaks at around 448 and 800 cm^{-1} which will be attributed to the rutile TiO_2. But in our results, the peaks are not obvious enough to be observed. What's more, we could find there is no much information about gold maybe because of the low loading of gold particles. However, comparing with the pristine TiO_2-Au sample, the intensity of the peaks decreased a lot after the plasma treatment. The color of the samples changed a lot after the hydrogen plasma treatment process. From Figure 6-2, we know the original TiO_2-Au is purple red, after hydrogenation, it changed to blue-black. And the black color turned a bit lighter after the O_2 plasma process.

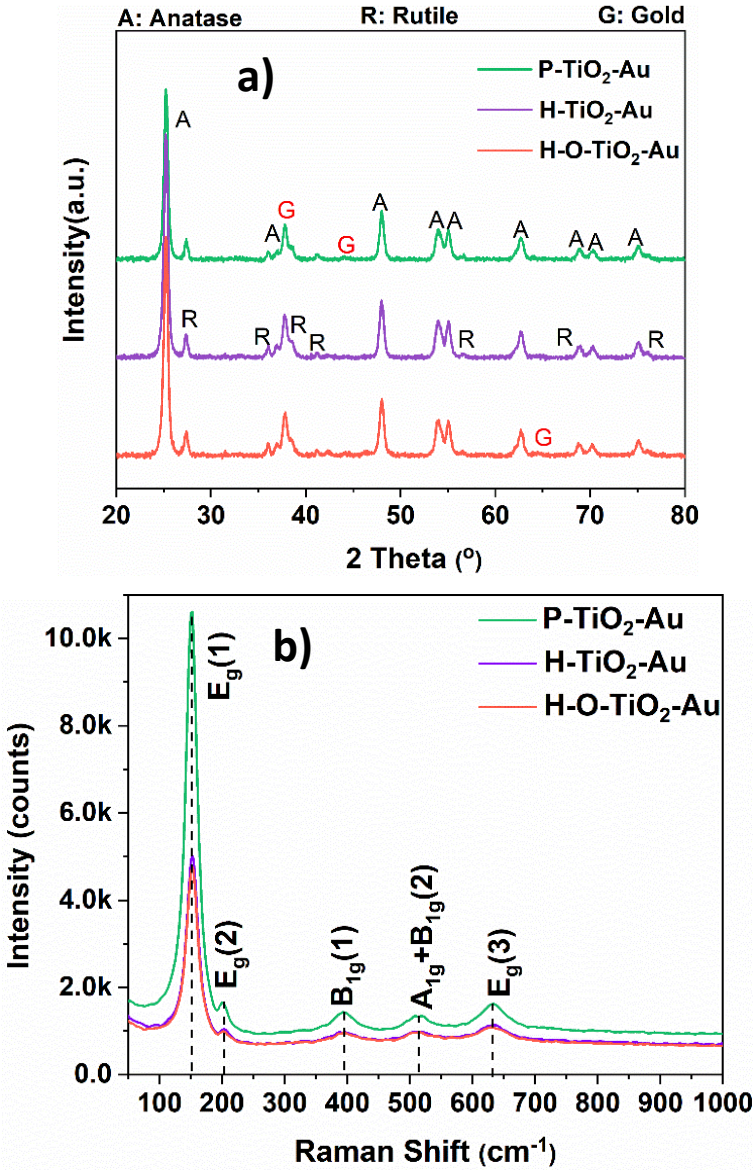

Figure 6-1 (a) XRD patterns and (b) Raman spectrum of P-TiO_2-Au, H-TiO_2-Au and H-O-TiO_2-Au.

The high-resolution transmission microscopy images of the three samples were shown in Figure 6-3. Gold particles with average size of 20 nm were observed for all samples. Compared the TEM photographs, we see some differences on the surface of Au and TiO_2 particles. From Figure 6-3 (a), we could see that the Au metal particle shown clear particle boundaries, while after hydrogen plasma treatment, the boundaries become a bit blurry, which is because of the interaction between the support and the metal [192]. When the sample was oxidized by the O_2 plasma a bit, the disordered surface was decreased a little (Figure 6-3 (d)), so we could know that the influences of the plasma treatment for the samples are quite obvious. Figure 6-4 told

us the EDS patterns of P-TiO_2-Au, H-TiO_2-Au and H-O-TiO_2-Au, Ti, O and Au elements could be found for all samples。

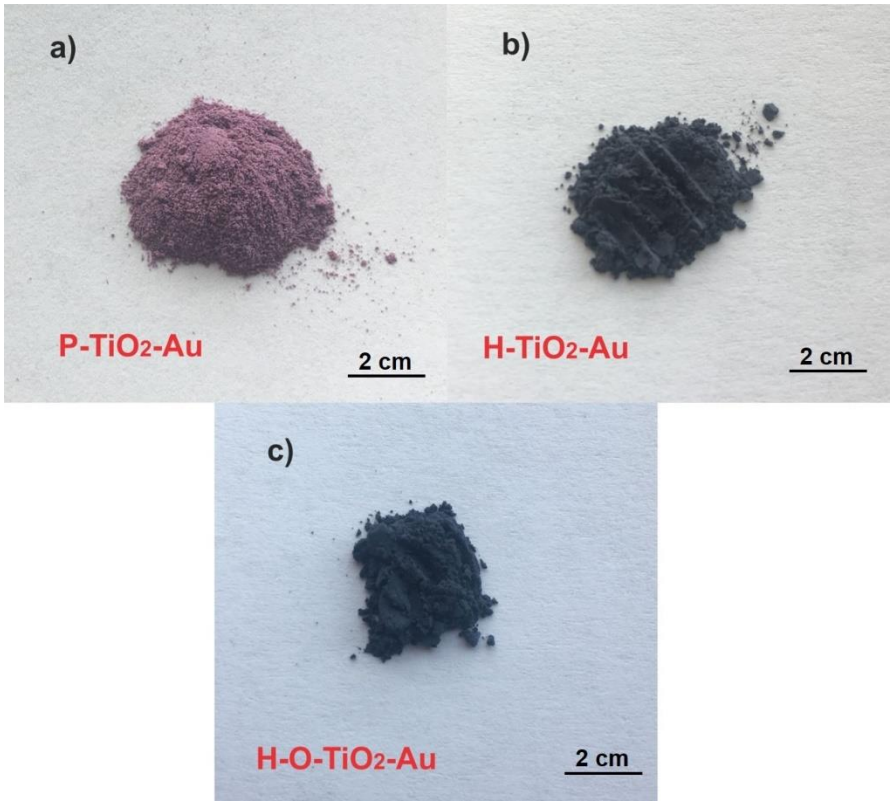

Figure 6-2 Photographs of (a) P-TiO_2-Au, (b) H-TiO_2-Au and (c) H-O-TiO_2-Au.

To investigate the optical properties of the TiO_2-Au samples, the absorbance spectra were measured by applying UV-Vis spectroscopy. Figure 6-5 (a) shows the absorbance spectra of the P-TiO_2-Au (green line), H-TiO_2-Au (purple line) and H-O-TiO_2-Au (red line), it clearly shows that the P-TiO_2-Au has a typical absorption behavior associated with the strong absorption in the UV range, and a big absorption peak at the wavelength of 550 nm. The appearance of the peak at 550 nm is due to the surface plasmon resonance effect[193]. The plasmon band at 550 nm can be ascribed to gold nanodots[194,195]. After the hydrogen plasma treatment, both of the H-TiO_2-Au and H-O-TiO_2-Au shown a very strong absorption in the UV range, but also the absorption in the whole visible region are quite strong compared to the P-TiO_2-Au sample. We calculated the optical band gap of the TiO_2-Au samples from a Tauc plot, shown in Figure 6-5 (b), as a plot of the $(ahv)^2$ versus hv curves.

$$\mathrm{ahv} = \mathrm{A}(\mathrm{hv} - \mathrm{E_g})^{\mathrm{m}} \tag{6.1}$$

Here, α is an absorption coefficient, A is a constant, hv is the incident photon energy, Eg is the optical band gap, and the value m is 2 for indirect transitions. The calculated band gaps for the P-TiO_2-Au, H-TiO_2-Au and H-O-TiO_2-Au are 3.02, 2.85 and 2.82 eV respectively. Obviously, after the plasma treatment process, a decrease of the band gap could be found, which we could attribute to the plasma treated disordered surface and the oxygen vacancies formation[196].

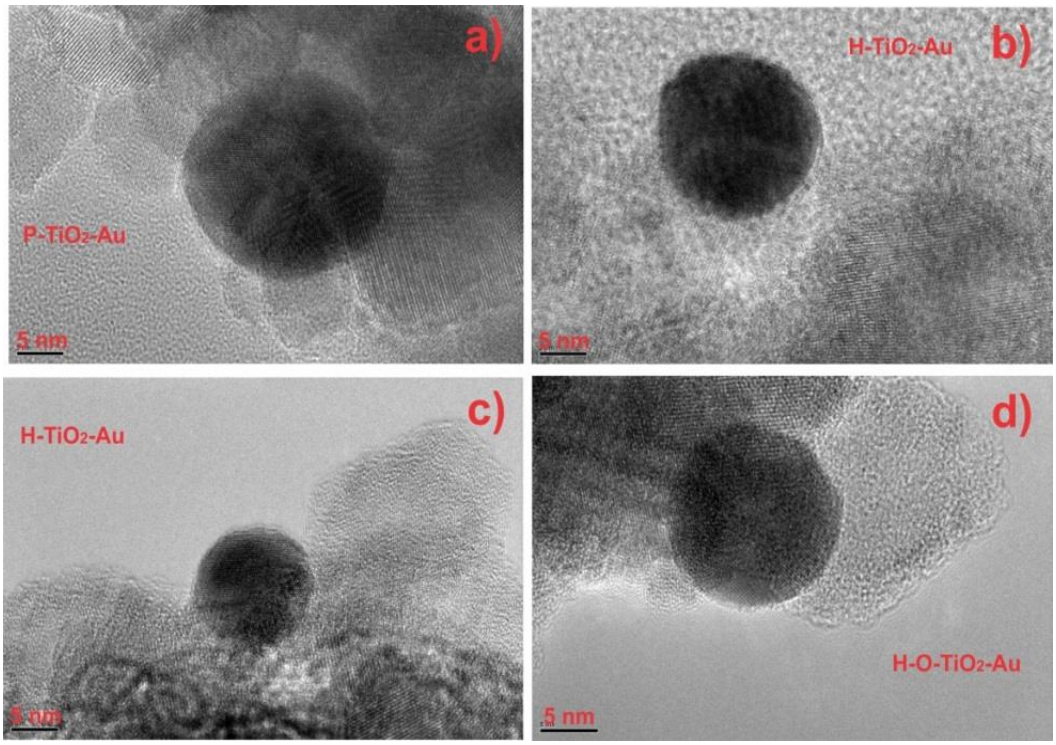

Figure 6-3 HRTEM images of (a) P-TiO_2-Au; (b), (c) H-TiO_2-Au and (d) H-O-TiO_2-Au.

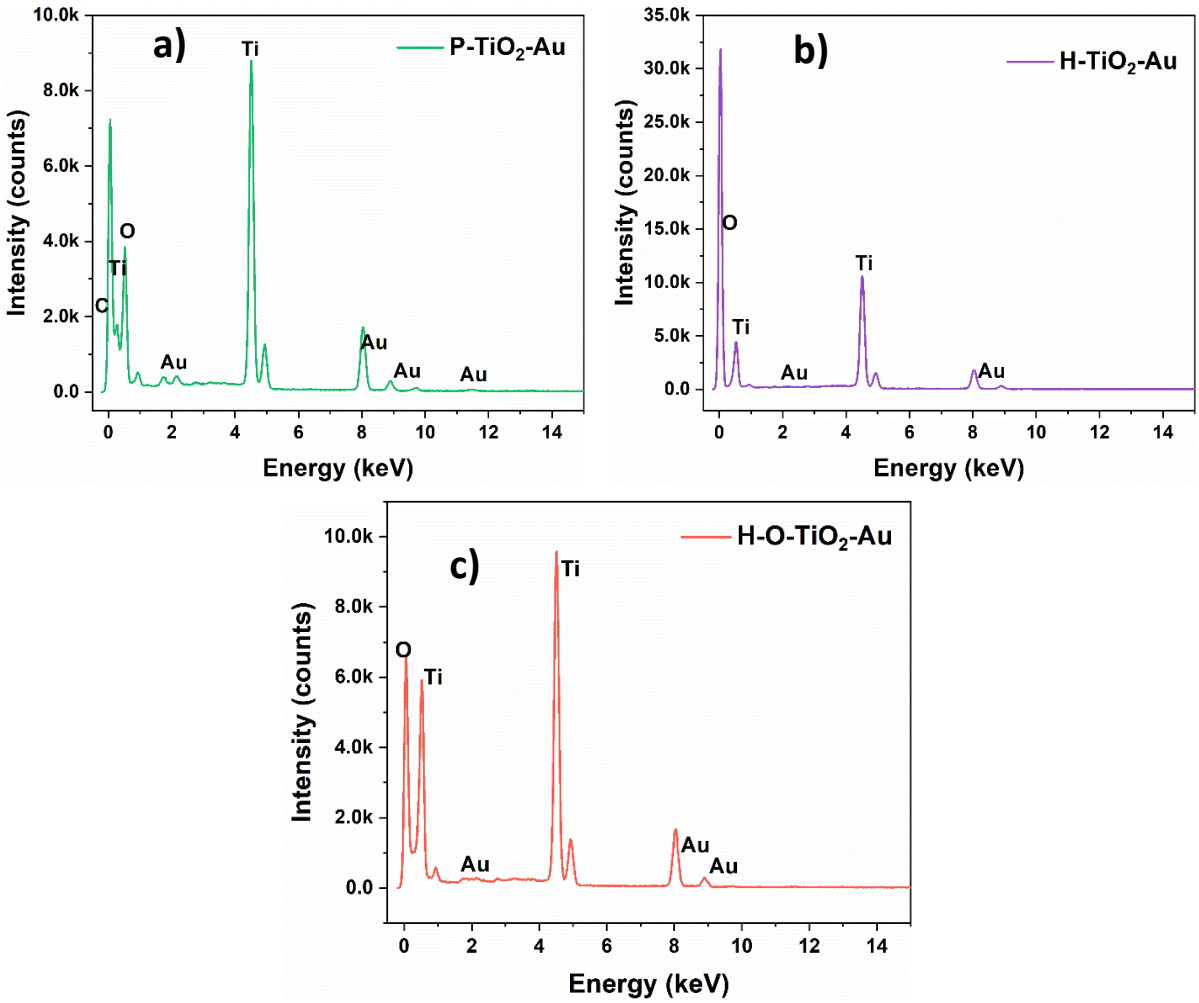

Figure 6-4 The acquired EDS patterns from TEM of P-TiO_2-Au, H-TiO_2-Au and H-O-TiO_2-Au.

The XPS spectrum of the samples is showed in Figure 6-6. From the full spectrum, we could see that Ti, O and Au elements could be found. And we almost didn't find any differences before and after hydrogenation. The high resolution spectrum of Ti 2p was shown in Figure 6-7 (a), there are two prominent peaks which located at around 458 and 464 eV, they could corresponding to the binding energies of the Ti $2p_{3/2}$ and Ti $2p_{1/2}$ to the Ti^{4+} of the TiO_2 [197,198]. From the spectrum we could find that after hydrogenation process, the peaks of Ti 2p shown a small shift to higher energy position compared to the original sample. The sample with hydrogen plasma treatment (H-TiO_2-Au) shown a higher shift than the sample which was treated by hydrogen and oxygen plasma (H-O-TiO_2-Au). For this shift we think that because of the hydrogenation process which could give some disordered surface and some oxygen vacancies on the samples[198].And then the high-resolution spectrum of O 1s is shown in Figure 6-7 (b), there is a peak at about 530 eV, which is due to the Ti-O bond. We could find

the same situation compare with the Ti 2p spectrum, H-TiO2-Au shown a higher binding energy than the original one, because the hydrogenated sample has much more OH species than others. From Table 6-1 we could know that after hydrogenation process, the ratio of O: Ti decreased a bit, so we thought that there is less oxygen atoms.

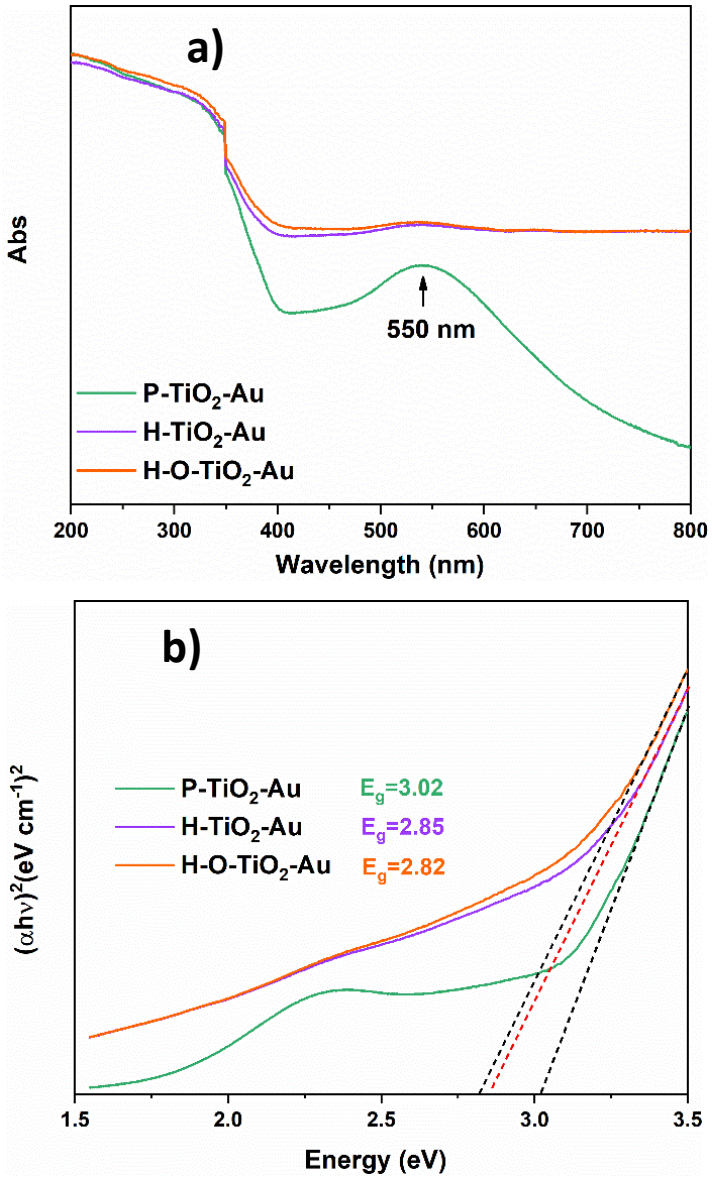

Figure 6-5 (a)UV-Vis absorption spectra of the TiO2-Au samples and (b) Tauc plots to obtain the band gaps.

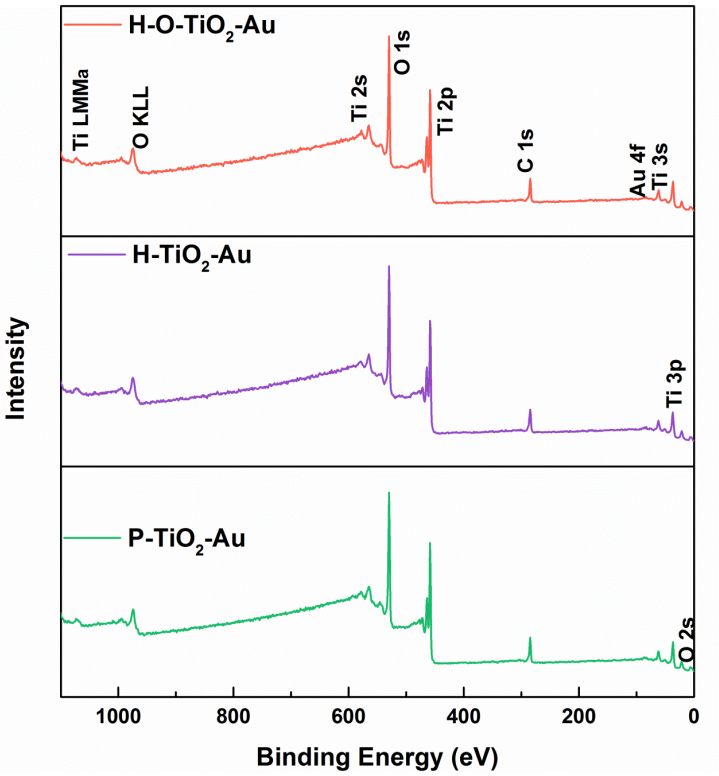

Figure 6-6 Full XPS spectrums of P-TiO_2-Au, H-TiO_2-Au and H-O-TiO_2-Au.

For Au 4f spectra, there are two peaks centered at about 83 and 86 eV, which could be attributed to Au $4f_{7/2}$ and Au $4f_{5/2}$, respectively. The same, after hydrogenation, a light shift to higher binding energy was shown, which could be influenced by the support oxygen vacancies on the surface. Table 6-1 shows the contents of elements O, Ti and Au in all three samples. First, the Au contents are the same for these three samples, and the ratios of O: Ti is a bit different. For the original sample, the ratio of O: Ti is about 2.05, after the hydrogenation process it became a bit lower (around 2.03), it means that there is less oxygen atoms in the H-TiO_2-Au sample. When we used the O_2 plasma treatment, the O ratio increased and became higher than the other two samples.

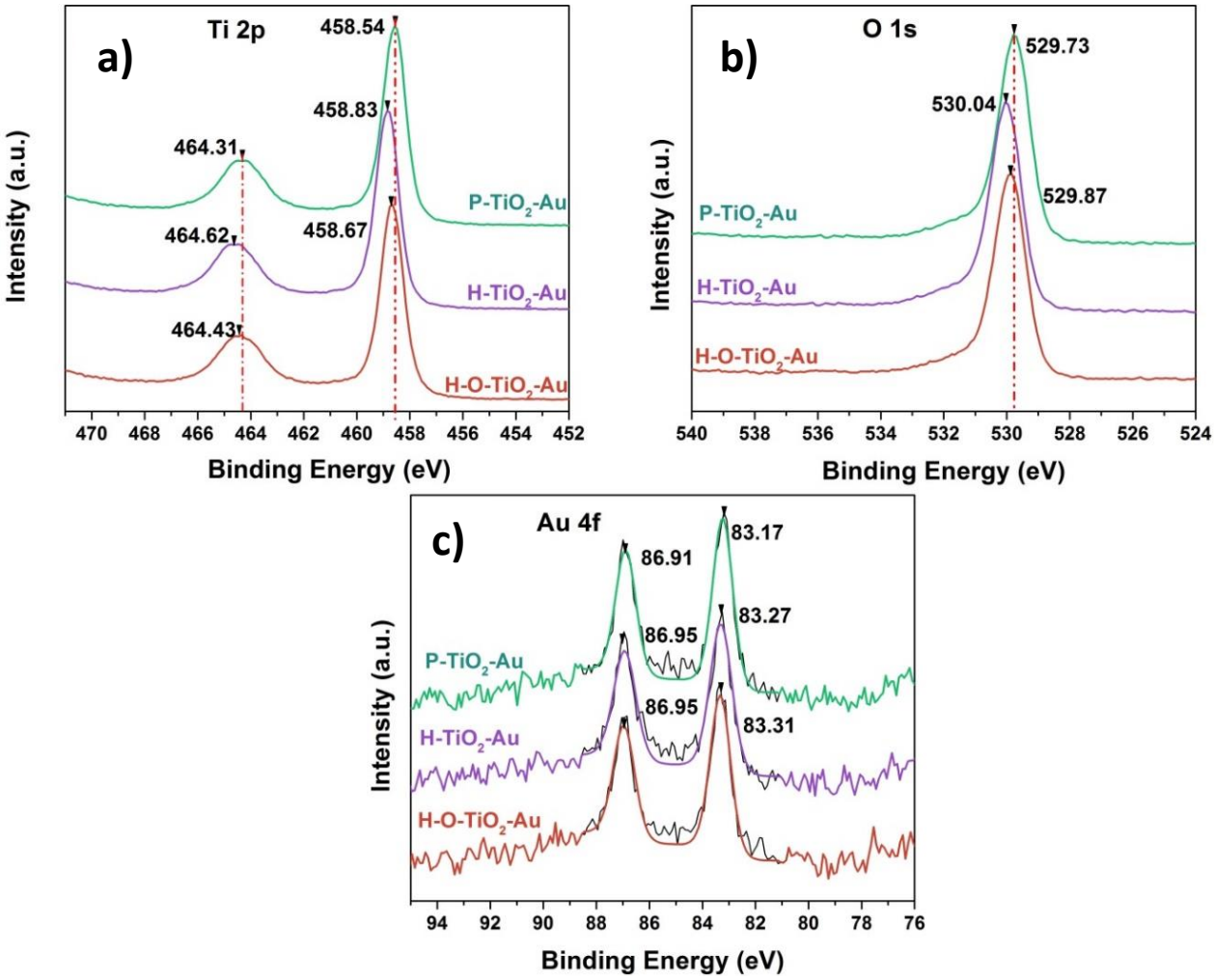

Figure 6-7 XPS spectrums of (a) Ti 2p,(b) O 1s and (c) Au 4f of P-TiO_2-Au, H-TiO_2-Au and H-O-TiO_2-Au.

Table 6-1 The concentrate of O, Ti and Au atoms and the ratios of O : Ti.

Sample	O 1s At %	Ti 2p At %	Au 4f At %	O: Ti
P-TiO_2-Au	47.79	23.28	0.11	2.05
H-TiO_2-Au	48.07	23.05	0.11	2.03
H-O-TiO_2-Au	48.99	23.55	0.11	2.08

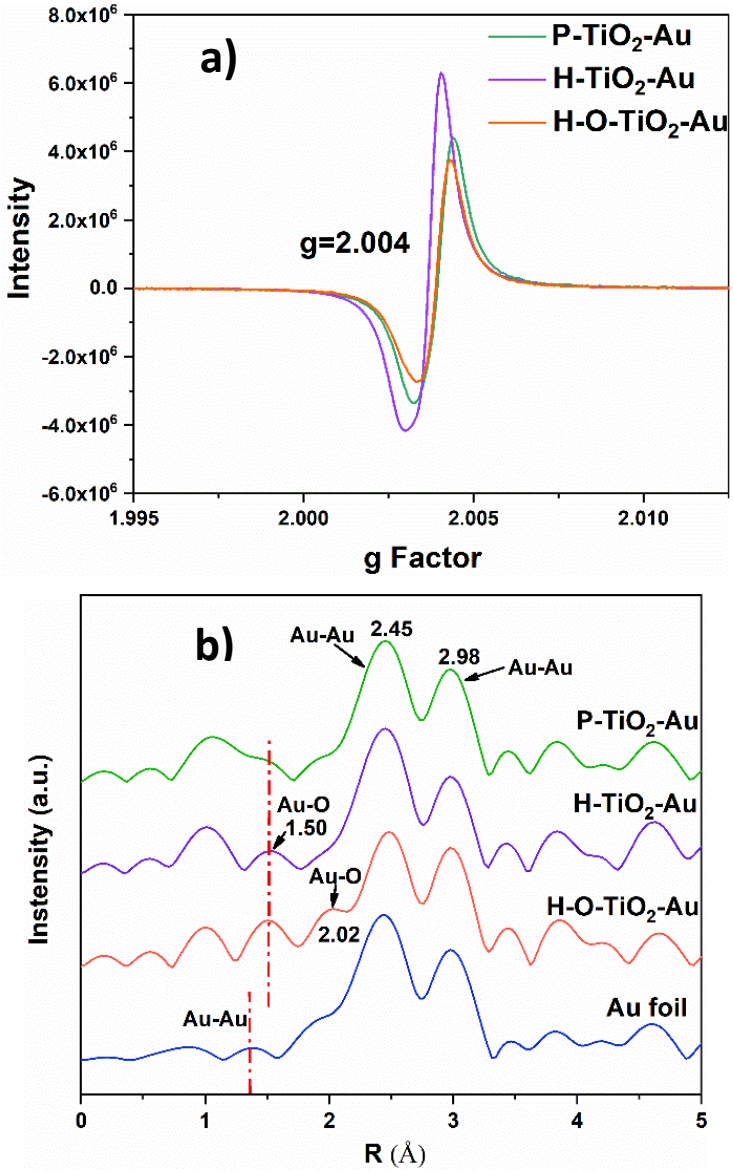

Figure 6-8 (a) The electron paramagnetic resonance (EPR) spectrum of all the samples; (b) Fourier transform (FT) of the Au L_3-edge of X-ray absorption spectrum.

And the electron paramagnetic resonance spectra of the three samples are shown in Figure 6-8 (a) to determine the possible unpaired electrons from the hydrogenation process. There is a big peak for the three sample which centered at g=2.004 could be attributed to the surface Ti^{3+} [101,199] , and single O_2^- radical trapped by O_2 adsorbed at oxygen vacancy [200]. The H-TiO_2-Au sample shown the highest intensity of the EPR signal, while the intensity of H-O-TiO_2-Au decreased a bit compared with the P-TiO_2-Au and H-TiO_2-Au. It means the oxygen vacancy is reduced after oxidation process. And we could say that the high-power hydrogen plasma treatment is an efficient method to introduce Ti^{3+} oxygen vacancies on the material surface. The X-ray absorption spectrum of the samples are displayed in Figure 6-8 (b), which

shows the short-range local structure of gold in the as prepared materials. We could find an obvious Au-O shell (R=1.5 Å) [201] for H-TiO_2-Au and H-O-TiO_2-Au, and the P-TiO_2-Au also shows an Au-O shell but the intensity is slightly weaker than the plasma treated materials. Compared with the other materials, H-O-TiO_2-Au gives us a new Au-O shell (R=2.02 Å), which could be attributed to the oxygen plasma treatment effect. And the main gold structure is Au-Au (R=2.45 and 2.98 Å) according to the Au foil spectrum. From the XAS results, we know that the hydrogen plasma treatment process didn't shown any kinds of new H-bonds, but the electronic atmosphere of the Au is changed which we could attributed to the metal-support interactions between Au particles and TiO_2 supporting materials, which we could see from the changes of TEM images.

6.2.2 Electrochemical nitrogen reduction reaction performance

After the materials characterizations, we used the TiO_2-Au composites as the catalyst for an electrochemical nitrogen reduction reaction. TiO_2-Au catalyst was used as cathodic catalysts, and NRR is initiated at different potentials versus RHE under N_2 saturation at room temperature and atmospheric pressure. During this experiment, N_2 gas is supplied in a feed gas stream to the cathode, where protons transported through the electrolyte (pH =1 HCl aqueous solution) reacted with N_2 to produce NH_3. From Figure 6-9 (a) we could know the yield of NH_3 during the NRR process at different voltages. When the reaction voltage is -0.1 V vs. RHE, the catalysts shown the best activities for nitrogen reduction reactions. The yield of H-TiO_2-Au is about 0.19 $\mu mol \cdot mg_{cat.}^{-1}$, while after a light oxygen plasma treated process, the yield of H-O-TiO_2-Au decreased to about 0.07 $\mu mol \cdot mg_{cat.}^{-1}$, it means after the oxidized process, with the decreasing of the disordered surfaces, the activity of the catalyst decreased a lot. While, the pristine sample (H-TiO_2-Au) without any modifications has the lowest NH_3 yield, just around 0.02 $\mu mol \cdot mg_{cat.}^{-1}$, it was just about first of nine of the NH_3 yield compared with H-TiO_2-Au catalyst. When we change the potential from -0.1 to -0.2, -0.3 and -0.4 V respectively, we find that the yield of NH_3 product decreased a lot for all the three samples, which could be attributed to the competitive adsorption of N_2 and hydrogen species on the electrode surface[94]. As the catalytic potential moves below −0.1 V versus RHE, the hydrogen evolution reaction (HER) will become the primary process in this catalytic system[84], which could be the main reason for a super low NH_3 production with a lower potential. Especially at the high potentials such as -0.3 and -0.4 V, the pristine TiO_2-Au (H-TiO_2-Au) didn't show any activity for the NH_3

producing, while the modified sample still worked well somehow, even the yield of NH_3 was quite low.

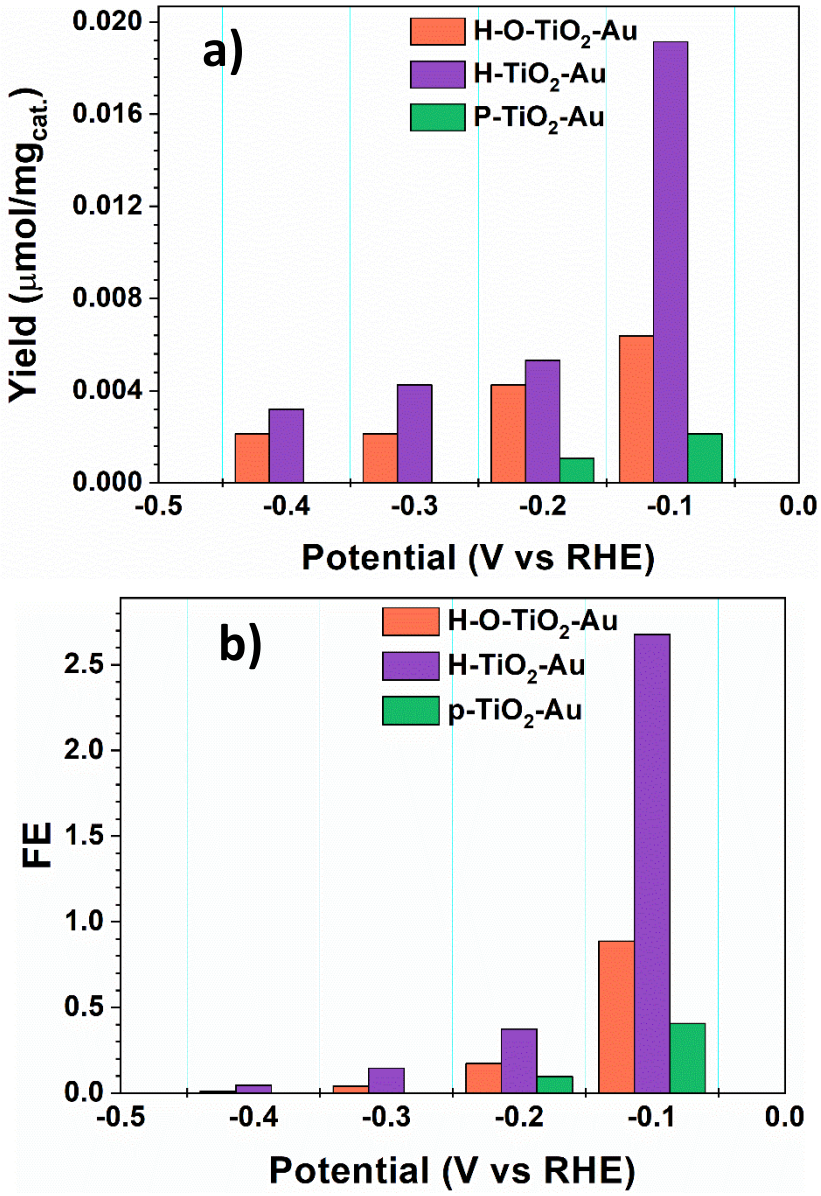

Figure 6-9 Electrocatalytic NRR of TiO_2-Au. (a) Yield rate of NH_3 with different catalysts at different potentials room temperature and ambient pressure; (b) Faradaic efficiency at each given potential.

Figure 6-9 (b) tells us the faradaic efficiency (FE) of the catalysts for NRR. The same results were obtained for these three catalysts, the highest FE of 2.7 % is obtained for H-TiO_2-Au at -0.1 V, while the H-O-TiO_2-Au just has a FE of about 0.9 % at -0.1V. For the original sample, P-TiO_2-Au only gave a faradaic efficiency of around 0.4 % for the electrochemical nitrogen reduction reactions. With the increasing of the reaction potential, the faradaic efficiencies

decreased quite fast for all the three samples. However, the plasma treated H-TiO_2-Au composite still give us better performances than the other two materials.

For practical application, the durability of the catalysts for improved nitrogen reduction reaction is critical. To determine the durability, chronoamperometric tests were conducted. Figure 6-10 shows the chronoamperometry results of the three samples at different potentials. When the potential is -0.1 and -0.2 V, we could find that the current of H-TiO_2-Au and H-O-TiO_2-Au are just slightly higher than the P-TiO_2-Au particles, while the H-O-TiO_2-Au displays the highest current density. What's more, all of the three samples shown a very good NRR stability for the duration of 3600 s because of the high stability of TiO_2. When the potentials come to -0.3 and -0.4 V, the differences between before and after plasma treated materials are more significantly. At these potentials, the materials with plasma treatment show quite similar current density, and both of them are much higher than the pristine materials. Then we could conclude that the hydrogen plasma treatment process improved the electrochemical performances of the TiO_2-Au nanoparticles a lot, the reaction current is considerable improved.

Therefore, there are almost no other productions except the NH_3 during the electrochemical reactions. In our present work, there is no N_2H_4 has been detected in the final products. It is quite similar with the work of D. Bao and co-workers[189]. They explained the mechanical of the NRR as an associative alternating pathway[202]: first, N_2 is much easier to be absorbed on the surface of gold particles because of the positive charge status, and the N_2-Au bond will be formed. Secondly, the active protons in the electrolyte will be active to form a N-H bond to break the N≡N triple bond. Finally, hydrogenation of the N_2 is carried out by adding H atoms one-by-one from the electrolyte and an electron from the electrode surface. The whole reaction process could be described in Figure 6-11.

In this case, NH_3 will be the major product of this reaction, and we could know that the TiO_2-Au catalyst has a great selectivity of producing NH_3 than other productions. According to the characterization results of TEM, UV-Vis, XPS and EPR, we are almost sure that the oxygen vacancies and disordered surface layer are existed after the hydrogen plasma treatment. And now we wonder how the oxygen defects could affect the performance of the sample as electrochemical reduction reactions catalyst. To further determine the NRR mechanism, density functional theory (DFT) was used to analyze the catalysts process[14,203]. The free energy changes(ΔG) and relative free energy of the elementary reactions are established in Figure 6-13. From Figure 6-13(a), for the first step, the N2 absorbed ΔG of the H-TiO2-Au is

lower than the P-TiO2-Au, it means the first step of the NRR reaction is easier to be processed for the H-TiO2-Au. Then, according to the calculation results (Figure 6-13 (b)), the formation of the -NNH intermediate is the rate-determining step of the whole NRR process，and the relative G of H-TiO2-Au is lower than P-TiO2-Au at this step, it makes the reaction to be preferred to happen. From this step on, all the step reactions of H-TiO2-Au are exothermic reactions, while the forth step of P-TiO2-Au (from -NHNHH+3/2*H2 to -NHHNHH+H2) is an endothermic reaction, it will need more energy to make this step to be processed. Figure 6-12 shows the structures of each reaction step on Au of the H-TiO_2-Au catalysts for NRR process. The hydriding pathway to produce NH_3 is clearly illustrated in the picture. Then the DFG calculation results tell us that the plasma treated materials with oxygen vacancies and disordered surface layer is proved to be a greater catalyst for the NRR process.

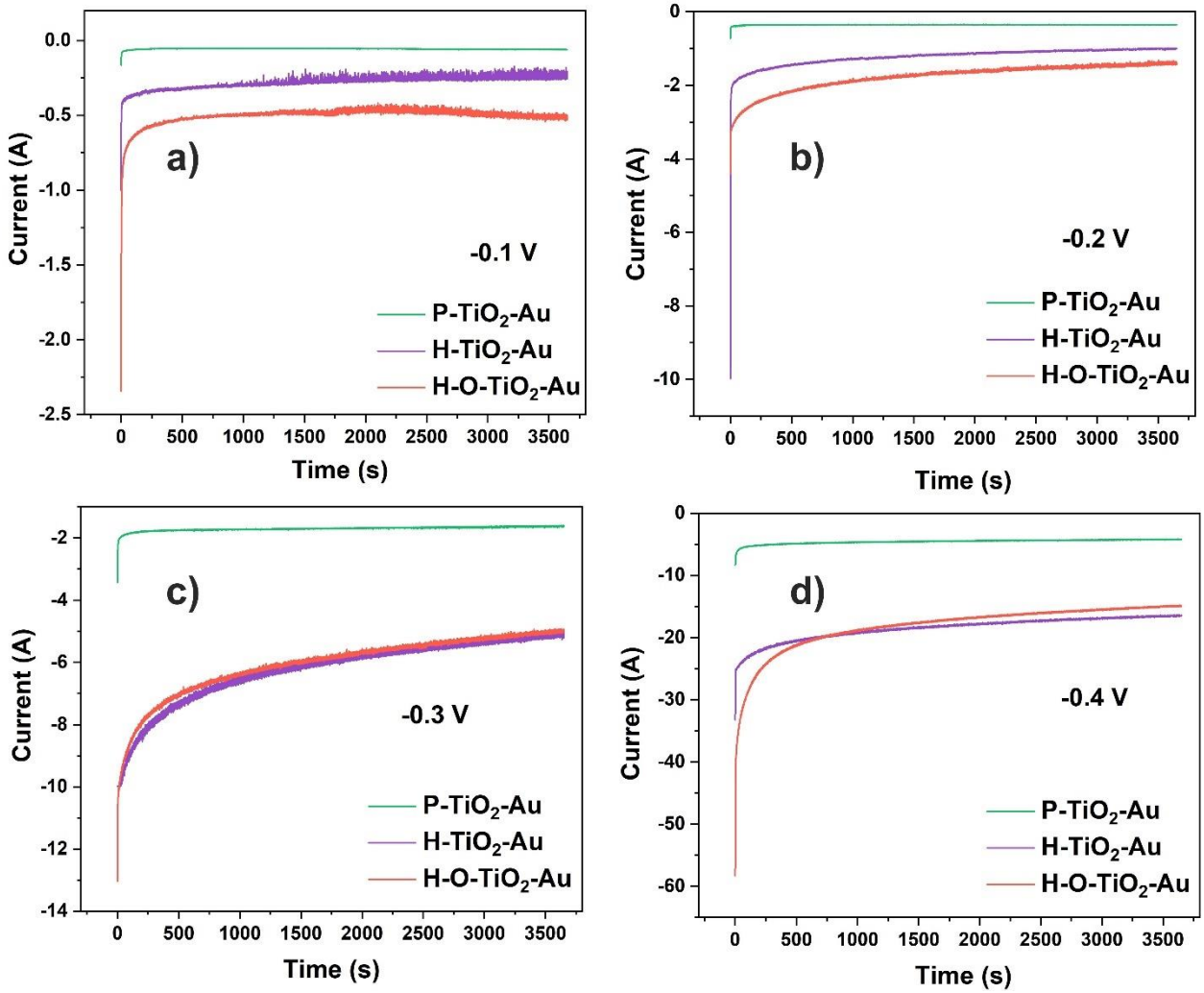

Figure 6-10 Chrono-amperometry results of the three samples at the corresponding potentials: (a)-0.1 V; (b) -0.2 V; (c)-0.3 V; (d) -0.4 V.

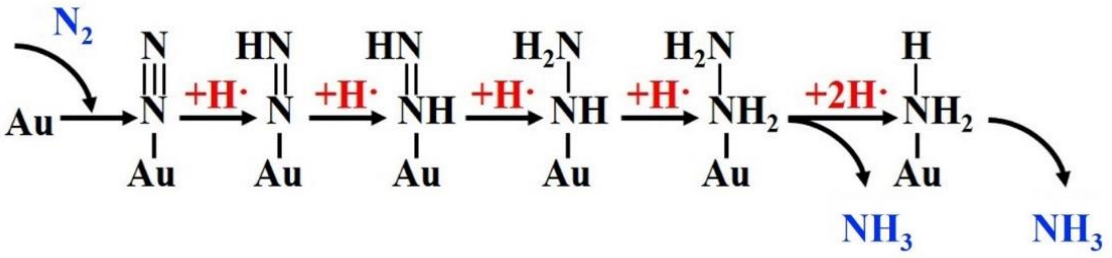

Figure 6-11 Hydriding pathway for NRR on Au catalysts at equilibrium potential.

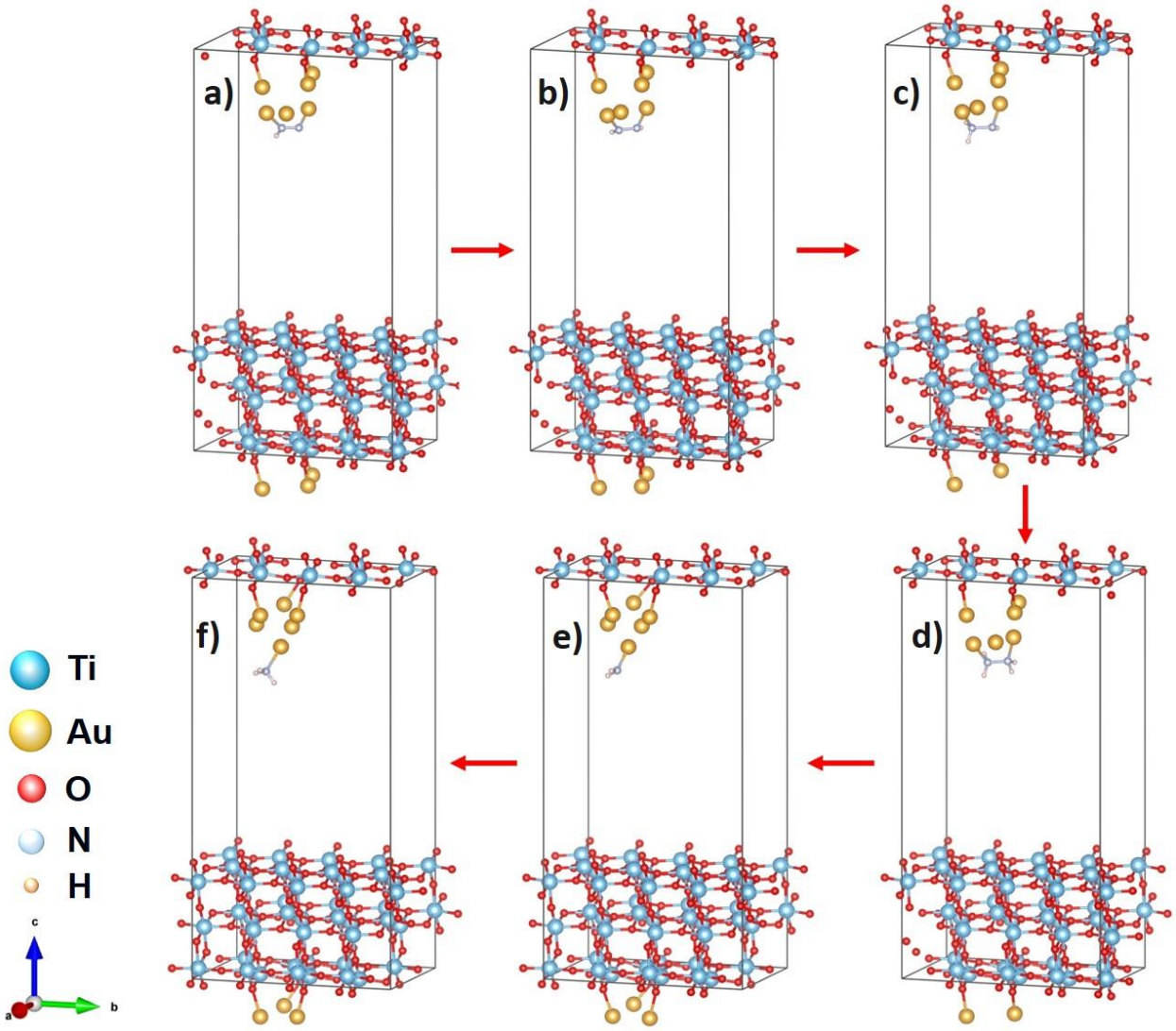

Figure 6-12 Illustration of structures on Au of the H-TiO_2-Au catalysts for NRR process. The 6 main intermediates shown the procedure of the NH_3 producing: (a)-NNH; (b)-NHNH; (c) -NHNHH; (d)-NHHNHH; (e)-NHH+NH_3; (f) NH_3.

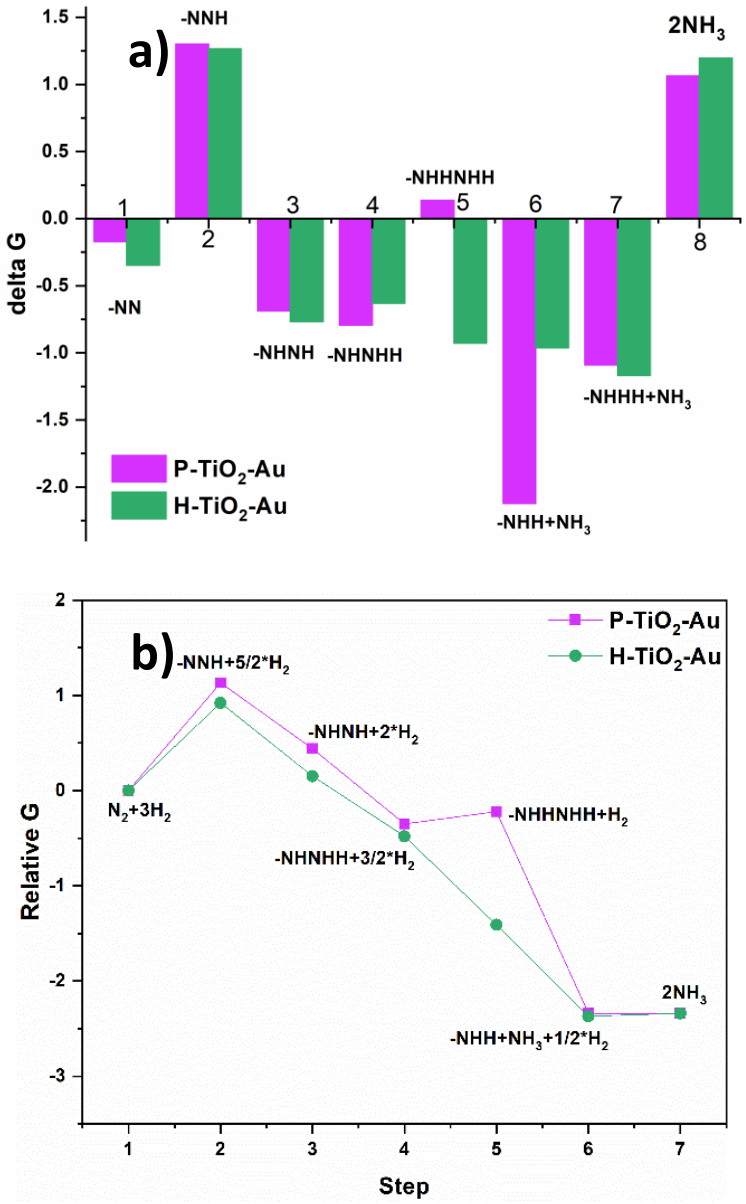

Figure 6-13 (a) Free energy changes of diagram and alternating hydriding pathway for NRR process of H-TiO_2-Au and P-TiO_2-Au; (b) Relative Free energy and alternating hydriding pathway for NRR process of H-TiO_2-Au and P-TiO_2-Au.

6.3 Conclusions

A hydrogenated blue-black TiO_2-Au (H-TiO_2-Au) composite is synthesized with an enhanced plasma treatment process. The plasma treated materials not only shown a very strong absorption in the UV range, but also the absorption in the whole visible region are stronger compared to the pristine TiO_2-Au sample. From the TEM investigations we could find some disordered positions on the surface, and also the Raman intensities of H-TiO_2-Au is much lower than the pristine material which could be attributed to the disordered surface and the oxygen vacancies formation. What's more, a small peak shift for the XPS could be found after the hydrogen plasma treatment. When the sample was used for the electrochemical nitrogen reduction reactions, the hydrogenated catalysts shown much better improved activities for the NH_3 production. And the yield of NH_3 of blue-black H-TiO_2-Au is around 9.5 times higher than the original sample, while the highest faradaic efficiency of 2.7 % is also obtain at the potential of -0.1V. The DFT calculation results confirms that the plasma treated material with oxygen vacancies and disordered surface layer is much preferred for the NRR process. The reduction process of H_2 plasma make an important role on the improving of catalysts' performances.

7. Summary and Perspective

In summary, different materials with different gases of plasma treatment modification methods for energy storage and conversion application were prepared and the electrochemical performance are tested. We used hydrogen and nitrogen as high-power plasma treatment gas, both of them created a disordered surface layer, which plays a significant role on enhancing the electrochemical performances of the materials. What's more, except metal oxides, we choose transition metal dichalcogenides (WS_2) for the plasma treatment process and it shown a promising improvement for anode materials of LIBs and SIBs as well. And not only for the single materials, we modified TiO_2-Au composite materials with hydrogen plasma, which resulted in a considerable improvement for the electrochemical catalysts performance of nitrogen reduction reaction.

Firstly, WS_2 nanoparticles are modified by H_2 plasma treatment, and the H-WS_2 shows a clearly improved rate performance compared with the pristine WS_2 when used as the anode materials for both lithium and sodium ion batteries. After the hydrogenated treatment, a disordered surface layer with a thickness about 2.5 nm is formed. The disordered surface could be investigated by the TEM, Raman and also the XPS results clearly. The H-WS_2 nanoparticles possess significantly higher specific capacity at different current densities. In addition, the electrochemical impedance spectroscopy (EIS) reveals a drastic decrease of the charge-transfer resistance for application in both LIBs and SIBs, which implies the plasma hydrogenated electrode material is more favorable for the electron transport during the lithium and sodium ion insertion/extraction process. We think after hydrogen plasma treatment, charge transfer of the electrode become easier and faster within the disordered surface than the crystalline phase. As a result, the larger capacity retention and longer lifetime of the electrode could be obtained. This is the main reason why we got a better performance for H-WS_2, and hydrogen plasma treatment could be identified as an effective method to reduce the resistance of the electrode with the disordered surface formation.

Secondly, N-TiO_2 nanoparticles have been synthesized via high power N_2 plasma treatment. Comparing with other synthesis methods, a disordered surface layer is formed in addition to the N doping after the treatment. Both disordered surface layer and N doping have a collective effect on the rate performance enhancement when used as the anode materials for sodium-ion batteries.

What's more, when the samples are tested for the anode materials of SIBs, the N-TiO_2 shows a great cycling stability. In addition, the electrochemical impedance spectroscopy (EIS) reveals a drastic decrease of the charge-transfer resistance from 137 Ω (pristine TiO_2) to about 50 Ω (N-TiO_2), which implies the plasma treatment for electrode material is more effective method for enhancing the electron transport during the sodium ion insertion/extraction process.

Thirdly, a hydrogenated blue-black TiO_2-Au composite is synthesized with an enhanced plasma treatment process. When the sample was used for the electrochemical nitrogen reduction reactions, the hydrogenated catalysts shown much better improved activities for the NH_3 production. And the yield of NH_3 of blue-black H-TiO_2-Au is around 9.5 times higher than the original sample, while the highest faradaic efficiency of 2.7 % is also obtain at the potential of -0.1V. From the TEM and the XPS results, we find some disordered surfaces were formed after the hydrogenation process, we could say that the reduction process of H_2 plasma make an important role on the improving of catalysts' performance.

Based on the present results, in the further research, the relation between disordered surface layer and the performance improvement haven't been investigated clearly enough, we should try more effective characterization methods, like nuclear magnetic resonance (NMR), and positron annihilation lifetime spectroscopy (PALS) to get more details about the differences before and after plasma treatment.

Secondly, we could focus on more different of materials which could be used for the plasma treatment process, and a deep understanding of microstructure and some other new applications could be tried as well. Firstly, various materials, like nanostructured Ni/TiO_2, NiO_2, and more composite materials could be tested with different plasma treatment. Secondly, different kinds of electrochemical applications could be tested as well, such as hydrogen evolution reaction (HER), oxygen evolution reaction (OER). What 's more, some photo-electrocatalyst performances could be tested as well, because the nanostructure and also plasma treatment could make the light absorption of materials improved a lot. We believe that the plasma treatment method holds great promise for prepare new energy storage materials.

References

[1] X. Zhang, X. Cheng, Q. Zhang, Nanostructured energy materials for electrochemical energy conversion and storage: A review, J. Energy Chem. 25 (2016) 967–984. doi:10.1016/j.jechem.2016.11.003.

[2] X. Chen, L. Liu, P.Y. Yu, S.S. Mao, Increasing Solar Absorption for Photocatalysis with Black Hydrogenated Titanium Dioxide Nanocrystals, Science (80). 331 (2011) 746–751.

[3] Y. Yan, M. Han, A. Konkin, T. Koppe, D. Wang, T. Andreu, G. Chen, U. Vetter, J.R. Morante, P. Schaaf, Slightly hydrogenated TiO_2 with enhanced photocatalytic performance, J. Mater. Chem. A. 2 (2014) 12708–12716. doi:10.1039/c4ta02192d.

[4] J.Y. Shin, J.H. Joo, D. Samuelis, J. Maier, Oxygen-deficient $TiO_{2-\delta}$ nanoparticles via hydrogen reduction for high rate capability lithium batteries, Chem. Mater. 24 (2012) 543–551. doi:10.1021/cm2031009.

[5] Z. Lu, C.T. Yip, L. Wang, H. Huang, L. Zhou, Hydrogenated TiO_2 nanotube arrays as high-rate anodes for lithium-ion microbatteries, Chempluschem. 77 (2012) 991–1000. doi:10.1002/cplu.201200104.

[6] T. Xia, C. Zhang, N.A. Oyler, X. Chen, Hydrogenated TiO_2 Nanocrystals: A novel microwave absorbing material, Adv. Mater. 25 (2013) 6905–6910. doi:10.1002/adma.201303088.

[7] T. Zhai, J. Gan, M. Yu, Y. Li, G. Wang, X. Lu, Y. Tong, Hydrogenated TiO_2 Nanotube Arrays for Supercapacitors , Nano Lett. 12 (2012) 1690–1696. doi:10.1021/nl300173j.

[8] W. Ren, Y. Yan, L. Zeng, Z. Shi, A. Gong, P. Schaaf, D. Wang, J. Zhao, B. Zou, H. Yu, G. Chen, E.M.B. Brown, A. Wu, A Near Infrared Light Triggered Hydrogenated Black TiO_2 for Cancer Photothermal Therapy, Adv. Healthc. Mater. 4 (2015) 1526–1536. doi:10.1002/adhm.201500273.

[9] T. Xia, W. Zhang, W. Li, N.A. Oyler, G. Liu, X. Chen, Hydrogenated surface disorder

enhances lithium ion battery performance, Nano Energy. 2 (2013) 826–835. doi:10.1016/j.nanoen.2013.02.005.

[10] L. Yu, L.P. Wang, H. Liao, J. Wang, Z. Feng, O. Lev, J.S.C. Loo, M.T. Sougrati, Z.J. Xu, Understanding Fundamentals and Reaction Mechanisms of Electrode Materials for Na-Ion Batteries, Small. 14 (2018) 1–22. doi:10.1002/smll.201703338.

[11] Y. Lu, L. Yu, X.W. (David) Lou, Nanostructured Conversion-type Anode Materials for Advanced Lithium-Ion Batteries, Chem. 4 (2018) 972–996. doi:10.1016/j.chempr.2018.01.003.

[12] K.A. Brown, D.F. Harris, M.B. Wilker, A. Rasmussen, N. Khadka, H. Hamby, S. Keable, G. Dukovic, J.W. Peters, L.C. Seefeldt, P.W. King, Light-driven dinitrogen reduction catalyzed by a CdS:nitrogenase MoFe protein biohybrid, Science (80). 352 (2016) 448–450. doi:10.1126/science.aaf2091.

[13] S. Licht, B. Cui, B. Wang, F.-F. Li, J. Lau, S. Liu, Ammonia Synthesis by N_2 and Steam Electrolysis in Molten Hydroxide Suspensions of Nanoscale Fe_2O_3, Science (80). 45 (2014) 637–640. doi:10.1002/chin.201443014.

[14] J.H. Montoya, C. Tsai, A. Vojvodic, J.K. Nørskov, The challenge of electrochemical ammonia synthesis: A new perspective on the role of nitrogen scaling relations, ChemSusChem. 8 (2015) 2180–2186. doi:10.1002/cssc.201500322.

[15] M. Stanley Whittingham, Lithium batteries and cathode materials, Chem. Rev. 104 (2004) 4271–4301. doi:10.1021/cr020731c.

[16] F. De Angelis, R. Proietti Zaccaria, E. Miele, S. Goriparti, C. Capiglia, E. Di Fabrizio, Review on recent progress of nanostructured anode materials for Li-ion batteries, J. Power Sources. 257 (2014) 421–443. doi:10.1016/j.jpowsour.2013.11.103.

[17] K. Xu, Nonaqueous Liquid Electrolytes for Lithium-Based Rechargeable Batteries, Chem. Rev. 104 (2004) 4303–4418. doi:10.1021/cr030203g.

[18] P. Lu, Y. Sun, H. Xiang, X. Liang, Y. Yu, 3D Amorphous Carbon with Controlled Porous and Disordered Structures as a High-Rate Anode Material for Sodium-Ion Batteries, Adv. Energy Mater. 8 (2018) 1–8. doi:10.1002/aenm.201702434.

[19] Y. Shao, B. Yi, J. Hou, M.W. Ellis, R.B. Moore, Graphene-based electrochemical

energy conversion and storage: fuel cells, supercapacitors and lithium ion batteries, Phys. Chem. Chem. Phys. 13 (2011) 15384. doi:10.1039/c1cp21915d.

[20] C.M. Schauerman, M.J. Ganter, G. Gaustad, C.W. Babbitt, R.P. Raffaelle, B.J. Landi, Recycling single-wall carbon nanotube anodes from lithium ion batteries, J. Mater. Chem. 22 (2012) 12008–12015. doi:10.1039/c2jm31971c.

[21] H. Fujimoto, K. Tokumitsu, A. Mabuchi, N. Chinnasamy, T. Kasuh, The anode performance of the hard carbon for the lithium ion battery derived from the oxygen-containing aromatic precursors, J. Power Sources. 195 (2010) 7452–7456. doi:10.1016/j.jpowsour.2010.05.041.

[22] B.Y. Guan, L. Yu, J. Li, X.W. Lou, A universal cooperative assembly-directed method for coating of mesoporous TiO_2 nanoshells with enhanced lithium storage properties, Sci. Adv. 2 (2016) 2–10. doi:10.1126/sciadv.1501554.

[23] L. Yu, H. Bin Wu, X.W. Lou, Mesoporous $Li_4Ti_5O_{12}$ hollow spheres with enhanced lithium storage capability, Adv. Mater. 25 (2013) 2296–2300. doi:10.1002/adma.201204912.

[24] G.N. Zhu, Y.G. Wang, Y.Y. Xia, Ti-based compounds as anode materials for Li-ion batteries, Energy Environ. Sci. 5 (2012) 6652–6667. doi:10.1039/c2ee03410g.

[25] W.J. Zhang, A review of the electrochemical performance of alloy anodes for lithium-ion batteries, J. Power Sources. 196 (2011) 13–24. doi:10.1016/j.jpowsour.2010.07.020.

[26] S. Martinet, Nanomaterials for rechargeable lithium batteries, Nanosci. Technol. (2016) 471–512. doi:10.1007/978-3-319-32023-6_13.

[27] D. Bresser, S. Passerini, B. Scrosati, Leveraging valuable synergies by combining alloying and conversion for lithium-ion anodes, Energy Environ. Sci. 9 (2016) 3348–3367. doi:10.1039/c6ee02346k.

[28] N.G. Rudawski, B.R. Yates, M.R. Holzworth, K.S. Jones, R.G. Elliman, A.A. Volinsky, Ion beam-mixed Ge electrodes for high capacity Li rechargeable batteries, J. Power Sources. 223 (2013) 336–340. doi:10.1016/j.jpowsour.2012.09.056.

[29] C.M. Park, J.H. Kim, H. Kim, H.J. Sohn, Li-alloy based anode materials for Li secondary batteries, Chem. Soc. Rev. 39 (2010) 3115–3141. doi:10.1039/b919877f.

[30] Z. Wang, L. Zhou, X.W. Lou, Metal oxide hollow nanostructures for lithium-ion batteries, Adv. Mater. 24 (2012) 1903–1911. doi:10.1002/adma.201200469.

[31] J. Yang, Y. Takeda, N. Imanishi, C. Capiglia, J.Y. Xie, O. Yamamoto, SiOx-based anodes for secondary lithium batteries, Solid State Ionics. 152–153 (2002) 125–129. doi:10.1016/S0167-2738(02)00362-4.

[32] Y.X. Yin, L.J. Wan, Y.G. Guo, Silicon-based nanomaterials for lithium-ion batteries, Chinese Sci. Bull. 57 (2012) 4104–4110. doi:10.1007/s11434-012-5017-2.

[33] Y. Li, X. Huang, X.W.D. Lou, J. Jiang, J. Liu, C. Yuan, Recent Advances in Metal Oxide-based Electrode Architecture Design for Electrochemical Energy Storage, Adv. Mater. 24 (2012) 5166–5180. doi:10.1002/adma.201202146.

[34] C.H. Lai, M.Y. Lu, L.J. Chen, Metal sulfide nanostructures: Synthesis, properties and applications in energy conversion and storage, J. Mater. Chem. 22 (2012) 19–30. doi:10.1039/c1jm13879k.

[35] C. Yuan, H. Bin Wu, Y. Xie, X.W. Lou, Mixed transition-metal oxides: Design, synthesis, and energy-related applications, Angew. Chemie - Int. Ed. 53 (2014) 1488–1504. doi:10.1002/anie.201303971.

[36] G. Yu-Guo, H. Jin-Song, W. Li-Jun, Nanostructured Materials for Electrochemical Energy Conversion and Storage Devices, Adv. Mater. 20 (2008) 2878–2887. doi:10.1002/adma.200800627.

[37] Z. Wen, K. Rui, J. Jin, Y. Lu, C. Shen, One-Step Solvothermal Synthesis of Nanostructured Manganese Fluoride as an Anode for Rechargeable Lithium-Ion Batteries and Insights into the Conversion Mechanism, Adv. Energy Mater. 5 (2014) 1401716. doi:10.1002/aenm.201401716.

[38] L. Ji, Z. Lin, M. Alcoutlabi, X. Zhang, Recent developments in nanostructured anode materials for rechargeable lithium-ion batteries, Energy Environ. Sci. 4 (2011) 2682–2689. doi:10.1039/c0ee00699h.

[39] Y. Xiao, J.Y. Hwang, I. Belharouak, Y.K. Sun, Superior Li/Na-storage capability of a carbon-free hierarchical CoSx hollow nanostructure, Nano Energy. 32 (2017) 320–328. doi:10.1016/j.nanoen.2016.12.053.

[40] K.A. Kwon, H.S. Lim, Y.K. Sun, K. Do Suh, α-Fe_2O_3 submicron spheres with hollow and macroporous structures as high-performance anode materials for lithium ion batteries, J. Phys. Chem. C. 118 (2014) 2897–2907. doi:10.1021/jp5000057.

[41] B. Dunn, H. Kamath, J. M. Tarascon, Electrical Energy Storage for the Grid: A Battery of Choices (Supporting Online Material), Science (80). 334 (2011) 928–935. doi:10.1126/science.1212741.

[42] Y. Sun, N. Liu, Y. Cui, Promises and challenges of nanomaterials for lithium-based rechargeable batteries, Nat. Energy. 1 (2016) 1–12. doi:10.1038/nenergy.2016.71.

[43] J. Yao, Y. Gong, S. Yang, P. Xiao, Y. Zhang, K. Keyshar, G. Ye, S. Ozden, R. Vajtai, P.M. Ajayan, $CoMoO_4$ nanoparticles anchored on reduced graphene oxide nanocomposites as anodes for long-life lithium-ion batteries, ACS Appl. Mater. Interfaces. 6 (2014) 20414–20422. doi:10.1021/am505983m.

[44] Y. luo, L. Mei, H. Zhang, T. Yang, T. Wang, Q. Li, D. Guo, Enhanced electrochemical performance of $CoMoO_4$ nanorods/reduced graphene oxide as anode material for lithium-ion batteries, Electrochim. Acta. 158 (2015) 327–332. doi:10.1016/j.electacta.2015.01.154.

[45] X. Cao, Z. Yin, H. Zhang, Three-dimensional graphene materials: Preparation, structures and application in supercapacitors, Energy Environ. Sci. 7 (2014) 1850–1865. doi:10.1039/c4ee00050a.

[46] Y. Zhao, X. Li, B. Yan, D. Xiong, D. Li, S. Lawes, X.L. Sun, Recent Developments and Understanding of Novel Mixed Transition-Metal Oxides as Anodes in Lithium Ion Batteries, Adv. Energy Mater. 6 (2016) 1–19. doi:10.1002/aenm.201502175.

[47] C. Zheng, C. Chen, L. Chen, M. Wei, A CMK-5-encapsulated $MoSe_2$ composite for rechargeable lithium-ion batteries with improved electrochemical performance, J. Mater. Chem. A. 5 (2017) 19632–19638. doi:10.1039/c7ta06286a.

[48] S. Liu, B. Shen, Y. Niu, M. Xu, Fabrication of WS_2-nanoflowers@rGO composite as an anode material for enhanced electrode performance in lithium-ion batteries, J. Colloid Interface Sci. 488 (2017) 20–25. doi:10.1016/j.jcis.2016.10.083.

[49] Y. Wang, D. Kong, W. Shi, B. Liu, G.J. Sim, Q. Ge, H.Y. Yang, Ice Templated Free-

Standing Hierarchically WS_2/CNT-rGO Aerogel for High-Performance Rechargeable Lithium and Sodium Ion Batteries, Adv. Energy Mater. 6 (2016) 1–9. doi:10.1002/aenm.201601057.

[50] Y. Du, X. Zhu, L. Si, Y. Li, X. Zhou, J. Bao, Improving the anode performance of WS_2 through a self-assembled double carbon coating, J. Phys. Chem. C. 119 (2015) 15874–15881. doi:10.1021/acs.jpcc.5b03540.

[51] L. Zhang, H. Bin Wu, Y. Yan, X. Wang, X.W. Lou, Hierarchical MoS_2 microboxes constructed by nanosheets with enhanced electrochemical properties for lithium storage and water splitting, Energy Environ. Sci. 7 (2014) 3302–3306. doi:10.1039/c4ee01932f.

[52] W. Sun, P. Li, X. Liu, J. Shi, H. Sun, Z. Tao, F. Li, J. Chen, Size-controlled MoS_2 nanodots supported on reduced graphene oxide for hydrogen evolution reaction and sodium-ion batteries, Nano Res. 10 (2017) 2210–2222. doi:10.1007/s12274-016-1410-5.

[53] L. Zhou, S. Yan, L. Pan, X. Wang, Y. Wang, Y. Shi, A scalable sulfuration of WS_2 to improve cyclability and capability of lithium-ion batteries, Nano Res. 9 (2016) 857–865. doi:10.1007/s12274-015-0966-9.

[54] L. Pan, Huilin, Hu, Yong Sheng, Chen, Room-temperature stationary sodium-ion batteries for large-scale electric energy storage, Energy Environ. Sci. 6 (2013) 2338–2360. doi:10.1039/c3ee40847g.

[55] J.Y. Hwang, S.T. Myung, Y.K. Sun, Sodium-ion batteries: Present and future, Chem. Soc. Rev. 46 (2017) 3485–3856. doi:10.1039/c6cs00776g.

[56] V. Palomares, P. Serras, I. Villaluenga, K.B. Hueso, J. Carretero-González, T. Rojo, Na-ion batteries, recent advances and present challenges to become low cost energy storage systems, Energy Environ. Sci. 5 (2012) 5884–5901. doi:10.1039/c2ee02781j.

[57] Y.E. Zhu, L. Yang, J. Sheng, Y. Chen, H. Gu, J. Wei, Z. Zhou, Fast Sodium Storage in TiO_2@CNT@C Nanorods for High-Performance Na-Ion Capacitors, Adv. Energy Mater. 7 (2017) 1–9. doi:10.1002/aenm.201701222.

[58] Y. Zhang, C.W. Foster, C.E. Banks, L. Shao, H. Hou, G. Zou, J. Chen, Z. Huang, X. Ji, Graphene-Rich Wrapped Petal-Like Rutile TiO_2 tuned by Carbon Dots for High-

Performance Sodium Storage, Adv. Mater. 28 (2016) 9391–9399. doi:10.1002/adma.201601621.

[59] S. Guo, J. Yi, Y. Sun, H. Zhou, Recent advances in titanium-based electrode materials for stationary sodium-ion batteries, Energy Environ. Sci. 9 (2016) 2978–3006. doi:10.1039/c6ee01807f.

[60] L. Wu, D. Buchholz, D. Bresser, L. Gomes Chagas, S. Passerini, Anatase TiO_2 nanoparticles for high power sodium-ion anodes, J. Power Sources. 251 (2014) 379–385. doi:10.1016/J.JPOWSOUR.2013.11.083.

[61] H. Xiong, M.D. Slater, M. Balasubramanian, C.S. Johnson, T. Rajh, Amorphous TiO_2 Nanotube anode for rechargeable sodium ion batteries, J. Phys. Chem. Lett. 2 (2011) 2560–2565. doi:10.1021/jz2012066.

[62] Y. Zhang, V. Srot, I. Moudrakovski, Y. Feng, P.A. van Aken, J. Maier, Y. Yu, Boosting Sodium Storage in TiF_3/Carbon Core/Sheath Nanofibers through an Efficient Mixed-Conducting Network, Adv. Energy Mater. 1901470 (2019) 1–9. doi:10.1002/aenm.201901470.

[63] Y. Zhang, C.W. Foster, C.E. Banks, L. Shao, H. Hou, G. Zou, J. Chen, Z. Huang, X. Ji, Graphene-Rich Wrapped Petal-Like Rutile TiO_2 tuned by Carbon Dots for High-Performance Sodium Storage, Adv. Mater. 28 (2016) 9391–9399. doi:10.1002/adma.201601621.

[64] K.T. Kim, G. Ali, K.Y. Chung, C.S. Yoon, H. Yashiro, Y.K. Sun, J. Lu, K. Amine, S.T. Myung, Anatase titania nanorods as an intercalation anode material for rechargeable sodium batteries, Nano Lett. 14 (2014) 416–422. doi:10.1021/nl402747x.

[65] Q. Zhao, R. Bi, J. Cui, X. Yang, L. Zhang, TiO_{2-x} Nanocages Anchored in N-Doped Carbon Fiber Films as a Flexible Anode for High-Energy Sodium-Ion Batteries, ACS Appl. Energy Mater. 1 (2018) 4459–4466. doi:10.1021/acsaem.8b00985.

[66] H. He, Q. Gan, H. Wang, G.L. Xu, X. Zhang, D. Huang, F. Fu, Y. Tang, K. Amine, M. Shao, Structure-dependent performance of TiO_2/C as anode material for Na-ion batteries, Nano Energy. 44 (2018) 217–227. doi:10.1016/j.nanoen.2017.11.077.

[67] Y. Yang, X. Ji, M. Jing, H. Hou, Y. Zhu, L. Fang, X. Yang, Q. Chen, C.E. Banks, Carbon

dots supported upon N-doped TiO_2 nanorods applied into sodium and lithium ion batteries, J. Mater. Chem. A. 3 (2015) 5648–5655. doi:10.1039/c4ta05611f.

[68] Y. Zhang, C. Wang, H. Hou, G. Zou, X. Ji, Nitrogen Doped/Carbon Tuning Yolk-Like TiO_2 and Its Remarkable Impact on Sodium Storage Performances, Adv. Energy Mater. 7 (2017). doi:10.1002/aenm.201600173.

[69] H.A. Cha, H.M. Jeong, J.K. Kang, Nitrogen-doped open pore channeled graphene facilitating electrochemical performance of TiO_2 nanoparticles as an anode material for sodium ion batteries, J. Mater. Chem. A. 2 (2014) 5182–5186. doi:10.1039/c4ta00041b.

[70] J. Wang, G. Liu, K. Fan, D. Zhao, B. Liu, J. Jiang, D. Qian, C. Yang, J. Li, N-doped carbon coated anatase TiO_2 nanoparticles as superior Na-ion battery anodes, J. Colloid Interface Sci. 517 (2018) 134–143. doi:10.1016/J.JCIS.2018.02.001.

[71] Y. Yeo, J.W. Jung, K. Park, I.D. Kim, Graphene-wrapped anatase TiO_2 nanofibers as high-rate and long-cycle-life anode material for sodium ion batteries, Sci. Rep. 5 (2015) 1–9. doi:10.1038/srep13862.

[72] Y. Wu, X. Liu, Z. Yang, L. Gu, Y. Yu, Nitrogen-Doped Ordered Mesoporous Anatase TiO_2 Nanofibers as Anode Materials for High Performance Sodium-Ion Batteries, Small. 12 (2016) 3522–3529. doi:10.1002/smll.201600606.

[73] J. Ni, S. Fu, C. Wu, J. Maier, Y. Yu, L. Li, Self-Supported Nanotube Arrays of Sulfur-Doped TiO_2 Enabling Ultrastable and Robust Sodium Storage, Adv. Mater. 28 (2016) 2259–2265. doi:10.1002/adma.201504412.

[74] H. He, H. Wang, D. Sun, M. Shao, X. Huang, Y. Tang, N-doped rutile TiO_2/C with significantly enhanced Na storage capacity for Na-ion batteries, Electrochim. Acta. 236 (2017) 43–52. doi:10.1016/J.ELECTACTA.2017.03.104.

[75] D. Yan, C. Yu, X. Zhang, J. Li, J. Li, T. Lu, L. Pan, Enhanced electrochemical performances of anatase TiO_2 nanotubes by synergetic doping of Ni and N for sodium-ion batteries, Electrochim. Acta. 254 (2017) 130–139. doi:10.1016/j.electacta.2017.09.120.

[76] S. Liu, Z. Cai, J. Zhou, A. Pan, S. Liang, Nitrogen-doped TiO_2 nanospheres for advanced sodium-ion battery and sodium-ion capacitor applications, J. Mater. Chem. A. 4 (2016)

18278–18283. doi:10.1039/c6ta08472a.

[77] Y. Zhang, C. Wang, H. Hou, G. Zou, X. Ji, Nitrogen Doped/Carbon Tuning Yolk-Like TiO_2 and Its Remarkable Impact on Sodium Storage Performances, Adv. Energy Mater. 7 (2017) 1600173. doi:10.1002/aenm.201600173.

[78] Y. Lu, Y. Yang, T. Zhang, Z. Ge, H. Chang, P. Xiao, Y. Xie, L. Hua, Q. Li, H. Li, B. Ma, N. Guan, Y. Ma, Y. Chen, Photoprompted Hot Electrons from Bulk Cross-Linked Graphene Materials and Their Efficient Catalysis for Atmospheric Ammonia Synthesis, ACS Nano. 10 (2016) 10507–10515. doi:10.1021/acsnano.6b06472.

[79] K. Honkala, A. Hellman, I.N. Remediakis, A. Logadottir, A. Carlsson, S. Dahl, C.H. Christensen, J.K. Nørskov, Ammonia Synthesis from First-Principles Calculations, Science (80-.). 4963 (2005) 555–559.

[80] M.M. Rodriguez, E. Bill, W.W. Brennessel, P.L. Holland, N_2 Reduction and Hydrogenation to Ammonia by a Molecular Iron-Potassium Complex, Science (80). 334 (2014) 780–783.

[81] A. Hellman, E.J. Baerends, M. Biczysko, T. Bligaard, C.H. Christensen, D.C. Clary, S. Dahl, R. Van Harrevelt, K. Honkala, H. Jonsson, G.J. Kroes, M. Luppi, U. Manthe, J.K. Nørskov, R.A. Olsen, J. Rossmeisl, E. Skúlason, C.S. Tautermann, A.J.C. Varandas, J.K. Vincent, Predicting catalysis: Understanding ammonia synthesis from first-principles calculations, J. Phys. Chem. B. 110 (2006) 17719–17735. doi:10.1021/jp056982h.

[82] H. Broda, F. Tuczek, Catalytic ammonia synthesis in homogeneous solution - Biomimetic at last?, Angew. Chemie - Int. Ed. 53 (2014) 632–634. doi:10.1002/anie.201308780.

[83] R. Schlögl, Catalytic synthesis of ammonia - A “never-ending story”?, Angew. Chemie - Int. Ed. 42 (2003) 2004–2008. doi:10.1002/anie.200301553.

[84] T. Oshikiri, K. Ueno, H. Misawa, Selective Dinitrogen Conversion to Ammonia Using Water and Visible Light through Plasmon-induced Charge Separation, Angew. Chemie - Int. Ed. 55 (2016) 3942–3946. doi:10.1002/anie.201511189.

[85] V. Kordali, G. Kyriacou, C. Lambrou, Electrochemical synthesis of ammonia at atmospheric pressure and low temperature in a solid polymer electrolyte cell, Chem.

Commun. (2000) 1673–1674. doi:10.1039/b004885m.

[86] S. Giddey, S.P.S. Badwal, A. Kulkarni, Review of electrochemical ammonia production technologies and materials, Int. J. Hydrogen Energy. 38 (2013) 14576–14594. doi:10.1016/j.ijhydene.2013.09.054.

[87] N. Cherkasov, A.O. Ibhadon, P. Fitzpatrick, A review of the existing and alternative methods for greener nitrogen fixation, Chem. Eng. Process. Process Intensif. 90 (2015) 24–33. doi:10.1016/j.cep.2015.02.004.

[88] T.M. Pappenfus, K. Lee, L.M. Thoma, C.R. Dukart, Wind to Ammonia: Electrochemical Processes in Room Temperature Ionic Liquids, 16 (2009) 89–93. doi:10.1149/1.3159311.

[89] Y. Lu, J. Li, T. Tada, Y. Toda, S. Ueda, T. Yokoyama, M. Kitano, H. Hosono, Water Durable Electride Y5Si3: Electronic Structure and Catalytic Activity for Ammonia Synthesis, J. Am. Chem. Soc. 138 (2016) 3970–3973. doi:10.1021/jacs.6b00124.

[90] T. Lipman, 3 , Nihar Shah, Ammonia as an Alternative Energy Storage Medium for Hydrogen Fuel Cells: Scientific and Technical Review for Near-Term Stationary Power Demonstration Projects, Final Report Tim, 2007.

[91] J. Han, X. Ji, X. Ren, G. Cui, L. Li, F. Xie, H. Wang, B. Li, X. Sun, MoO_3 nanosheets for efficient electrocatalytic N_2 fixation to NH_3, J. Mater. Chem. A. 6 (2018) 12974–12977. doi:10.1039/C8TA03974G.

[92] S. Chen, S. Perathoner, C. Ampelli, C. Mebrahtu, D. Su, G. Centi, Electrocatalytic Synthesis of Ammonia at Room Temperature and Atmospheric Pressure from Water and Nitrogen on a Carbon-Nanotube-Based Electrocatalyst, Angew. Chemie - Int. Ed. 56 (2017) 2699–2703. doi:10.1002/anie.201609533.

[93] C. Lv, C. Yan, G. Chen, Y. Ding, J. Sun, Y. Zhou, G. Yu, An Amorphous Noble-Metal-Free Electrocatalyst that Enables Nitrogen Fixation under Ambient Conditions, Angew. Chemie - Int. Ed. 57 (2018) 6073–6076. doi:10.1002/anie.201801538.

[94] M.M. Shi, D. Bao, B.R. Wulan, Y.H. Li, Y.F. Zhang, J.M. Yan, Q. Jiang, Au Sub-Nanoclusters on TiO_2 toward Highly Efficient and Selective Electrocatalyst for N_2 Conversion to NH_3 at Ambient Conditions, Adv. Mater. 29 (2017).

doi:10.1002/adma.201606550.

[95] H.M. Liu, S.H. Han, Y. Zhao, Y.Y. Zhu, X.L. Tian, J.H. Zeng, J.X. Jiang, B.Y. Xia, Y. Chen, Surfactant-free atomically ultrathin rhodium nanosheet nanoassemblies for efficient nitrogen electroreduction, J. Mater. Chem. A. 6 (2018) 3211–3217. doi:10.1039/c7ta10866d.

[96] C. Guo, J. Ran, A. Vasileff, S.Z. Qiao, Rational design of electrocatalysts and photo(electro)catalysts for nitrogen reduction to ammonia (NH_3) under ambient conditions, Energy Environ. Sci. 11 (2018) 45–56. doi:10.1039/c7ee02220d.

[97] V. Kyriakou, I. Garagounis, E. Vasileiou, A. Vourros, M. Stoukides, Progress in the Electrochemical Synthesis of Ammonia, Catal. Today. 286 (2017) 2–13. doi:10.1016/j.cattod.2016.06.014.

[98] D. Bao, Q. Zhang, F.L. Meng, H.X. Zhong, M.M. Shi, Y. Zhang, J.M. Yan, Q. Jiang, X.B. Zhang, Electrochemical Reduction of N_2 under Ambient Conditions for Artificial N_2 Fixation and Renewable Energy Storage Using N_2/NH_3 Cycle, Adv. Mater. 29 (2017). doi:10.1002/adma.201604799.

[99] Z. Zheng, B. Huang, J. Lu, Z. Wang, X. Qin, X. Zhang, Y. Dai, M.H. Whangbo, Hydrogenated titania: Synergy of surface modification and morphology improvement for enhanced photocatalytic activity, Chem. Commun. 48 (2012) 5733–5735. doi:10.1039/c2cc32220j.

[100] Z. Wang, C. Yang, T. Lin, H. Yin, P. Chen, D. Wan, F. Xu, F. Huang, J. Lin, X. Xie, M. Jiang, Visible-light photocatalytic, solar thermal and photoelectrochemical properties of aluminium-reduced black titania, Energy Environ. Sci. 6 (2013) 3007–3014. doi:10.1039/c3ee41817k.

[101] A. Naldoni, M. Allieta, S. Santangelo, M. Marelli, F. Fabbri, S. Cappelli, C.L. Bianchi, R. Psaro, V. Dal Santo, Effect of nature and location of defects on bandgap narrowing in black TiO_2 nanoparticles, J. Am. Chem. Soc. 134 (2012) 7600–7603. doi:10.1021/ja3012676.

[102] W. Zhou, W. Li, J.Q. Wang, Y. Qu, Y. Yang, Y. Xie, K. Zhang, L. Wang, H. Fu, D. Zhao, Ordered mesoporous black TiO_2 as highly efficient hydrogen evolution photocatalyst, J. Am. Chem. Soc. 136 (2014) 9280–9283. doi:10.1021/ja504802q.

[103] Y. Yan, B. Hao, D. Wang, G. Chen, E. Markweg, A. Albrecht, P. Schaaf, Understanding the fast lithium storage performance of hydrogenated TiO_2 nanoparticles, J. Mater. Chem. A. 1 (2013) 14507–14513. doi:10.1039/c3ta13491a.

[104] C. Wu, Y. Xie, Promising vanadium oxide and hydroxide nanostructures: From energy storage to energy saving, Energy Environ. Sci. 3 (2010) 1191–1206. doi:10.1039/c0ee00026d.

[105] S. Li, H. Zhou, B. Han, F. Deng, X. Liu, L. Xiao, J. Fan, Hydrogenated mesoporous TiO_2-SiO_2 with increased moderate strong Brönsted acidic sites for Friedel-Crafts alkylation reaction, Catal. Sci. Technol. 2 (2012) 719–721. doi:10.1039/c2cy00510g.

[106] Ç. Kiliç, A. Zunger, N-type doping of oxides by hydrogen, Appl. Phys. Lett. 81 (2002) 73–75. doi:10.1063/1.1482783.

[107] Y. Yan, X. Cheng, W. Zhang, G. Chen, H. Li, A. Konkin, Z. Sun, S. Sun, D. Wang, P. Schaaf, Plasma Hydrogenated TiO_2/Nickel Foam as an Efficient Bifunctional Electrocatalyst for Overall Water Splitting, ACS Sustain. Chem. Eng. 7 (2018) acssuschemeng.8b04496. doi:10.1021/acssuschemeng.8b04496.

[108] Y. Yan, M. Han, A. Konkin, T. Koppe, D. Wang, T. Andreu, G. Chen, U. Vetter, J.R. Morante, P. Schaaf, Slightly hydrogenated TiO_2 with enhanced photocatalytic performance, J. Mater. Chem. A. 2 (2014) 12708–12716. doi:10.1039/c4ta02192d.

[109] J. Qiu, J. Dawood, S. Zhang, Hydrogenation of nanostructured semiconductors for energy conversion and storage, Chinese Sci. Bull. 59 (2014) 2144–2161. doi:10.1007/s11434-014-0186-9.

[110] T. Xia, W. Zhang, W. Li, N.A. Oyler, G. Liu, X. Chen, Hydrogenated surface disorder enhances lithium ion battery performance, Nano Energy. 2 (2013) 826–835. doi:10.1016/j.nanoen.2013.02.005.

[111] S.Y. Myonga, K.S. Lim, Highly stable and textured hydrogenated ZnO thin films, Appl. Phys. Lett. 82 (2003) 3026–3028. doi:10.1063/1.1571651.

[112] Van De Walle CG, Hydrogen as a cause of doping in zinc oxide, Phys. Rev. Lett. 85 (2000) 1012–5. doi:10.1103/PhysRevLett.85.1012.

[113] Y. Yan, B. Hao, D. Wang, G. Chen, E. Markweg, A. Albrecht, P. Schaaf, Understanding

the fast lithium storage performance of hydrogenated TiO_2 nanoparticles, J. Mater. Chem. A. 1 (2013) 14507–14513. doi:10.1039/c3ta13491a.

[114] J. Maier, Nanoionics: ion transport and electrochemical storage in confined systems, Nat. Mater. 4 (2005) 805–815. doi:10.1038/nmat1513.

[115] M.A. and J.-M. Tarascon, Building better batteries, Nature. 451 (2008) 2–7. doi:10.1038/451652a.

[116] J. Chen, F. Cheng, Combination of Lightweight Elements and Nanostructured Materials for Batteries723 ACCOUNTS OF CHEMICAL RESEARCH 713, 42 (2009) 50. doi:10.1021/ar800229g.

[117] A.S. ARICÒ1, B. BRUCE, PETERSCROSATI3, J.-M. TARASCON, AND, W. VAN SCHALKWIJK, Nanostructured materials for advanced energy conversion and storage devices, Nat. Mater. 59 (2005) 366–377. doi:10.1016/S0025-6196(12)62414-8.

[118] B. Dunn, H. Kamath, J. Tarascon, Electrical Energy Storage for the Grid : A Battery of Choices, Science (80). 334 (2011) 928. doi:10.1126/science.1212741.

[119] N.S. Choi, Z. Chen, S.A. Freunberger, X. Ji, Y.K. Sun, K. Amine, G. Yushin, L.F. Nazar, J. Cho, P.G. Bruce, Challenges facing lithium batteries and electrical double-layer capacitors, Angew. Chemie - Int. Ed. 51 (2012) 9994–10024. doi:10.1002/anie.201201429.

[120] N. Yabuuchi, K. Kubota, M. Dahbi, S. Komaba, Research development on sodium-ion batteries, Chem. Rev. 114 (2014) 11636–11682. doi:10.1021/cr500192f.

[121] S.W. Kim, D.H. Seo, X. Ma, G. Ceder, K. Kang, Electrode materials for rechargeable sodium-ion batteries: Potential alternatives to current lithium-ion batteries, Adv. Energy Mater. 2 (2012) 710–721. doi:10.1002/aenm.201200026.

[122] C. Zhu, P. Kopold, W. Li, P.A. Van Aken, J. Maier, Y. Yu, Engineering nanostructured electrode materials for high performance sodium ion batteries: A case study of a 3D porous interconnected WS_2/C nanocomposite, J. Mater. Chem. A. 3 (2015) 20487–20493. doi:10.1039/c5ta05758b.

[123] Y. Xu, Y. Zhu, Y. Liu, C. Wang, Electrochemical performance of porous carbon/tin composite anodes for sodium-ion and lithium-ion batteries, Adv. Energy Mater. 3 (2013)

128–133. doi:10.1002/aenm.201200346.

[124] Y. Li, Z. Yang, S. Xu, L. Mu, L. Gu, Y.S. Hu, H. Li, L. Chen, Air-Stable Copper-Based P_2-$Na_{7/9}Cu_{2/9}Fe_{1/9}Mn_{2/3}O_2$ as a New Positive Electrode Material for Sodium-Ion Batteries, Adv. Sci. 2 (2015) 1–7. doi:10.1002/advs.201500031.

[125] S. Komaba, N. Yabuuchi, T. Nakayama, A. Ogata, T. Ishikawa, I. Nakai, Study on the reversible electrode reaction of $Na_{1-x}Ni_{0.5}Mn_{0.5}O_2$ for a rechargeable sodium-ion battery, Inorg. Chem. 51 (2012) 6211–6220. doi:10.1021/ic300357d.

[126] J. Xu, M. Wang, N.P. Wickramaratne, M. Jaroniec, S. Dou, L. Dai, High-performance sodium ion batteries based on a 3D anode from nitrogen-doped graphene foams, Adv. Mater. 27 (2015) 2042–2048. doi:10.1002/adma.201405370.

[127] Y. Liu, N. Zhang, L. Jiao, Z. Tao, J. Chen, Ultrasmall Sn nanoparticles embedded in carbon as high-performance anode for sodium-ion batteries, Adv. Funct. Mater. 25 (2015) 214–220. doi:10.1002/adfm.201402943.

[128] X. Xu, W. Liu, Y. Kim, J. Cho, Nanostructured transition metal sulfides for lithium ion batteries: Progress and challenges, Nano Today. 9 (2014) 604–630. doi:10.1016/j.nantod.2014.09.005.

[129] R. Chen, T. Zhao, W. Wu, F. Wu, L. Li, J. Qian, R. Xu, H. Wu, H.M. Albishri, A.S. Al-Bogami, D.A. El-Hady, J. Lu, K. Amine, Free-standing hierarchically sandwich-type tungsten disulfide nanotubes/graphene anode for lithium-ion batteries, Nano Lett. 14 (2014) 5899–5904. doi:10.1021/nl502848z.

[130] D. Chen, G. Ji, B. Ding, Y. Ma, B. Qu, W. Chen, J.Y. Lee, Double transition-metal chalcogenide as a high-performance lithium-ion battery anode material, Ind. Eng. Chem. Res. 53 (2014) 17901–17908. doi:10.1021/ie503759v.

[131] Y. Liu, W. Wang, Y. Wang, X. Peng, Homogeneously assembling like-charged WS_2 and GO nanosheets lamellar composite films by filtration for highly efficient lithium ion batteries, Nano Energy. 7 (2014) 25–32. doi:10.1016/j.nanoen.2014.04.018.

[132] C. Liu, F. Li, M. Lai-Peng, H.M. Cheng, Advanced materials for energy storage, Adv. Mater. 22 (2010) 28–62. doi:10.1002/adma.200903328.

[133] H. Liu, D. Su, G. Wang, S.Z. Qiao, An ordered mesoporous WS_2 anode material with

superior electrochemical performance for lithium ion batteries, J. Mater. Chem. 22 (2012) 17437–17440. doi:10.1039/c2jm33992g.

[134] M. V. Reddy, G. V. Subba Rao, B.V.R. Chowdari, Metal Oxides and Oxysalts as Anode Materials for Li Ion Batteries, Chem. Rev. 113 (2013) 5364–5457. doi:10.1021/cr3001884.

[135] X. Xu, C.S. Rout, J. Yang, R. Cao, P. Oh, H.S. Shin, J. Cho, Freeze-dried WS_2 composites with low content of graphene as high-rate lithium storage materials, J. Mater. Chem. A. 1 (2013) 14548–14554. doi:10.1039/c3ta13329j.

[136] T.T. Debela, Y.R. Lim, H.W. Seo, I.S. Kwon, I.H. Kwak, J. Park, W. Il Cho, H.S. Kang, Two-Dimensional WS_2@Nitrogen-Doped Graphite for High-Performance Lithium Ion Batteries: Experiments and Molecular Dynamics Simulations, ACS Appl. Mater. Interfaces. 10 (2018) 37928–37936. doi:10.1021/acsami.8b10133.

[137] J. Ren, Z. Wang, F. Yang, R.P. Ren, Y.K. Lv, Freestanding 3D single-wall carbon nanotubes/WS_2 nanosheets foams as ultra-long-life anodes for rechargeable lithium ion batteries, Electrochim. Acta. 267 (2018) 133–140. doi:10.1016/j.electacta.2018.01.167.

[138] X. Li, J. Zhang, Z. Liu, C. Fu, C. Niu, WS_2 nanoflowers on carbon nanotube vines with enhanced electrochemical performances for lithium and sodium-ion batteries, J. Alloys Compd. 766 (2018) 656–662. doi:10.1016/j.jallcom.2018.07.008.

[139] A. Ambrosi, Z. Sofer, M. Pumera, 2H→1T phase transition and hydrogen evolution activity of MoS_2, $MoSe_2$, WS_2 and WSe_2 strongly depends on the MX_2 composition, Chem. Commun. 51 (2015) 8450–8453. doi:10.1039/c5cc00803d.

[140] H. Li, Q. Zhang, C.C.R. Yap, B.K. Tay, T.H.T. Edwin, A. Olivier, D. Baillargeat, From bulk to monolayer MoS_2: Evolution of Raman scattering, Adv. Funct. Mater. 22 (2012) 1385–1390. doi:10.1002/adfm.201102111.

[141] A.G. Bagnall, W.Y. Liang, E.A. Marseglia, B. Welber, Raman studies of MoS_2 at high pressure, Phys. B+C. 99 (1980) 343–346. doi:10.1016/0378-4363(80)90257-0.

[142] C. Lee, H. Yan, L.E. Brus, T.F. Heinz, Ḱ.J. Hone, S. Ryu, Anomalous Lattice Vibrations of Single- and Few-Layer MoS_2, ACS Nano. 4 (2010) 2695–2700. doi:10.1021/nn1003937.

[143] T. Xia, W. Zhang, J. Murowchick, G. Liu, X. Chen, Built-in Electric Field-Assisted Surface-Amorphized Nanocrystals for High-Rate Lithium-Ion Battery, (2013).

[144] T. Xia, W. Zhang, J.B. Murowchick, G. Liu, X. Chen, A facile method to improve the photocatalytic and lithium-ion rechargeable battery performance of TiO_2 nanocrystals, Adv. Energy Mater. 3 (2013) 1516–1523. doi:10.1002/aenm.201300294.

[145] R. Sandrock, M. Baumeister, Synthesis and Transfer of Large-Area Toward the Recyclable Use of Sapphire Monolayer WS_2 Crystals: Moving Substrates, ACS Nano. 9 (2015) 283-6178–6187. doi:10.1021/acsnano.5b01480.

[146] A.P. Shpak, A.M. Korduban, L.M. Kulikov, T. V. Kryshchuk, N.B. Konig, V.O. Kandyba, XPS studies of the surface of nanocrystalline tungsten disulfide, J. Electron Spectros. Relat. Phenomena. 181 (2010) 234–238. doi:10.1016/j.elspec.2010.05.030.

[147] Y. Chen, K. Xie, Z.X. Liu, Determination of the position of V^{4+} as minor component in XPS spectra by difference spectra, Appl. Surf. Sci. 133 (1998) 221–224. doi:10.1016/S0169-4332(98)00202-5.

[148] X. Lu, G. Wang, T. Zhai, M. Yu, J. Gan, Y. Tong, Y. Li, Hydrogenated TiO_2 nanotube arrays for supercapacitors, Nano Lett. 12 (2012) 1690–1696. doi:10.1021/nl300173j.

[149] X. Ding, T. Liu, S. Ahmed, N. Bao, J. Ding, J. Yi, Enhanced ferromagnetism in WS_2 via defect engineering, J. Alloys Compd. 772 (2019) 740–744. doi:10.1016/j.jallcom.2018.09.088.

[150] W. Yang, J. Wang, C. Si, Z. Peng, J. Frenzel, G. Eggeler, Z. Zhang, [001] Preferentially-oriented 2D tungsten disulfide nanosheets as anode materials for superior lithium storage, J. Mater. Chem. A. 3 (2015) 17811–17819. doi:10.1039/c5ta04176g.

[151] L. Jitkang, Y.S. Pin, C.H. Xin, L.S. Chun, Characterization of magnetic nanoparticle by dynamic light scattering, Nanoscale Res. Lett. 8 (2013) 381.

[152] V.B. Niste, M. Ratoi, H. Tanaka, F. Xu, Y. Zhu, J. Sugimura, Self-lubricating Al-WS_2 composites for efficient and greener tribological parts, Sci. Rep. 7 (2017) 1–14. doi:10.1038/s41598-017-15297-6.

[153] K. Shiva, H.S.S. Ramakrishna Matte, H.B. Rajendra, A.J. Bhattacharyya, C.N.R. Rao, Employing synergistic interactions between few-layer WS_2 and reduced graphene oxide

to improve lithium storage, cyclability and rate capability of Li-ion batteries, Nano Energy. 2 (2013) 787–793. doi:10.1016/j.nanoen.2013.02.001.

[154] Q. Wang, J. Li, Facilitated lithium storage in MoS_2 overlayers supported on coaxial carbon nanotubes, J. Phys. Chem. C. 111 (2007) 1675–1682. doi:10.1021/jp066655p.

[155] Y. Liu, N. Zhang, H. Kang, M. Shang, L. Jiao, J. Chen, WS_2 Nanowires as a High-Performance Anode for Sodium-Ion Batteries, Chem. - A Eur. J. 21 (2015) 11878–11884. doi:10.1002/chem.201501759.

[156] C. Zhu, P. Kopold, W. Li, P.A. Van Aken, J. Maier, Y. Yu, Engineering nanostructured electrode materials for high performance sodium ion batteries: A case study of a 3D porous interconnected WS_2/C nanocomposite, J. Mater. Chem. A. 3 (2015) 20487–20493. doi:10.1039/c5ta05758b.

[157] X. Wang, J. Huang, J. Li, L. Cao, W. Hao, Z. Xu, Improved Na Storage Performance with the Involvement of Nitrogen-Doped Conductive Carbon into WS_2 Nanosheets, ACS Appl. Mater. Interfaces. 8 (2016) 23899–23908. doi:10.1021/acsami.6b06032.

[158] D. Chen, G. Ji, B. Ding, Y. Ma, B. Qu, W. Chen, J.Y. Lee, In situ nitrogenated graphene-few-layer WS_2 composites for fast and reversible Li+ storage, Nanoscale. 5 (2013) 7890–7896. doi:10.1039/c3nr02920d.

[159] Q. Pang, Y. Gao, Y. Zhao, Y. Ju, H. Qiu, Y. Wei, B. Liu, B. Zou, F. Du, G. Chen, Improved Lithium-Ion and Sodium-Ion Storage Properties from Few-Layered WS_2 Nanosheets Embedded in a Mesoporous CMK-3 Matrix, Chem. - A Eur. J. 23 (2017) 7074–7080. doi:10.1002/chem.201700542.

[160] Z. A. Zhang, J. M. Li, X. D. Shi, J. Fang, and J. Li, Facile synthesis of WS_2 nanosheets-carbon composites anodes for sodium and lithium ion batteries, ChemNanoMat. 13 (2016) 997. doi:10.1016/S0740-5472(96)90021-5.

[161] X. P. Fang, C. X. Hua, C. R. Wu, X. F. Wang, L. Y. Shen, Q. Y. Kong, J. Z. Wang, Y. S. Hu, Z. X. Wang, L. Chen, Synthesis of graphene and electrochemical performance, Chem. Eur. J. 19 (2013) 5694–5700. doi:10.1002/chem.201204254.

[162] Y. Wu, X. Liu, Z. Yang, L. Gu, Y. Yu, Nitrogen-Doped Ordered Mesoporous Anatase TiO_2 Nanofibers as Anode Materials for High Performance Sodium-Ion Batteries, Small.

(2016) 3474. doi:10.1002/smll.201670126.

[163] H. Liu, K. Cao, X. Xu, L. Jiao, Y. Wang, H. Yuan, Ultrasmall TiO_2 nanoparticles in situ growth on graphene hybrid as superior anode material for sodium/lithium ion batteries, ACS Appl. Mater. Interfaces. 7 (2015) 11239–11245. doi:10.1021/acsami.5b02724.

[164] J. Marques, T.D. Gomes, M.A. Forte, R.F. Silva, C.J. Tavares, A new route for the synthesis of highly-active N-doped TiO_2 nanoparticles for visible light photocatalysis using urea as nitrogen precursor, Catal. Today. (2019) 36–45. doi:10.1016/j.cattod.2018.09.002.

[165] J. Wang, K. Tapio, A. Habert, S. Sorgues, C. Colbeau-Justin, B. Ratier, M. Scarisoreanu, J. Toppari, N. Herlin-Boime, J. Bouclé, Influence of Nitrogen Doping on Device Operation for TiO_2-Based Solid-State Dye-Sensitized Solar Cells: Photo-Physics from Materials to Devices, Nanomaterials. 6 (2016) 35. doi:10.3390/nano6030035.

[166] Z. El Koura, N. Patel, R. Edla, A. Miotello, Multilayer films of indium tin oxide/$TiO_{>2}$ codoped with vanadium and nitrogen for efficient photocatalytic water splitting, Int. J. Nanotechnol. 11 (2014) 1017. doi:10.1504/ijnt.2014.064297.

[167] X. Yao, X. Wang, L. Su, H. Yan, M. Yao, Band structure and photocatalytic properties of N/Zr co-doped anatase TiO_2 from first-principles study, J. Mol. Catal. A Chem. 351 (2011) 11–16. doi:10.1016/j.molcata.2011.09.027.

[168] Y. Hu, B. Wang, J. Zhang, T. Wang, R. Liu, J. Zhang, X. Wang, H. Wang, Synthesis and photoelectrochemical response of CdS quantum dot-sensitized TiO_2 nanorod array photoelectrodes, Nanoscale Res. Lett. 8 (2013) 1–5. doi:10.1186/1556-276X-8-222.

[169] D.G. Huang, S.J. Liao, W.B. Zhou, S.Q. Quan, L. Liu, Z.J. He, J.B. Wan, Synthesis of samarium- and nitrogen-co-doped TiO_2 by modified hydrothermal method and its photocatalytic performance for the degradation of 4-chlorophenol, J. Phys. Chem. Solids. 70 (2009) 853–859. doi:10.1016/j.jpcs.2009.04.005.

[170] J. Liu, R. Han, Y. Zhao, H. Wang, W. Lu, T. Yu, Y. Zhang, Enhanced photoactivity of V-N codoped TiO_2 derived from a two-step hydrothermal procedure for the degradation of PCP-Na under visible light irradiation, J. Phys. Chem. C. 115 (2011) 4507–4515. doi:10.1021/jp110814b.

[171] Z.L. Zhang, J.F. Li, X.L. Wang, J.Q. Qin, W.J. Shi, Y.F. Liu, H.P. Gao, Y.L. Mao, Enhancement of Perovskite Solar Cells Efficiency using N-Doped TiO_2 Nanorod Arrays as Electron Transfer Layer, Nanoscale Res. Lett. 12 (2017). doi:10.1186/s11671-016-1811-0.

[172] H. Wang, Y. Hu, The photocatalytic property of nitrogen-doped TiO_2 nanoball film, Int. J. Photoenergy. 2013 (2013). doi:10.1155/2013/179427.

[173] D.-K.K. and D.-W.P. Kanattukara Vijayan Bineesh, Synthesis and characterization of zirconium-doped mesoporous nano-crystalline TiO_2, Nanoscale. 2 (2010) 1057. doi:10.1039/c005273f.

[174] R.K. Singhal, S. Kumar, P. Kumari, Y.T. Xing, E. Saitovitch, Evidence of defect-induced ferromagnetism and its "switch" action in pristine bulk TiO_2, Appl. Phys. Lett. 98 (2011) 1–4. doi:10.1063/1.3562328.

[175] G.A. Battiston, R. Gerbasi, A. Gregori, M. Porchia, S. Cattarin, G.A. Rizzi, PECVD of amorphous TiO_2 thin films: Effect of growth temperature and plasma gas composition, Thin Solid Films. 371 (2000) 126–131. doi:10.1016/S0040-6090(00)00998-6.

[176] S. Sakthivel, M. Janczarek, H. Kisch, Visible light activity and photoelectrochemical properties of nitrogen-doped TiO_2, J. Phys. Chem. B. 108 (2004) 19384–19387. doi:10.1021/jp046857q.

[177] Y. Cong, J. Zhang, F. Chen, M. Anpo, Synthesis and characterization of nitrogen-doped TiO_2 nanophotocatalyst with high visible light activity, J. Phys. Chem. C. 111 (2007) 6976–6982. doi:10.1021/jp0685030.

[178] S.M. Oh, J.Y. Hwang, C.S. Yoon, J. Lu, K. Amine, I. Belharouak, Y.K. Sun, High electrochemical performances of microsphere C-TiO_2 anode for sodium-ion battery, ACS Appl. Mater. Interfaces. 6 (2014) 11295–11301. doi:10.1021/am501772a.

[179] J. Chen, W. Song, H. Hou, Y. Zhang, M. Jing, X. Jia, X. Ji, Ti^{3+} Self-Doped Dark Rutile TiO_2 Ultrafine Nanorods with Durable High-Rate Capability for Lithium-Ion Batteries, Adv. Funct. Mater. 25 (2015) 6793–6801. doi:10.1002/adfm.201502978.

[180] H. Zhang, Q. Deng, C. Mou, Z. Huang, Y. Wang, A. Zhou, J. Li, Surface structure and high-rate performance of spinel $Li_4Ti_5O_{12}$ coated with N-doped carbon as anode material

for lithium-ion batteries, J. Power Sources. 239 (2013) 538–545. doi:10.1016/j.jpowsour.2013.03.013.

[181] J. Lin, D. Ma, Y. Li, P. Zhang, H. Mi, L. Deng, L. Sun, X. Ren, In situ nitrogen doping of TiO_2 by plasma enhanced atomic layer deposition for enhanced sodium storage performance, Dalt. Trans. 46 (2017) 13101–13107. doi:10.1039/c7dt03303f.

[182] R. Zhang, Y. Wang, H. Zhou, J. Lang, J. Xu, Y. Xiang, S. Ding, Mesoporous TiO_2 nanosheets anchored on graphene for ultra long life Na-ion batteries, Nanotechnology. 29 (2018) 225401. doi:10.1088/1361-6528/aab562.

[183] H.A. Cha, H.M. Jeong, J.K. Kang, Nitrogen-doped open pore channeled graphene facilitating electrochemical performance of TiO_2 nanoparticles as an anode material for sodium ion batteries, J. Mater. Chem. A. 2 (2014) 5182–5186. doi:10.1039/c4ta00041b.

[184] Y. Wu, X. Liu, Z. Yang, L. Gu, Y. Yu, Energy Storage: Nitrogen-Doped Ordered Mesoporous Anatase TiO_2 Nanofibers as Anode Materials for High Performance Sodium-Ion Batteries (Small 26/2016) , Small. 12 (2016) 3474–3474. doi:10.1002/smll.201670126.

[185] R. Lan, J.T.S. Irvine, S. Tao, Synthesis of ammonia directly from air and water at ambient temperature and pressure, Sci. Rep. 3 (2013) 1–7. doi:10.1038/srep01145.

[186] S. Mukherjee, D.A. Cullen, S. Karakalos, K. Liu, H. Zhang, S. Zhao, H. Xu, K.L. More, G. Wang, G. Wu, Metal-organic framework-derived nitrogen-doped highly disordered carbon for electrochemical ammonia synthesis using N_2 and H_2O in alkaline electrolytes, Nano Energy. 48 (2018) 217–226. doi:10.1016/j.nanoen.2018.03.059.

[187] Y. Liu, Y. Su, X. Quan, X. Fan, S. Chen, H. Yu, H. Zhao, Y. Zhang, J. Zhao, Facile Ammonia Synthesis from Electrocatalytic N_2 Reduction under Ambient Conditions on N-Doped Porous Carbon, ACS Catal. 8 (2018) 1186–1191. doi:10.1021/acscatal.7b02165.

[188] G.F. Chen, X. Cao, S. Wu, X. Zeng, L.X. Ding, M. Zhu, H. Wang, Ammonia Electrosynthesis with High Selectivity under Ambient Conditions via a Li^+ Incorporation Strategy, J. Am. Chem. Soc. 139 (2017) 9771–9774. doi:10.1021/jacs.7b04393.

[189] D. Bao, Q. Zhang, F.L. Meng, H.X. Zhong, M.M. Shi, Y. Zhang, J.M. Yan, Q. Jiang, X.B. Zhang, Electrochemical Reduction of N_2 under Ambient Conditions for Artificial N_2 Fixation and Renewable Energy Storage Using N_2 /NH_3 Cycle, Adv. Mater. 29 (2017). doi:10.1002/adma.201604799.

[190] Y.J. He, J.F. Peng, W. Chu, Y.Z. Li, D.G. Tong, Black mesoporous anatase TiO_2 nanoleaves: A high capacity and high rate anode for aqueous Al-ion batteries, J. Mater. Chem. A. 2 (2014) 1721–1731. doi:10.1039/c3ta13906a.

[191] M. Xu, S. He, H. Chen, G. Cui, L. Zheng, B. Wang, M. Wei, TiO_{2-x}-Modified Ni Nanocatalyst with Tunable Metal-Support Interaction for Water-Gas Shift Reaction, ACS Catal. 7 (2017) 7600–7609. doi:10.1021/acscatal.7b01951.

[192] J. Ohyama, A. Yamamoto, K. Teramura, T. Shishido, T. Tanaka, Modification of metal nanoparticles with TiO_2 and metal-support interaction in photodeposition, ACS Catal. 1 (2011) 187–192. doi:10.1021/cs100072k.

[193] B.B. Tripathy, M. Behera, H. Rath, P. Mallick, N.C. Mishra, Evolution of microstructure and optical properties of TiO_2/Au nanocomposite, Indian J. Pure Appl. Phys. 57 (2019) 95–100.

[194] X. Li, T. Fan, H. Zhou, B. Zhu, J. Ding, D. Zhang, A facile way to synthesize biomorphic N-TiO_2 incorporated with Au nanoparticles with narrow size distribution and high stability, Microporous Mesoporous Mater. 116 (2008) 478–484. doi:10.1016/j.micromeso.2008.05.007.

[195] J.J. Mock, M. Barbic, D.R. Smith, D.A. Schultz, S. Schultz, Shape effects in plasmon resonance of individual colloidal silver nanoparticles, J. Chem. Phys. 116 (2002) 6755–6759. doi:10.1063/1.1462610.

[196] B. Shougaijam, C. Ngangbam, T.R. Lenka, Plasmon-sensitized optoelectronic properties of Au nanoparticle-assisted vertically aligned TiO_2 nanowires by GLAD technique, IEEE Trans. Electron Devices. 64 (2017) 1127–1133. doi:10.1109/TED.2017.2648500.

[197] R. Sanjinés, H. Tang, H. Berger, F. Gozzo, G. Margaritondo, F. Lévy, Electronic structure of anatase TiO_2 oxide, J. Appl. Phys. 75 (1994) 2945–2951. doi:10.1063/1.356190.

[198] B. Bharti, S. Kumar, H.N. Lee, R. Kumar, Formation of oxygen vacancies and Ti^{3+} state in TiO_2 thin film and enhanced optical properties by air plasma treatment, Sci. Rep. 6 (2016) 1–12. doi:10.1038/srep32355.

[199] C. Yang, Z. Wang, T. Lin, H. Yin, X. Lü, D. Wan, T. Xu, C. Zheng, J. Lin, F. Huang, X. Xie, M. Jiang, Core-shell nanostructured "black" Rutile Titania as excellent catalyst for hydrogen production enhanced by sulfur doping, J. Am. Chem. Soc. 135 (2013) 17831–17838. doi:10.1021/ja4076748.

[200] B. Li, Z. Zhao, Q. Zhou, B. Meng, X. Meng, J. Qiu, Highly efficient low-temperature plasma-assisted modification of TiO_2 nanosheets with exposed {001} facets for enhanced visible-light photocatalytic activity, Chem. - A Eur. J. 20 (2014) 14763–14770. doi:10.1002/chem.201402664.

[201] J. Wan, W. Chen, C. Jia, L. Zheng, J. Dong, X. Zheng, Y. Wang, W. Yan, C. Chen, Q. Peng, D. Wang, Y. Li, Defect Effects on TiO_2 Nanosheets: Stabilizing Single Atomic Site Au and Promoting Catalytic Properties, Adv. Mater. 30 (2018) 1–8. doi:10.1002/adma.201705369.

[202] M.A. Shipman, M.D. Symes, Recent progress towards the electrosynthesis of ammonia from sustainable resources, Catal. Today. 286 (2017) 57–68. doi:10.1016/j.cattod.2016.05.008.

[203] E. Skúlason, T. Bligaard, S. Gudmundsdóttir, F. Studt, J. Rossmeisl, F. Abild-Pedersen, T. Vegge, H. Jónsson, J.K. Nørskov, A theoretical evaluation of possible transition metal electro-catalysts for N_2 reduction, Phys. Chem. Chem. Phys. 14 (2012) 1235–1245. doi:10.1039/c1cp22271f.

Scientific Publications

[1]. **Hongmei Wang,** Qian Yuan, Dong Wang, Ge Chen, Xing Cheng, Thomas Kups and Peter Schaaf. Disordered Surface Formation of WS_2 via Hydrogen Plasma with Enhanced Anode Performances for Lithium and Sodium Ion Batteries, Sustainable Energy Fuels, 2019, 3, 865-874. DOI:10.1039/C8SE00566D

[2]. **Hongmei Wang,** Jie Xiong, Xing Cheng, Ge Chen, Thomas Kups, Dong Wang and Peter Schaaf, N-doped TiO_2 with a disordered surface layer fabricated via plasma treatment as an anode with clearly enhanced performance for rechargeable sodium ion batteries, Sustainable Energy Fuels, 2019, DOI:10.1039/C9SE00350A.

[3]. **Hongmei Wang,** Yong Yan, Ge Chen. The effects of confinement on TiO_2@SnO_2 @ TiO_2 hollow spheres for high reversible lithium storage capacity. Journal of Alloys and Compounds, 2019, 778, 375-381. https://doi.org/10.1016/j.jallcom.2018.11.123

[4]. **Hongmei Wang,** Yong Yan, Ge Chen, Integrating the hierarchical structure with well-dispersed conductive agents to realize synergistically enhanced electrode performance, J. Mater. Chem. A, 2015, 3, 10275–10283 (Back Cover). DOI: 10.1039/C5TA00984G

[5]. Yong Yan, Andreea Ioana Radu, Wenye Rao, **Hongmei Wang,** Ge Chen, Karina Weber, Dong Wang, Dana Cialla-May, Juergen Popp, and Peter Schaaf. Mesoscopically Bi-continuous Ag–Au Hybrid Nanosponges with Tunable Plasmon Resonances as Bottom-Up Substrates for Surface-Enhanced Raman Spectroscopy, Chem. Mater., 2016, 28 (21), 7673–7682. https://doi.org/10.1021/acs.chemmater.6b02637

[6]. Qian Yuan, Joachim Döll, Henry Romanus, **Hongmei Wang,** Heike Bartsch, Anre Albrecht, Marttin Hoffmann, Peter Schaaf and Dong Wang, Surface-Nanostructured Al–AlN Composite Thin Films with Excellent Broad-Band Antireflection Properties Fabricated by Limited Reactive Sputtering, ACS Appl. Nano Mater., 2018, 1 (3), 1124–1130. https://doi.org/10.1021/acsanm.7b00302.

[7]. Xiaoyan Liu, Xuezhao Shi, **Hongmei Wang,** Haixia Zhang. Atom transfer radical polymerization of diverse functional SBA-15 for selective separation of proteins, Microporous and Mesoporous Materials, 2014, 200,165–173. https://doi.org/10.1016/j.micromeso. 2014.08.027

Conferences

[1]. Student helper of 2nd International Conference on Applied Surface Science, 12-15 June 2017, Dalian, China.

[2]. 50th anniversary of Germany Annual Catalysis Meeting (50 Jahrestreffen Deutscher Katalytiker), 15-17. March 2017, Weimar, Germany.

[3]. **Hongmei Wang,** Ge Chen, Oral Presentation, Double shell TiO_2 hollow spheres encapsulating SnO_2 layer for high performance lithium ion battery, 1st International Conference on Applied Surface Science, 2015, Shanghai.

Supervision of master thesis and Project work

[1]. 2017 Master thesis, Yuan, Qian.
Topic: Hydrogenated WS_2 as Anode Material for Lithium ion Batteries.

[2]. 2018 Project work, Xiong, Jie.
Topic: Hydrogen and Nitrogen Plasma Treated Titanium Dioxide Anode Material for Sodium-ion Batteries

[3]. 2019 Master thesis, Xiong, Jie.
Topic:Preparation of Nanostructured Ni for Electrochemical catalysts of Hydrogen Evolution Reactions.

Declaration

I hereby declare that this Ph.D. dissertation entitled “Hydrogen and Nitrogen Plasma Treated Materials with Disordered Surface Layer used for Energy Storage and Conversion Devices” was carried out by me for the degree of Doctor under the supervision of Univ. Dr. rer. nat. habil. Dr. hc Peter Schaaf. All data or information in this dissertation that have been directly or indirectly consulted or used from other sources are clearly stated. This dissertation has not been submitted, in part or in whole, for any other degree or examination in any other University. I have acknowledged all main sources of help, and I have made clear exactly what was done by others and what I have contributed when the work was done jointly with others. Some of the results may have been published in scientific journals or elsewhere. I am aware that the falsity of this declaration will be regarded as an attempt of deception and will cause the derogation of the doctoral procedure.

Ilmenau, 02. September 2019 Hongmei Wang

(*Place, date*) (*Signature*)